$LiBH_4$–MgH_2 Composites for Hydrogen Storage

Vom Promotionsausschuss der
Technischen Universität Hamburg-Harburg
zur Erlangung des akademischen Grades
Doktor-Ingenieurin (Dr.-Ing.)
genehmigte Dissertation

von
Ulrike Bösenberg

aus
Hamburg

2009

Vorsitzender des Prüfungsausschusses: Prof. Dr. G. Schneider
1. Gutachter: Prof. Dr. R. Bormann
2. Gutachter: Prof. Dr. T. Klassen
Tag der mündlichen Prüfung: 08.06.2009

Contents

1 Introduction

At present, the supplied energy originates mostly from fossil fuels such as coal, oil and gas which are both, source as well as carrier of energy. Their high emission of greenhouse gases and pollutants during combustion as well as their limited resources are serious concerns and require the development of alternatives.

Hydrogen is a promising energy carrier for mobile applications because of its high energy content. Conversion of hydrogen into power leads only to water vapor as a final product. Greenhouse gases and pollutants are not emitted during this process. Modeling of atmospheric changes including an implementation of hydrogen fuel cell vehicles indicate a reduction of climate forcing [1], even if the hydrogen is produced from fossil fuels such as natural gas because of the higher well to wheel efficiency compared to conservative vehicles [2].

For implementation of hydrogen as a fuel, its production, transportation, storage and reconversion into power have to be managed. Hydrogen can be produced from fossil fuels or from renewable energy sources either directly or indirectly. Reconversion into power is achieved by sophisticated fuel cells or combustion engines. One of the major problems is the transport and storage because of the low explosion level of hydrogen and the high requirements on the system weight and density. Hydrogen can be stored in gaseous, liquid or chemically-bound form.

The major drawback of gaseous hydrogen is its low density at ambient conditions. Pressurization up to 700 bar increases the density but poses high requirements on the tank design and thus, the system weight capacity is lowered to approximately 5 wt%. Since this is the highest achieved value in practical applications at present, it sets the benchmark.

Liquefaction consumes already one third of the energy content of hydrogen because the boiling point of hydrogen is at 20 K. These low temperatures lead to boil-off losses despite good insulation. Because these losses can be kept small for large amounts and stationary tanks, these are favored applications for liquid hydrogen with its high density.

An alternative that avoids the so far described problems is chemical storage. Hydrogen can be adsorbed on large surfaces such as high-surface-area-activated-

carbons or carbon-nanotubes. The covalent bonding in the hydrogen molecule leads to a small interaction with the adsorbent. Reasonable storage capacities above 5 wt% are only obtained at cryogenic temperatures, thus similar problems as for liquid hydrogen have to be managed.

Hydrogen interacts strongly with metals to form a hydride phase. By storage in metal-hydrides, the hydrogen reaches high volumetric densities. In most cases, energy has to be provided to release the hydrogen again, thus creating a safe storage. But the well known transition-metal-hydrides are not suitable for mobile applications, due to their high atomic weight the storage capacities are only in the range of 1-2 wt%.

1.1 Hydrogen storage in metal hydrides for mobile applications

Essential for a highly efficient storage system is the combination of high gravimetric hydrogen capacities above 6 wt% with a desorption pressure of several bars in the temperature range of 80-120 °C, because then the waste heat of a standard Proton Exchange Membrane (PEM) fuel cell can be used to release the hydrogen from the hydride. These are the widely accepted targets for hydrogen storage in mobile applications, e.g., by the United States Department of Energy (US-DOE) [3]. In theory, the sorption temperatures and pressures are only determined by the reaction enthalpy, but in practice the reaction kinetics can have a significant influence. High reaction enthalpies are not only unfavorable due to the higher desorption temperatures but also during the absorption reaction because of the large amount of heat that has to be removed, thus posing high requirements on the heat management. High reaction rates are crucial for application, but they can be influenced through the microstructure of the metal hydride and by the addition of suitable catalysts. At present, no single metal hydride fulfills all the requirements at the same time.

The formation of alloys or intermetallic compounds are well known methods of thermodynamic tuning for metal hydrides since the pioneering work of Libowitz et al. [4]. They observed much higher desorption pressures of the ternary hydride $ZrNiH_3$ compared to the binary ZrH_2 at the same temperature. The change in thermodynamic properties due to the formation of an intermetallic phase in the desorbed state was investigated by Reilly and Wiswall [5, 6] for the Mg-Cu-H system, where intermetallic Mg_2Cu forms upon desorption. Mg-Ni-H is another well explored system in which a ternary hydride, Mg_2NiH_4, forms. Both systems have

reduced reaction enthalpies in comparison to pure MgH_2 and therefore show higher desorption pressures at the same temperature. MgH_2 is a preferable material due to the high gravimetric storage capacity and the availability of Mg, but addition of transition metals, e.g., nickel or copper reduces the gravimetric storage capacity significantly. Pure MgH_2 was investigated in detail and a breakthrough was achieved for the sorption kinetics by the addition of transition-metal-oxide catalysts [7, 8]. However, the thermodynamic properties of the material remained unchanged and its equilibrium pressure of 1 bar hydrogen at approximately 300 °C is unsuitable for practical applications. Extensive theoretical and experimental studies for ternary and quaternary hydrides with Mg were performed, but no suitable system was found so far [9, 10].

To overcome the drawback of the reduced gravimetric capacities of the multinary systems, the Reactive Hydride Composites (RHC) were recently developed [11–14]. In these, a chemical reaction between two or more hydrides lowers the overall reaction enthalpy while the gravimetric hydrogen storage capacity remains high. This concept is illustrated in figure 1.1. The new compound can be MgB_2, for example, formed by the exothermic reaction between a light metal borohydride and MgH_2. Reversible sorption reactions forming a boride upon desorption were observed for, e.g., $LiBH_4$−MgH_2, $NaBH_4$−MgH_2, $Ca(BH_4)_2$−MgH_2 and $LiBH_4$−Al composites, but the kinetics are slow and the details of the ongoing sorption reactions are not known [12, 14–16]. Theoretical estimations show promising reaction enthalpies for these composites, leading to suitable desorption pressures and temperatures for mobile applications combined with high gravimetric storage capacities [16, 17].

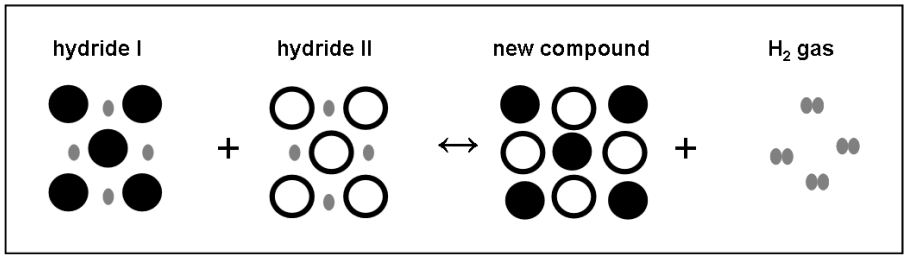

Figure 1.1: Schematic drawing of the concept of Reactive Hydride Composites (RHC)

1.2 Scope of the work

In the present work, $2\,LiBH_4+MgH_2 \longleftrightarrow 2\,LiH+MgB_2+4\,H_2$ composites are investigated in detail. This system shows a reversible hydrogen capacity of approximately 10.5 wt% and a theoretically assessed reaction enthalpy of 46 kJ/mol H_2, leading to an estimated equilibrium temperature of 170 °C at 1 bar H_2 [14,17]. Before the start of this work, little was known about the detailed reaction mechanism and the rate limiting processes, but this knowledge is fundamental for directed improvement of the reaction kinetics. Therefore, investigations on kinetic and thermodynamic properties and processes by means of (high-pressure) -differential-scanning-calorimetry, volumetric measurements and powder X-ray diffraction is one aim of the present work.

Transition- and light-metal based additives have a large beneficial effect on the reaction kinetics of the RHCs similar to the well known effect on the light metal hydrides MgH_2 and $NaAlH_4$ [7, 8, 18]. With the aim to discover the mechanism and function of the additives, their influence on the sorption kinetics is described in a phenomenological approach by volumetric measurements in a Sievert's type apparatus as a first step. In a second step the chemical state as well as size and distribution of Zr-based additives is studied exemplarily in more detail by X-ray absorption spectroscopy and anomalous small angle X-ray scattering(ASAXS). In a third step, confirmation of the observations by ASAXS and general knowledge of the microstructure are addressed by transmission electron microscopy (TEM). With this comprehensive understanding of chemical state, size, distribution and effect on the sorption kinetics a possible mechanism for the function of the additives is proposed. The present work contributes to the understanding of the ongoing reactions and the mechanisms of the additives which is mandatory for tailored composites with optimized reaction kinetics.

2 Experimental – materials and methods

In the following section, a short overview of the applied preparation and measurement techniques and parameters is given. Advantages as well as drawbacks of the methods are discussed.

2.1 Materials

The Reactive Hydride Composite system $LiBH_4{-}MgH_2$ as well as its hydrogenation and dehydrogenation reactions $2\,LiBH_4 + MgH_2 \longleftrightarrow 2\,LiH + MgB_2 + 4\,H_2$ are characterized kinetically, thermodynamically as well as by structural methods for the first and further sorption cycles. Because the initial conditions are well defined a special focus is put on the first desorption reaction with and without additive. During cycling, the reaction is not always complete and residual materials may influence the reaction. This is distracting and may be misleading when analyzing the reaction mechanism. A variety of transition metal based compounds such as chlorides, borides, isopropoxides and oxides are used as additives, but also the effect of adding final reaction products (MgB_2, LiH) is investigated. The materials used in the present study are purchased from commercial suppliers (Alfa Aesar or Sigma Aldrich) with the highest available purity. For better comparison of the composites, a series of experiments is performed with the materials of one production charge. This is especially important for the initial $LiBH_4{-}MgH_2$ composites, because $LiBH_4$ was only available with 95% purity and these composites show a variation of the sorption behavior with different production charges.

2.2 Sample preparation by high-energy ball milling

All investigated materials are prepared by high-energy ball milling using a Fritsch P5 or a Spex8000 Shaker mill. For all preparation hardened stainless steel vials

and milling balls are used. Unless noted otherwise, the ball to powder ratio is 10:1 and the MgH_2 is pre-milled with the final amount of balls, prior to adding $LiBH_4$ and additive. All milling experiments and handling of samples and materials are performed under continuously purified argon atmosphere in a glove box to protect the samples from oxidation. However, as a slight change in the sorption behavior of the composites is observed with storing time, the characterization is performed as close to preparation as possible.

2.3 Sample characterization by electron microscopy

The microstructure of as milled and cycled samples is characterized by electron microscopy. All samples are prepared at GKSS and selected samples are sent out for characterization to collaborating institutes. The scanning electron microscope (SEM) images are obtained at GKSS. The prepared powders are mounted on conductive carbon stickers under argon atmosphere. Short exposition to air could not be avoided during the transfer to the microscope. Transmission electron (TEM) micrographs are obtained in cooperation with Ms. Emilie Deprez and Prof. Asuncion Fernández Camacho at the Instituto de Ciencia de Materiales de Sevilla, Spain with a Philips CM 200 (figures 3.6, 3.7, 3.8 and 3.31(b)). Here, selected samples are mounted in emulsion with toluol to the copper-grid sample carriers. The details are given in [19]. Analysis of the chemical composition of the phases is addressed by energy dispersive X-ray spectroscopy (EDX) and electron energy loss spectroscopy (EELS). Only Mg and possible additives or O-impurities as well as the transition metal based additives can be detected by EDX. Identification of B is possible by EELS. But both, Li and H cannot be detected by either method due to their low atomic number. The samples are mounted in emulsion with toluol to the sample carriers, but always significant amounts of oxygen are measured in the samples. The formation of MgO and Li_2O is observed by diffraction. The samples are only partially stable under the beam, decomposition of MgH_2 to metallic Mg can be observed. Further high-resolution TEM investigations with a FEI Tecnai instrument on the samples are performed in cooperation with Dr. Dietrich Häußler and Prof. Wolfgang Jäger at the Christian Albrecht University in Kiel, Germany (figure 3.2). Here, the powder samples are mounted on carbon coated copper grids under argon atmosphere and mounted on the sample carrier and the microscope under ambient conditions. Short exposition to air could not be avoided for these measurements.

However, these investigations are limited to particle edges and very small particles. To overcome this drawback, uniformly thin slices are cut out of the particles by a focused ion beam (FIB) to be further investigated by TEM. These measurements are performed on selected samples in collaboration with Prof. Kyu Hwan Oh and Mr. Ji Woo Kim from the Seoul National University and Prof. Young Whan Cho and Dr. Jae-Pyoung Ahn from the Korean Institute of Science and Technology, Korea (figures 2.1, 3.3, 3.4, 3.32, 3.33, 3.34 and 3.35).

The preparation process in the FIB is illustrated in figure 2.1. Prior to sectioning a protective layer of Pt is deposited on center part of the particle, as illustrated by figure 2.1 (a). Cutting of the particles is performed with 30 keV Ga^+ ion beams from the back and front, leading to a thin sample slice, see figure 2.1 (b). This sample slice is then further cut out and further thinning to a final thickness of 50-90 nm is performed by milling parallel to the cross sectional plane, the final state is illustrated in figure 2.1 (c). This slice is then mounted on a copper grid and then transported to the TEM under inert conditions using an Ar filled glove bag. Up to now, investigations on as milled $LiH-MgB_2$ composites and as milled $LiH-MgB_2$ composites with 10mol% $ZrCl_4$ was performed, but further experiments on cycled samples are in progress. Details on the instruments and measurement parameters are given in [20].

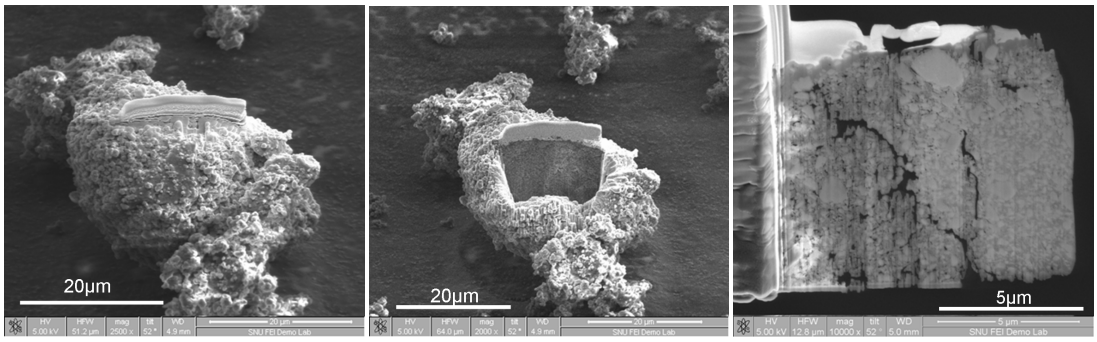

(a) Pt deposition (b) cross-sectioning (c) final thinning

Figure 2.1: Sequence of cross-sectional TEM sample preparation by FIB: (a) deposition of a Pt protective layer, (b) after cross-sectioning and (c) after final thinning.

2.4 Kinetic characterization

The reaction kinetics of the materials are measured in a volumetric Sievert's apparatus designed by HERA Hydrogen Systems. If not noted otherwise, the measurements for the desorption reaction are performed by heating to 400 °C and then keeping the sample isothermal until the end of the reaction. A back-pressure of 5 bar hydrogen is applied. To minimize the pressure change during the reaction, an additional volume of 1 l size is used. Standard conditions for the absorption reaction are 350 °C and 50 bar hydrogen. The measurement principle is based on the measurement of the pressure difference between the sample and a reference. Sample and reference-container are of identical design and are kept under identical conditions. For analysis, the change in pressure on the sample side due to the absorption or desorption reactions is converted into hydrogen content by weight percent using the ideal gas law. To minimize influences from surroundings, the main volume of the gas is kept at 40 °C.

2.5 Thermal analysis

The thermodynamic properties are investigated by differential scanning calorimetry (DSC) under flowing argon atmosphere as well as under hydrogen atmosphere. All instruments are placed in dedicated glove boxes. Thus oxidation of the samples prior and during the measurement is prevented. For sample containers, Al_2O_3 crucibles and lids provided by Netzsch are used. In the investigated temperature range of 20-500 °C no reaction with the sample material is observed.

2.5.1 Simultaneous thermal analysis and mass spectroscopy

Simultaneous DSC, thermogravimetry and mass spectroscopy of the exhaust gas is obtained using a Netzsch STA 409 C and a Hiden HPR-20 QIC mass spectrometer. The gas transfer takes place through a heated glass capillary of approximately 2 m length. If not otherwise specified the heating rate is 5 K/min, the argon flow 150 ml/min and the maximum temperature 470 °C. With this apparatus, only the desorption reaction can be investigated since the measurements take place under 1 bar argon. Due to the violent desorption reaction of $LiBH_4$ the maximum temperature is set to 480 °C for the composites and a high argon flow was used to transport the released gases.

2.5.2 High-pressure differential scanning calorimetry

For thermodynamic investigations on the reversible reactions of the composites, Netzsch DSC 204 HP Phoenix high-pressure DSC instruments are used. These measurements were performed at the Leibniz Institute for Solid State and Materials Research Dresden (figures 3.12, 3.19 and 3.43) or at the Helmut-Schmidt-University, Hamburg (figures 3.17 and 3.20). The standard hydrogen back pressure is 3 bar hydrogen for the desorption reaction and 50 bar hydrogen for the absorption. The apparatus work in dynamic mode, i.e. keeping the hydrogen pressure constant for the entire temperature range. The comparability of the dynamic conditions in the DSC and the isothermal static conditions in the Sievert's apparatus will be discussed in chapter 4.

2.6 Analysis with X-rays

X-rays are a powerful tool to investigate materials, they can be used to obtain information on, e.g., crystal structure, microstructure and chemical states. Basic characterization of the materials is obtained by laboratory X-ray diffraction. With the high intensity of the synchrotron sources, measurement times are short and in-situ investigations of the sorption reactions at non-ambient conditions are possible. In the following, the methods and parameters applied for the present work are described. A more fundamental background is given for the small angle X-ray scattering (SAXS) with a focus on anomalous small angle X-ray scattering (ASAXS). Measurement parameters and analysis procedure are described in detail. A short introduction to X-ray absorption spectroscopy (XAS) is given for the X-ray absorption near edge structure (XANES) measurements. Measurement parameters and analysis procedures are described with respect to samples with Zr-based additives.

2.6.1 Laboratory X-ray diffraction

For laboratory X-ray diffraction (XRD) a Bruker D8 Advance X-ray diffractometer or a Siemens D 5000 with Cu Kα radiation (λ =1.5418 Å) is used. The powders are protected from oxidation by Kapton film and measured in symmetrical reflection mode. The diffraction peaks give information on the phases present in the sample and their state. From the full width at half maximum (FWHM) of the diffraction peaks, an average crystallite size can be estimated by use of the Scherrer formula [21]

$$t = \frac{0.9 \cdot \lambda}{\beta \cdot \cos\theta} \tag{2.1}$$

where t is the thickness or diameter of the crystallites, λ the wavelength, β the FWHM in radians and θ half of the diffraction angle.

2.6.2 In-situ XRD at the synchrotron (MAX-lab and ESRF)

In-situ XRD measurements are performed in transmission mode at the I711 of the MAX-lab, Lund, Sweden [22] and at the Swiss Norwegian Beamline (BM01B) of the European Synchrotron Radiation Facility (ESRF), Grenoble, France. The samples are mounted into single crystal sapphire tubes under inert conditions in an argon filled glove box. At I711, the diffracted intensity is measured using a MAR 165 charge coupled device (CCD) plate detector with a typical wavelength of the radiation around 1 Å. The schematic setup used at I711, MAX-lab, is shown in figure 2.2. The sample is heated by a tungsten wire below the capillary and the temperature is controlled by an external proportional-integral-derivative (PID) regulator by a thermocouple inserted into the powder-bed. High-resolution powder diffractometry at the BM01B, ESRF, is performed in a similar setup using six counting chains with an offset of 1° and then averaging over all detectors.

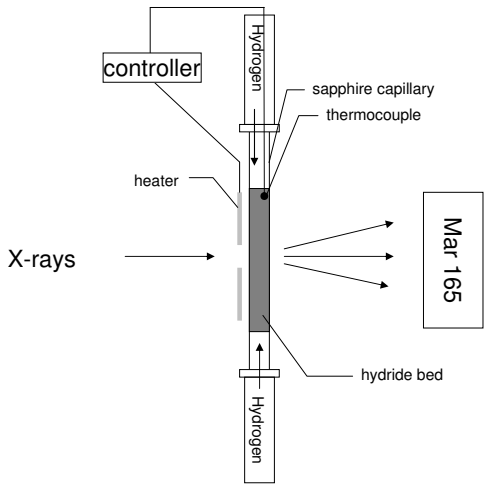

Figure 2.2: Schematic setup of the in-situ XRD setup at I711, MAX-lab, Lund

Pressures up to 150 bar hydrogen and temperatures up to 500 °C can be applied in the experimental setup at I711, MAX-lab and temperatures up to 600 °C and pressures up to 15 bar hydrogen are used at the BM01B, ESRF.

A quantitative analysis of the diffraction patterns in relation to time and temperature allows conclusions on the reaction mechanism and the reaction kinetics. The evolution of the crystallite sizes during the reactions can also be analyzed using the Scherrer formula (equation 2.1).

A short discussion of the accuracy of the temperatures during the experiments is necessary, because both experimental setups show errors in the temperature detection up $\pm 50\,\mathrm{K}$. The error is not systematic but varies with the location of the thermocouple during each experiment. At I711, MAX-lab, the thermocouple is integrated into the capillary and it is also used to regulate the oven. The temperature controller allows for fluctuations around $\pm 10\,\mathrm{K}$. But during the experiments, the observed decomposition temperatures show a disagreement of up 50 °C to to the known equilibrium temperatures.

At the BM01B, ESRF, the thermocouple is not integrated in the capillary, the deviation from the furnace temperature was measured at each temperature level manually approximately at the position of the beam. A large spatial variation of the temperature was noticed. Small deviations in the measuring position of the thermocouple lead to large variations in the recorded temperature of about 10-15 °C.

The influence of the high-flux photon beam at the synchrotron on the sample temperature shall be addressed shortly. At a wavelength of 1Å, the photon beam has an energy of approximately 12 keV. This corresponds to approximately 0.2 mW for the incident beam. At this energy, $LiBH_4{-}MgH_2$ composites have an absorption length of approximately 2.16 mm and absorb therefore up to of 30% of the beam energy in the used capillaries, this would correspond to 0.06 mW. According to $Q = m \cdot c_p \cdot \Delta T$, where Q is the amount of energy in J, m the sample mass with approximately 1 mg, c_p the heat capacity of the material, here assumed to take a value between 1 and $5\,J/(mg \cdot K)$ and ΔT the rise in temperature in K; the corresponding energy in one minute of 3.6 mJ could lead to a rise in temperature of 0.5 to 4 K, assuming that all photons go through the sample and all absorbed energy is converted to heat. These estimations show, that the temperature influence from the energy input of the photon beam is negligible small.

2.6.3 Small-angle X-ray scattering

Microstructural characterization of the investigated materials by standard techniques such as electron microscopy is challenging due to the nature of the materials as already pointed out in section 2.3. The hydrides are usually not stable under

the electron beam. Light elements such as Li and B cannot be detected by standard energy dispersive X-ray spectroscopy (EDX) and the nanostructural/partially amorphous state of the samples makes high resolution imaging difficult. Nonetheless, information on the microstructure and phase distribution of the hydrides as well as the additives is crucial for understanding the materials behavior and solving the observed kinetic problems.

Besides electron microscopy, small angle scattering (SAS) with neutrons (SANS) or X-rays (SAXS) are well known tools to characterize the nanostructure of a material. The methods are complementary to electron microscopy as SAS measurements average over the whole sample rather than probing locally. SAS bears the advantage of being independent of the physical state, such as crystalline, amorphous or liquid. Structural information can be obtained on inhomogeneities in the material because the difference between the electron density or scattering length density for the different phases leads to scattering of X-rays or neutrons, respectively. The difference between the electron densities defines mainly the contrast between the phases for the SAXS. Typically scattering from structures in the size range of 1-100 nm is observed at angles smaller than 5 °. The basics of SAS described in the following are covered in literature by, e.g., [23–26].

The scattered intensity measured in SAXS is expressed as the macroscopic differential scattering cross section $d\Sigma/d\Omega$. It is defined as the ratio of the number of particles scattered per second divided by the flux of the incident beam per unit solid angle Ω and has the dimensions of an area (cm^2). By normalization to unit sample volume, $d\Sigma/d\Omega$ is written in cm^{-1} [27]. The scattering cross section describes the probability to observe a scattering incident of a given inhomogeneity at a certain angle. In other words, if there is a typical and very often occurring size and shape it has a higher probability to scatter and therefore the measured intensity corresponding to this size and shape is likely to be higher. Usually, $d\Sigma/d\Omega$ is plotted as a function of the scattering vector q which describes the correlation between the vector of the incident wave to the scattered wave. The length of the scattering vector is hereby defined for the entire thesis as $q = 4\pi \sin\theta/\lambda$, where θ is half of the scattering angle and λ is the wavelength of the radiation. It is usually noted in nm^{-1} or $Å^{-1}$ and quantifies length scales in reciprocal space. For example, the Bragg distance is calculated as $d_{hkl} = 2\pi/q$. The normalization to the wavelength makes all independent measurements directly comparable.

In the following theoretical considerations, the scattering is assumed to be elastic and the intensity of the scattered radiation is small compared to the intensity of the incident beam, so that multiple scattering events are assumed to be negligible.

The amplitude of the scattered wave is the Fourier transform of the electron density distribution in the sample. But as the measured scattering intensity is defined as the absolute square of the scattering amplitude, analysis can not be performed by simple inverse Fourier transformation because the phase information is lost. However, the Fourier transform is used to obtain a distance distribution (autocorrelation) function, revealing information about the maximum lengths present in the sample.

The scattering amplitude $A(q)$ from point–like scatterers with an electron density $\rho(\mathbf{x})$, described by the vector $\mathbf{x}$ in the reciprocal space is expressed by

$$A(q) = \int \rho(\mathbf{x}) e^{-iq\cdot\mathbf{x}} d\mathbf{x} \tag{2.2}$$

The scattering intensity is then $|A(q)|^2$. To describe measurements of real samples with an almost infinite number of scattering centers, the individual contributions from the instrument and sample to the scattering intensity are grouped and the measured scattering intensity is expressed as

$$I(q) = I_0(\lambda)\Delta\Omega\eta(\lambda)T(\lambda)V_s\frac{d\Sigma}{d\Omega}(q) + B \tag{2.3}$$

where $I_0(\lambda)$ is the incident flux, $\Delta\Omega$ is the solid angle element defined by the size of the detector pixel, $\eta(\lambda)$ is the detector efficiency, $T(\lambda)$ the transmission and V_s the volume of the sample illuminated. $d\Sigma(q)/d\Omega$ is the differential scattering cross section per unit volume and B the background. The scattering cross section contains all the information about size, shape and interactions between the scattering structures and is described by

$$\frac{d\Sigma}{d\Omega}(q) = nV^2(\Delta\rho)^2 P(q)S(q) \tag{2.4}$$

where n is the number concentration of scattering centers, V is the volume of one scattering centre, $(\Delta\rho)^2$ the contrast. The form factor $P(q)$ contains the information on the size and shape of the structures. For the most common shapes like spheres or rods expressions have been derived. Whereas the structure factor $S(q)$ describes the interferences and therefore distances between the particles.

The sizes and shapes of the structures present in the sample are commonly evaluated by fitting and comparing calculated intensities of defined shapes and sizes to the measured intensities. For the more complex models it is often necessary to

have additional information from other methods like electron microscopy or chemical analysis to obtain reliable results from the model-fitting, because the solutions are not unique.

2.6.4 Anomalous small-angle X-ray scattering (ASAXS)

The increasing availability of tunable synchrotron radiation has risen the interest in resonant scattering and anomalous small-angle X-ray scattering (ASAXS) was introduced by Stuhrmann in 1980 [28]. Reviews treating the fundamental aspects as well as examples for application of this method can be found, e.g., in [28–31]. Some examples of application are the determination of shape and distribution of precipitates in metal alloys, porous catalysts and ion distributions in polymers.

Close to an absorption edge of an element the anomalous dispersion correction, the complex contribution to the atomic scattering factor f, can not be neglected any more. f is defined as $f(q,E) = f_0(q) + f'(q,E) + f''(q,E)$ where $f_0 = Z$, the number of electrons (atomic number), and $f'(q,E)$ the real and $f''(q,E)$ the imaginary part of the anomalous dispersion correction. The dependence f on q is small for small angles and is therefore neglected herein. Far away from an absorption edge, f is assumed to be constant and equal to Z. The real part f' is related to a phase shift of the interacting X-ray wave whereas the imaginary part f'' is related to the absorption. Figure 2.3(a) illustrates the contribution of the complex part at the absorption edge of zirconium. Especially the real part $f'(E)$ has a very strong contribution at energies just below the absorption edge.

This significant change in the scattering factor f in the vicinity of the absorption edge of an element leads to a change in the scattered intensity because the scattered intensity depends on the square of the scattering factor, $I(q,E) \propto f(E)^2$. This dependency is used for ASAXS by measuring SAXS at several different energies in the vicinity of the absorption edge. Due to the change in scattering intensity, a contrast variation is obtained and the scattering of the structures containing the respective element can be separated from the total scattering. Figure 2.3(b) shows the impact of the energy variation and the contribution of $f'(E)$ to the SAXS for the two marked energies. Where the solid line corresponds to the scattering at the energy marked by the filled symbol in figure 2.3(a) and the dashed line to the scattering at the energy marked by the open symbol. A small, but significant change in the scattering intensity is observed. In proportion to the total scattering amplitude, this change with the energy is small and thus accuracy and detector sensitivity are crucial. The higher intensity at the larger q values is due to fluorescence and

resonant Raman scattering. These inelastic contributions have to be removed prior to further analysis.

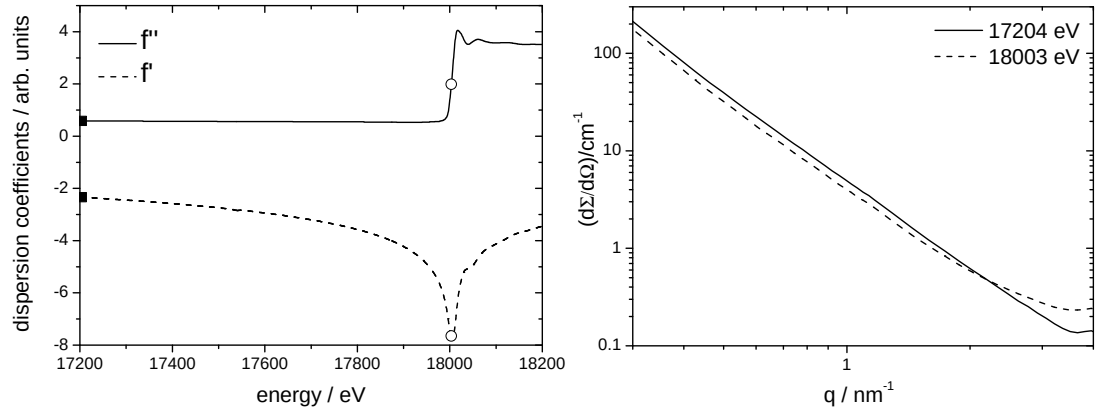

(a) anomalous dispersion correction for zirconium

(b) SAXS curves at the two marked energies

Figure 2.3: Variation and influence of the anomalous dispersion correction on the example of zirconium

A multicomponent phase system can be generally described by

$$\mathbf{I} = A\mathbf{S} \tag{2.5}$$

where $\mathbf{I}$ is a column vector of intensities $I(q, E)$, $\mathbf{S}$ is a column vector of the partial structure factors and A is the coefficient matrix containing volume fractions and scattering factors of the phases [32, 33]. The partial structure factors (PSF) describe the independent scattering contribution of each phase and the cross terms the scattering contribution of the interfaces and interactions between the phases. Due to the large electron density contrast between the hydride matrix and the transition metal element, the investigated samples were treated as two-phase systems. Equation 2.5 can then be written as

$$\begin{aligned} I(q,E) = \quad & x_\alpha \left| f_\alpha(q,E) \right|^2 S_{\alpha\alpha}(q) \\ & +2x_\beta \Re \left[f_\alpha(q,E) f_\beta(q,E) \right] S_{\alpha\beta}(q) \\ & +x_\beta \left| f_\beta(q,E) \right|^2 S_{\beta\beta}(q) \end{aligned} \tag{2.6}$$

where x_α and x_β are the atomic fractions of the phases α and β, f the described scattering factor and S the PSFs [34]. Only one phase shows energy dependent scattering in the measured energy range. Several methods to extract the PSFs for two and three component systems have been developed, e.g., by Lyon et al. [33, 35]

and Simon et al. [36], Fuoss et al. [37] and Munro et al. [38] as well as Goerigk et al. [39].

The calculation of the PSFs from equation 2.6 and 2.5 is very sensitive to statistical and systematical errors in the data and errors in the anomalous dispersion factors [40] and sometimes even negative PSFs are observed [36, 40], which can not be explained physically.

The PSF for the energy dependent scattering phase can also be solved by differentiation of the intensity for each energy and q-value with respect to f'. After plotting, a line is fitted at each q-value. The slope of this line is then proportional to $S_{\beta\beta}$. This method is described in detail in [37, 38] and was recently successfully applied by Vainio et al. [40, 41].

Goerigk et al. [39] have evolved a set of equations for a two phase-system and three measuring energies to determine the PSF. Here, exact knowledge of the anomalous dispersion corrections and atomic fractions of the phases are required. However, the quality of the determined scattering factor and estimation of the atomic fractions of the investigated samples is insufficient for using this method.

The scattering contribution of the cross term $S_{\alpha\beta}$ is calculated to be small. Therefore the difference in the differential scattering cross section at the highest and lowest measuring energy is taken as the PSF and further analyzed.

For the vanadium containing samples, a large number of scattering curves have to be discarded due to unreliabilities in the data. As can be seen from this discussion, precise measurements and a careful evaluation of the obtained data is mandatory for each sample.

Measurement parameters For ASAXS measurements the Zr-containing powders are filled in 1 mm thick sample holders of aluminum alloy with a hole of 5 mm in diameter and sealed by two 55 µm thick Kapton tapes in an argon filled glovebox. For a similar transmission and to avoid multiple scattering effects, the thickness for the V-containing samples is approximately 50 µm. The measurements are performed under vacuum conditions at beamline B1, Hasylab, DESY [42, 43]. Prior to each ASAXS measurement a low resolution XANES scan is measured to determine the position of the absorption edge of each sample. The beamline is calibrated to the edge energies of Zr-foil at 17998 eV and V-foil at 5665 eV [44]. The individual SAXS measurements are performed at 5 or 6 energies below the previously determined absorption edges for the Zr-containing materials and at 3 energies for the V-containing samples. All samples are measured at two sample-to-detector distances of 935 mm and 3635 mm to cover the maximum available q-range. The reliable q-range of the

instrument in the energy range of Zr is concluded to be from 0.2 to 14 nm^{-1} and in the energy range of V from 0.1 to 4 nm^{-1}. Three measurement cycles are performed for each sample at each energy and distance. The measured 2D data is corrected for dark current, detector response, transmission of the sample, and for geometrical distortion and integrated azimuthally. Further, the intensities are put on absolute intensity scale by using pre-calibrated glassy carbon standards. A q^{-4} dependence is fitted to the scattering data at high q values and then subtracted to correct the data for an energy dependent background caused by fluorescence and resonant Raman scattering.

For the vanadium containing samples, a large number of scattering curves had to be discarded due to unreliabilities. The absorption edge of V is at 5665 eV just at the edge of possible measuring energies of the instrument. The detector sensitivity at these X-ray energies is rather poor and a substantial contribution from slit scattering was observed and only parts of the obtained 2D scattering signal could be used.

Analysis-model fitting After determination of the PSF, the separated scattering curve can be treated and analyzed as a normal SAXS curve. In a first approach, to analyze the typical size of the Zr-containing compounds the Debye-Bueche model was used. It is a two phase model with sharp interfaces but random shape and distribution of the phases. A schematic image of the model is shown in figure 2.4. The model was first developed by Debye et al. [45] and recently applied by Goerigk and Williamson [46, 47] on ASAXS data. The separated scattering curves were fitted to the function

$$\frac{d\sigma}{d\Omega}(q) = \frac{ba^3}{(1+a^2q^2)^2} + \frac{c}{q^4} \tag{2.7}$$

with the correlation length a, from which the two correlations lengths of the phases α and β, ξ_α and ξ_β, can be calculated according to $1/a = 1/\xi_\alpha + 1/\xi_\beta$. The correlation length $\xi_\beta = x_\beta \cdot a/(1-\Phi_\beta)$ corresponds to the Zr-containing phase β with its volume fraction Φ_β. The constant b includes information on the volume fraction, density and concentration of phase α. The equations to estimate b from the fit described in [47] cannot be solved in this case because neither the density of the material nor the composition are known exactly. Therefore, the volume fractions were assessed from the chemical formula of the composites. The additional c/q^4-term comes from large Zr-containing inhomogeneities where c is a constant.

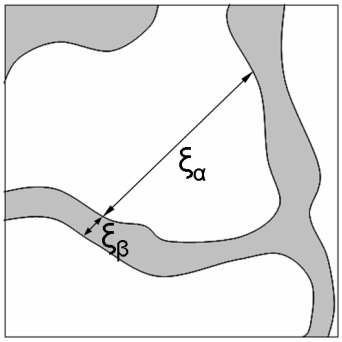

Figure 2.4: Schematic drawing of the Debye-Bueche model [47].

2.6.5 X-ray absorption Spectroscopy

In the energy range of an absorption edge of an element, compounds display a characteristic absorption character [48,49]. Changes in the charge distribution around a given atom in different chemical environments (e.g. different oxidation states) can alter core-level binding energies and thus lead to a shift of the absorption edge by several eV. The atoms surrounding the absorbing atom modulate the absorption at energies above the edge by scattering –the so called fine structure– is observed. A typical curve is illustrated in figure 2.5 for metallic Zr-foil. The fine structure reveals information on the distance and chemical character of the surrounding atoms. The region near the edge, the X-ray absorption near edge structure (XANES) range, is dominated by multiple scattering of the electrons and therefore revealing details of the electronic properties and the spatial arrangement of the atoms around the absorbing one and the electronic properties. The extended X-ray absorption fine structure (EXAFS) is dominated by single scattering phenomena because the excited electrons have reached the continuum states. The information on the geometrical distribution of the surrounding atoms can be extracted.

In this work, a qualitative comparison to reference samples was performed in the XANES range. Reliable conclusions on the present chemical state of the investigated material can be drawn.

The measurements are performed at Beamline A1, Hasylab, Desy [50, 51] on samples with Zr-based additives, the same samples used for ASAXS. The samples are mixed with cellulose and pressed into pellets of 11 mm in diameter. These pellets are then mounted between two 55 µm Kapton tapes on aluminum sample holders. The absorption coefficient μ_d is measured from approximately 100 eV below the k-edge of zirconium at 17998 eV to about 900 eV above. For each sample, the

average from three measurements is taken, normalized and corrected for pre-edge background.

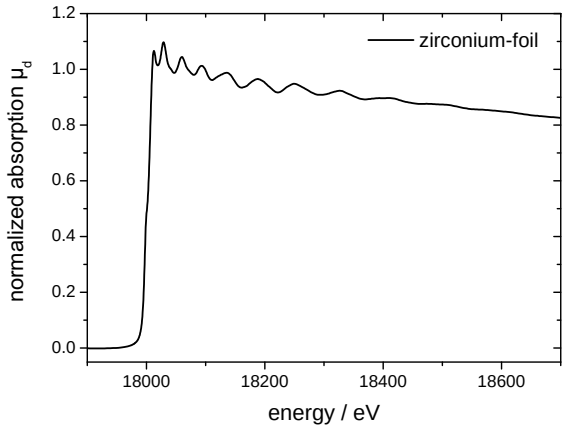

Figure 2.5: Linear absorption coefficient near the k-absorption edge of metallic zirconium.

The data obtained from the X-ray absorption spectroscopy is further used to determine the anomalous dispersion coefficients f' and f'' described in 2.6.4 using the CHOOCH program by Evans [52]. The absorption edge is determined from these measurements according to [53] by taking the first inflection point of the first derivative of the absorption coefficient and is listed for each sample in table 3.1.

3 Results

The experiments are focused on finding and identifying the detailed reaction mechanisms and improving the sorption kinetics in $LiBH_4-MgH_2$ composites by suitable additives. This task is addressed by a combination of different experimental methods such as volumetric measurements, (High-pressure)- differential scanning calorimetry (DSC) and in- and ex-situ XRD. By these methods, important features like, reaction kinetics, storage capacity, ongoing reactions and the present crystalline phases are characterized. However, careful evaluation of the experimental conditions of the different methods is necessary before comprehensive conclusions can be drawn. The general issue of microstructure and phase distribution in the composites is addressed by electron microscopy studies.

Furthermore, the beneficial effect of additives and cycling on the reaction kinetics is investigated in more detail. The impact of transition-metal-chlorides, -isopropoxides and -oxides as well as surplus system compounds are described in a phenomenological approach by volumetric measurements. To shed light on the mechanism of these additives, more detailed studies are performed exemplarily for Zr-based additives by means of anomalous small angle X-ray scattering (ASAXS) and X-ray absorption spectroscopy (XANES). The location of the Zr additives is addressed in a high resolution TEM study. The results give information on the size, distribution and chemical state of the Zr-based compounds for the samples in the as prepared and cycled state. From this, conclusions on the origin of the beneficial effect of the transition-metal based additives are drawn.

3.1 Microstructure and phase distribution in the pure composites

The microstructure and phase distribution are key issues for the materials functionality, because significant mass transport of heavier atoms like Mg or B has to take place during the sorption reactions. Therefore, short diffusion paths are crucial for fast sorption kinetics. In a first approach the general phase distribution in

the milled, pure composites is addressed, revealing typical size ranges and phase distribution. The details for the sample preparation are given in chapter 2.3.

LiH−MgB_2 composites Figure 3.1(a) shows a SEM image of as milled LiH−MgB_2 composite. After the milling process, typical particle sizes between 5-20 µm are observed. Analysis of the XRD pattern of as milled LiH−MgB_2 composites in figure 3.1(b) shows the presence of two crystalline phases LiH and MgB_2 and crystallite sizes in the range of 10-20 nm are derived by the Scherrer formula. This is two orders of magnitude smaller than the structures observed in the SEM.

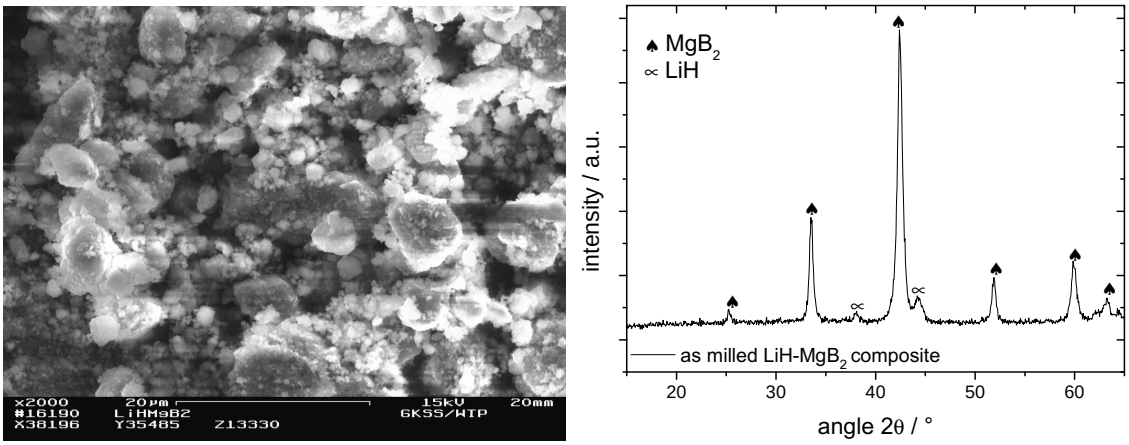

(a) SEM image (b) XRD pattern

Figure 3.1: SEM image and XRD pattern of as milled LiH−MgB_2 composite.

In case of SEM, short air exposure of the sample could not be avoided and thus structural changes due to the contact with air cannot be excluded.

To visualize the phase separation measured by XRD, higher resolution measurements are necessary. In figure 3.2 a high resolution TEM image of as milled LiH−MgB_2 composites is shown. The pattern of thin lines represent the atomic layers of individual crystallites. With the applied setup an identification of the different phases LiH and MgB_2 phases was not possible but an average crystallite size around 50 nm can be deduced. This is about twice the size than estimated from the XRD measurements.

These observations of particle edges and small particles suggest homogeneity and fine crystallinity of both phases.

Further measurements on the cross-section of the as milled LiH−MgB_2 composites support this assumption, see figure 3.3. The dense coating visible at the top is the protective Pt layer. The sample shows a homogeneous two phase mixture.

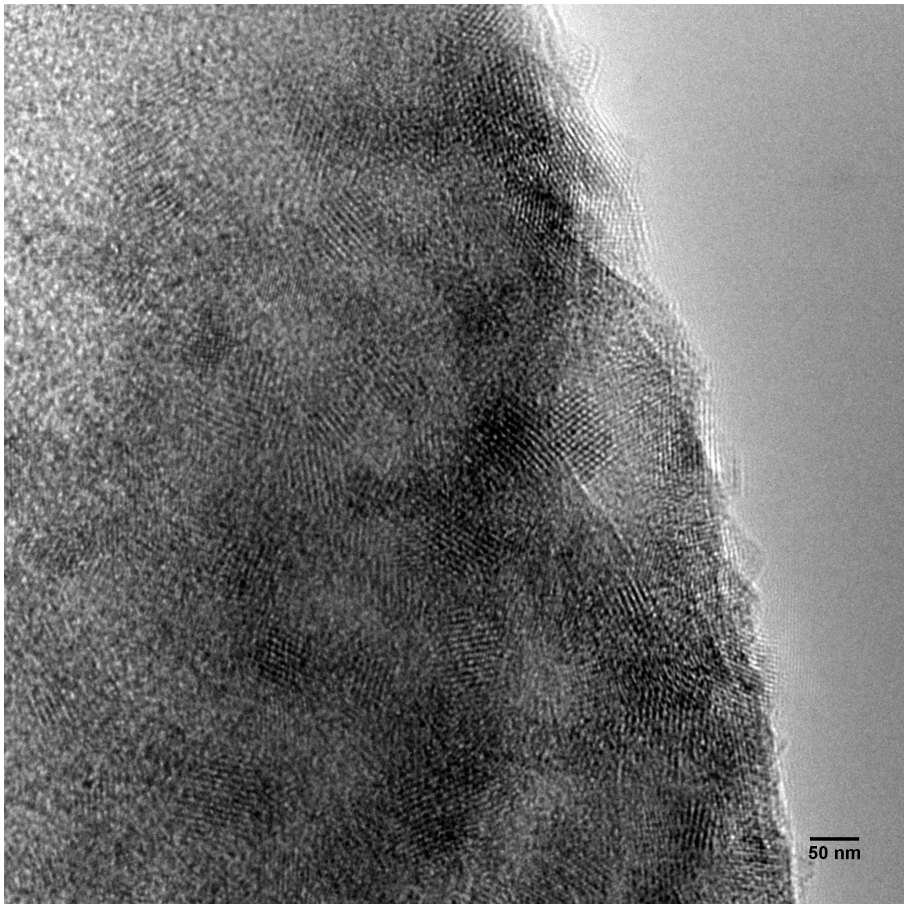

Figure 3.2: High resolution TEM image of as milled LiH−MgB_2 composites.

This sample with a final thickness of approximately 50 nm is then transferred to the TEM under argon atmosphere. The micrographs indicate the MgB_2 crystallites to be embedded in a almost amorphous LiH phase. Here, the influence from the electron beam might play a role because although the reflections are weak, peaks from crystalline LiH can be observed in powder diffraction measurements. This is imaged in figure 3.4 (a). The element distribution obtained by EELS of Li, Mg and B is mapped in detail in figures 3.4 (b) through (d). Light regions indicate a large content of the respective element while the dark region present a low concentration. From this analysis a correlation between the B and Mg content can be observed. However, this conclusion is not valid for all clusters, which can be explained by, e.g., LiH layers above or below the respective MgB_2 crystallite. Therefore the darker regions in figure 3.4 (a) can be attributed to consist mainly of MgB_2 while the lighter parts correspond to a LiH matrix.

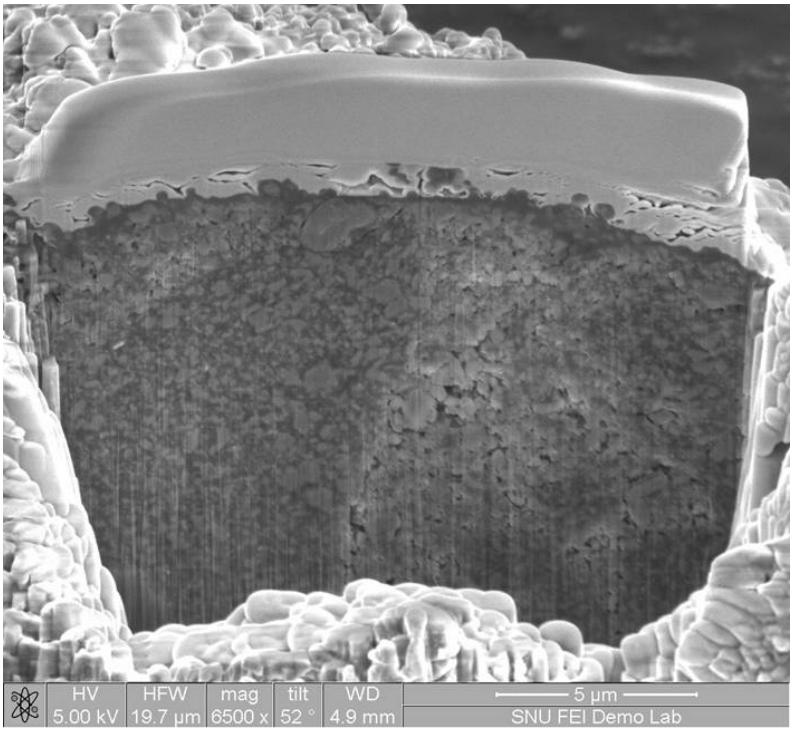

Figure 3.3: SEM images of the cross sections of as milled LiH−MgB_2 composites.

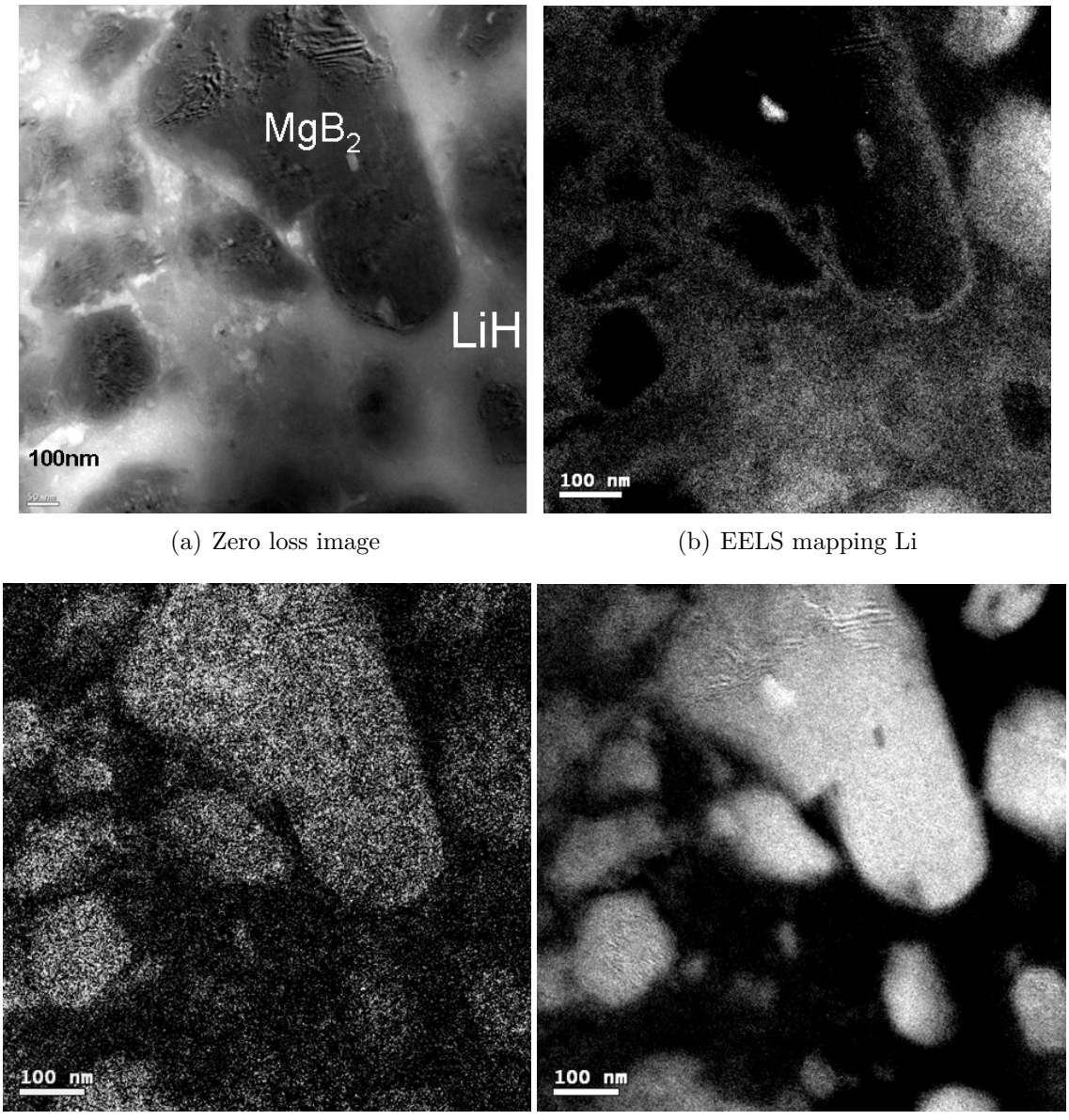

(a) Zero loss image

(b) EELS mapping Li

(c) EELS mapping B

(d) EELS mapping Mg

Figure 3.4: TEM micrograph and EELS mapping of elements of the corresponding region.

$LiBH_4-MgH_2$ composites In figure 3.5 the SEM image (a) and XRD pattern (b) of as milled $LiBH_4-MgH_2$ composite is presented. Imaging of the $LiBH_4-MgH_2$ composites is difficult, because of the low conductivity of the surfaces, the particles are charged and make higher resolution impossible. Analysis of the XRD pattern reveals the material to consist of nanocrystalline $LiBH_4$, MgH_2 and γ-MgH_2 after milling with typical crystallite sizes for the MgH_2 of 10-20 nm. $\gamma-MgH_2$ is a metastable structure of MgH_2 that is, e.g., formed during high-energy ball milling. The observed particles are much larger than the small crystalline units and the particles are therefore assumed to consist of multiple crystallites, similar to the $LiH-MgB_2$ composites.

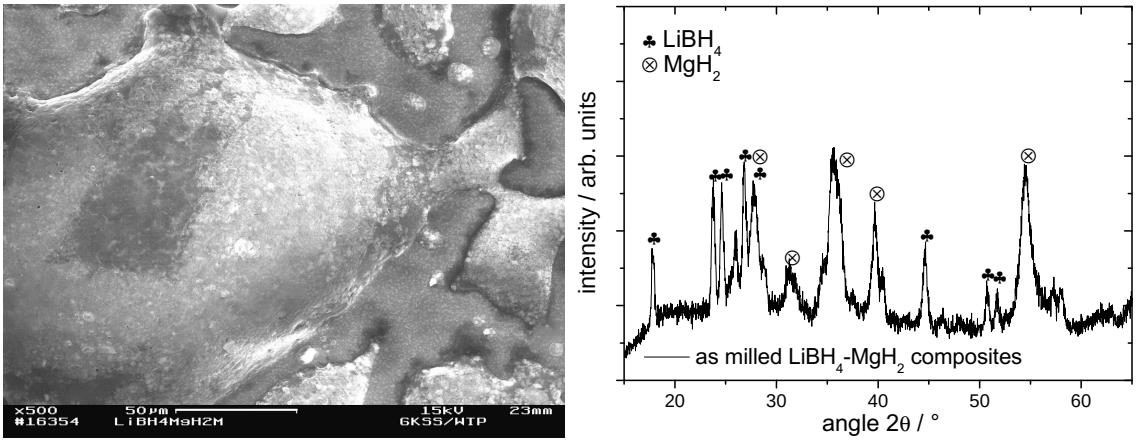

(a) SEM image (b) XRD pattern

Figure 3.5: SEM image and XRD pattern of as milled $LiBH_4-MgH_2$ composites.

In comparison to the $LiH-MgB_2$ composites the as milled $LiBH_4-MgH_2$ composites display a much coarser phase distribution, see figure 3.6. Two distinct regions can be differentiated on a larger scale of about 300 nm, dark and spotty and fairly homogeneous and light.

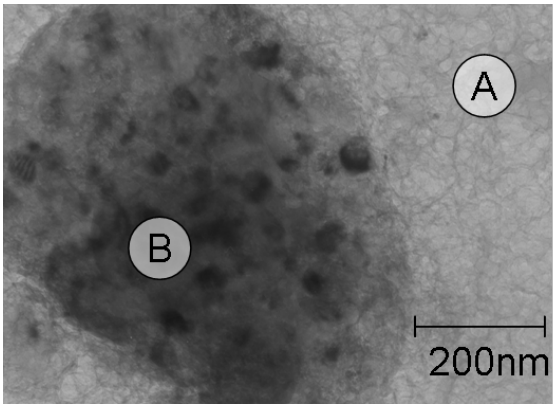

Figure 3.6: TEM image of $LiBH_4-MgH_2$ composites in the as milled state.

The diffraction pattern obtained in the microscope for this region A, shown in figure 3.7(a), reveals only amorphous structures. This is possibly due to the impact of the electron beam or to the preceding emulsion in toluol. The EEL spectrum of this region, shown in figure 3.7(b) by the black trace with the open symbols, displays very similar features to the EEL spectrum obtained for pure $LiBH_4$ (gray trace) and significant differences to the EEL spectrum of MgB_2 (black trace). The light gray material in region A is therefore proposed to consist of $LiBH_4$.

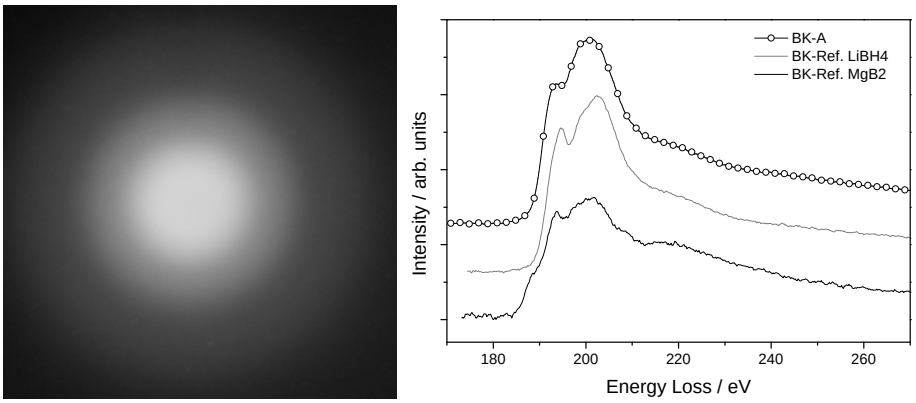

(a) diffraction region A (b) EELS region A

Figure 3.7: TEM diffraction image and B-EELS of region A.

Diffraction analysis of region B shows mainly metallic Mg and MgO, see figure 3.8 (a). This is also confirmed by the strong Mg signal obtained by EDX measurements shown in figure 3.8 (b). MgH_2 is not stable under the electron beam and decomposes therefore into metallic Mg. Thus MgH_2 seems to be embedded in $LiBH_4$ matrix.

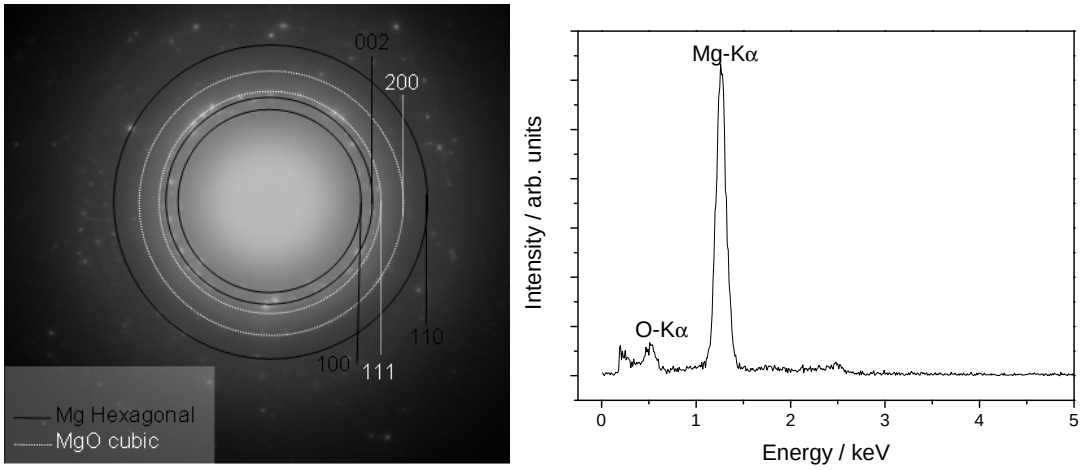

(a) Diffraction region B

(b) EDX-region B

Figure 3.8: TEM diffraction image and EDX of region B.

3.2 The first desorption reaction – kinetics and mechanism

The previous section illustrated the microstructure of the composites. Information on the sorption properties, reaction kinetics and reaction steps is addressed in the following section. The first desorption reaction of freshly milled $LiBH_4{-}MgH_2$ composites is presented in detail by volumetric measurements, DSC and XRD. The first desorption reaction of the pure composite is scientifically interesting because of the chemically well defined starting conditions and therefore clear reaction mechanism. From later experiments it is known, that the absorption reaction is often incomplete and small amounts of residual MgB_2 are detected. This makes a determination of the formation of new MgB_2 in the next desorption reaction difficult. The influence of the measurement parameters such as pressure and temperature on the reaction mechanism is reviewed.

3.2.1 Volumetric measurements

Volumetric measurements of the first desorption reaction of $LiBH_4{-}MgH_2$ composites were carried out in a Sievert's type apparatus to determine the reaction kinetics. In figure 3.9 the kinetic curves for the milled pure composite are shown under vacuum conditions and under a hydrogen back-pressure of 5 bar. The initial state of the as-milled powder is illustrated by XRD scan (a) in figure 3.10. It con-

sist of nanoscale $LiBH_4$ and MgH_2 crystallites. For the experiments the sample was heated to 400 °C and then kept isothermal, the dashed line represents the sample temperature. All reactions occur on a very large time scale in the hour-to-days range in two reaction steps.

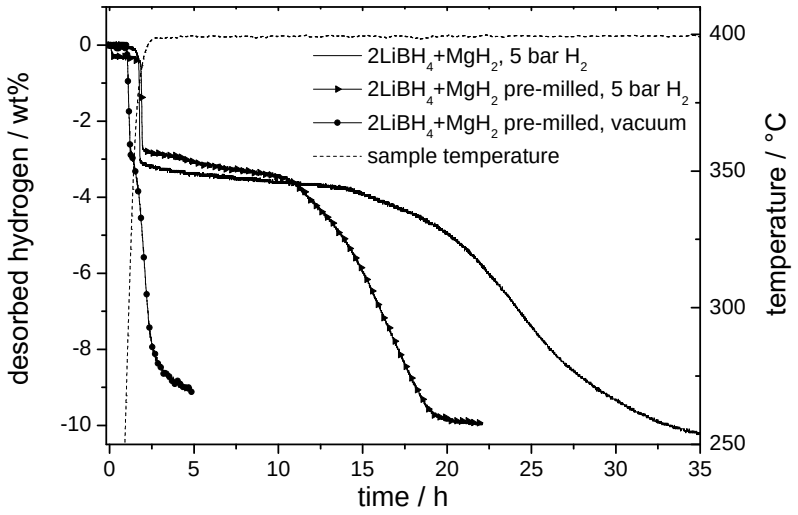

Figure 3.9: First desorption reaction of the pure $LiBH_4$−MgH_2 composite under 5 bar hydrogen and vacuum conditions.

The sample measured under vacuum conditions displays the shortest reaction time and therefore the fastest reaction kinetics. The hydrogen capacity measured within 9 h is approximately 9.5 wt%. Analysis of the reaction products by XRD reveals only metallic Mg and LiH, see figure 3.10 trace (b). The state of the boron in this sample is unknown, one possibility is the formation of amorphous boron, which is invisible to X-rays and the other possibility is the formation of volatile B_2H_6. From these reaction products, only rehydrogenation of Mg to MgH_2 was achieved [54]. To obtain the desired reaction products LiH, MgB_2 and hydrogen, measuring with a back-pressure of several bar hydrogen is necessary at this temperature. This is confirmed by XRD measurements after desorption in figure 3.10, trace (c), the solid reaction products are now LiH and MgB_2. The observation of this important boundary condition was also reported in literature [14].

However, for the pure samples measured under 5 bar hydrogen pressure at 400 °C a lengthy "incubation" period of about 15 h is observed, see the line trace and the trace with the triangles in figure 3.9. Approximately 10 wt% are desorbed within 35 h. For the composites containing the pre-milled MgH_2 (trace with the triangles in figure 3.9) a shorter incubation period and an overall faster reaction are observed, the reaction is completed after 20 h. This is assumed to be related

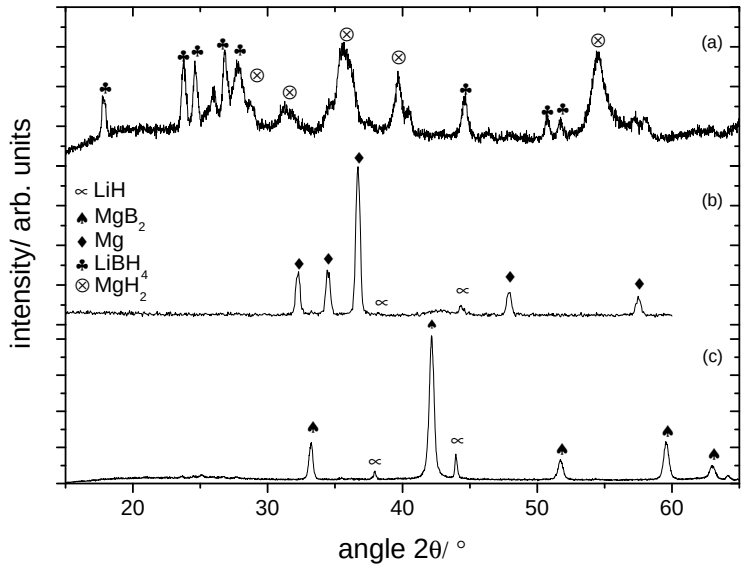

Figure 3.10: XRD of the pure $LiBH_4-MgH_2$ composites in the milled (a) and desorbed state, reactions performed under vacuum conditions (b) and 5 bar hydrogen pressure (c).

to a more efficient milling procedure, achieving finer crystallite and particle sizes and better distribution of the two phases. The origin of the incubation period for the pure compounds in the first desorption reaction will by addressed in further investigations, see section 3.4.

3.2.2 Thermal analysis

Volumetric measurements describe the overall reactions in a phenomenological approach. To understand the ongoing reactions in detail, a thermodynamic description of the individual processes is necessary for the complex reactions in the composites. This is addressed by simultaneous thermal analysis performed in a DSC apparatus combined with thermogravimetry and mass spectroscopy of the exhaust gas. In figure 3.11 the first heating to 480 °C of the $LiBH_4-MgH_2$ composites under argon-flow is measured. Four distinct endothermic reactions are observed. The first at approximately 110 °C is denoted A and relates to the polymorphic transformation of $LiBH_4$ from orthorhombic to hexagonal lattice structure [55]. The second endothermic peak at around 275 °C is the melting of $LiBH_4$ [56] and is denoted as B. In further diagrams the respective solidification during cooling is also indexed as B. The first melting of commercial $LiBH_4$ is sometimes correlated to a slight release of hydrogen [57]. For some samples, especially with additives, a decrease

of the melting temperature by as much as 20 °C was observed in DSC measurements. A direct correlation to the desorption temperature was not observed, but the influence was not investigated in detail.

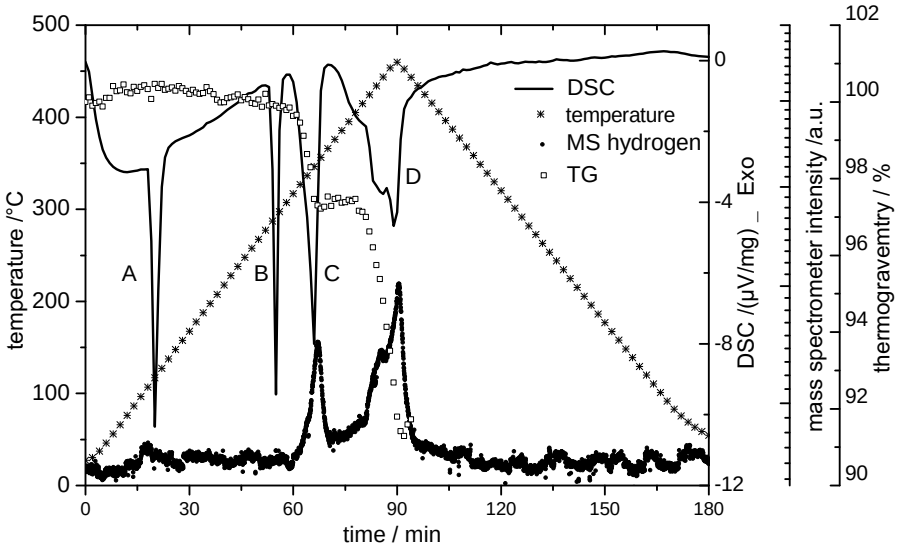

Figure 3.11: Simultaneous thermal analysis of $LiBH_4$−MgH_2 composites coupled with mass spectrometric analysis of the exhaust gas.

As shown by the Mass spectrometer- and balance signal, reactions C and D are accompanied by a significant release of hydrogen and loss of weight and correspond therefore to the desorption reactions. Further analysis of the reaction mechanism in section 3.2.3 reveals reaction C to belong to the desorption of MgH_2 and the reaction D to the desorption of $LiBH_4$. The ragged shape of the reaction D indicates a multiple step reaction or kinetic constraints. This was also observed for the pure $LiBH_4$ by Züttel et al. [58, 59], first suggesting intermediate formation of $LiBH_3$ and $LiBH_2$. Recently, the intermediate formation of $Li_2B_{12}H_{12}$ was proposed and experimentally confirmed by [60–62], but it is not known, whether its formation corresponds also to the ragged shape of the DSC peak.

For pure and doped $LiBH_4$ the release of gaseous diborane, B_2H_6, was observed [63], for the composites, however, only hydrogen was detected in the exhaust gas. Small amounts of gaseous B_2H_6 can not be excluded, though. Due to the long distance from the reaction vessel to the analyzer the decomposition of B_2H_6 before it reaches the analyzer is possible.

As shown in figure 3.9, the desorption under vacuum leads only to the formation of Mg and amorphous B or B_2H_6 and not MgB_2 in the investigated temperature

range. Therefore the decomposition mechanism under an argon flow is not necessarily the same as under a low hydrogen back-pressure.

A desorption measurement under hydrogen atmosphere in a high-pressure DSC was therefore carried out. In figure 3.12 the measurement of the first desorption reaction of the pure $LiBH_4-MgH_2$ composite is shown under 3 bar hydrogen pressure and a heating rate of 5 K/min. The reactions are labeled as before. Reactions A and B show little dependency on the pressure, however, reactions C and D are shifted to higher temperatures. The desorption of $LiBH_4$ (reaction D) is incomplete, which is clearly visible by reactions B (solidification of $LiBH_4$) and A (phase transformation of $LiBH_4$) during the cooling. The desorption reactions show kinetic restrictions in the DSC apparatus, because a complete desorption of $LiBH_4-MgH_2$ composites under isothermal conditions at 400 °C and 5 bar hydrogen was observed beforehand, see figure 3.9.

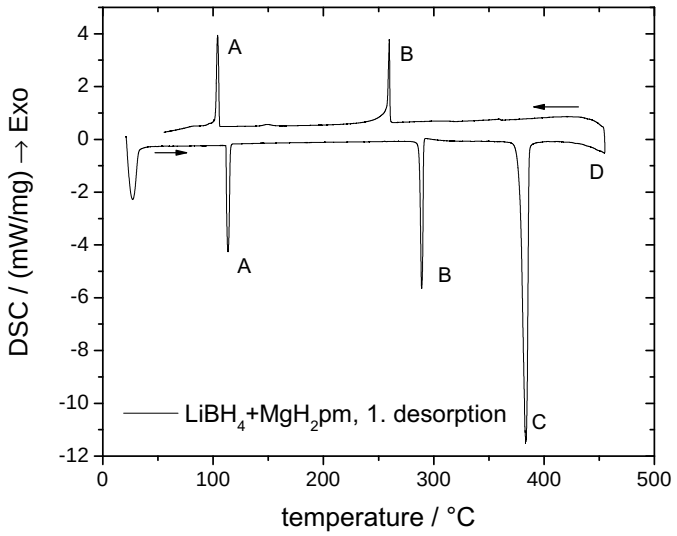

Figure 3.12: HP-DSC measurement $LiBH_4-MgH_2$ composite of the first desorption reaction, measured under 3 bar hydrogen and a heating rate of 5 K/min.

It must be noted, that an exothermic event caused by the formation of MgB_2 cannot be observed. For this there are two possible explanations. Either the endothermic desorption reaction of the $LiBH_4$ overlaps with the exothermic formation of MgB_2 or the formation of MgB_2 is very slow and occurs over a wide temperature range and hence does not display a clear peak.

The determination of the heat of reaction from the DSC measurements for these composites is not possible. The estimated values are unreasonably low as the desorption reaction is not finalized.

3.2.3 In-situ XRD

The intermediate state of the desorption reaction is suggested to correspond to the desorption of MgH_2 to metallic Mg, but confirmation of this intermediate state is necessary. This is achieved by in-situ XRD measurements. This method has the advantage that no changes due to quenching of the samples influence the results. The first desorption reaction of $LiBH_4-MgH_2$ composite with 5 mol% Vanadium-isopropoxide is illustrated in figure 3.13. As figure 3.15 shows, the reaction mechanism with and without additve is the same and figure 3.13 is therefore representative. The sample is measured under approximately 5 bar hydrogen and was heated to 400 °C and then kept isothermal.

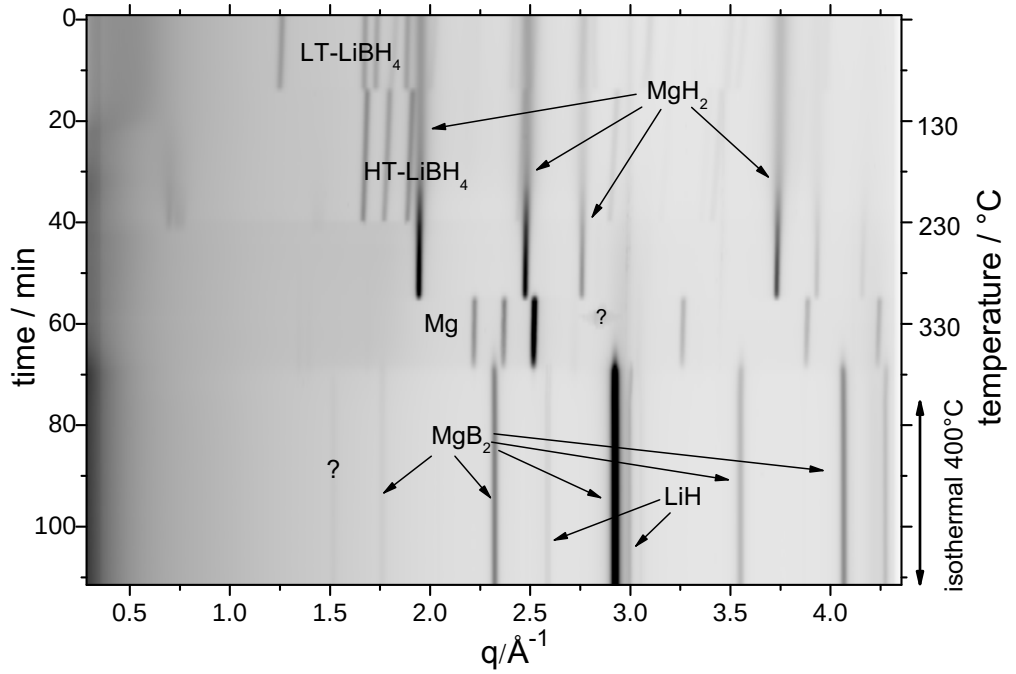

Figure 3.13: In-situ XRD of the first desorption reaction of $LiBH_4-MgH_2$ composites with 5 mol % Vanadium-isopropoxide under 5 bar hydrogen, heating to 400° C and then keeping isothermal. The measurement was obtained at the MAX-lab.

Clearly visible are the initial crystalline compounds $LiBH_4$ and MgH_2. No reflections from the additive phase or reaction products of the additive with the hydride matrix can be observed, which suggests a very fine distribution. At approximately 110 °C occurs the phase transformation of $LiBH_4$ from orthorhombic (LT) to hexagonal (HT) lattice structure. Upon further heating, at approximately 230 °C the $LiBH_4$ melts and it's decomposition cannot be followed further by X-ray diffraction. At temperatures of approximately 280 °C a fast desorption of MgH_2

into metallic Mg is observed. This points towards inaccuracy in the temperature measurement, because the decomposition temperature of MgH_2 under 5 bar hydrogen is known to be greater than 350 °C [64], for pure MgH_2 as well as for the composites. The formation of MgB_2 is observed very soon afterward, supposedly simultaneous to the desorption of $LiBH_4$. The quantitative description of this reaction is shown in figure 3.14(a). The fraction of the MgH_2 seems to increase before a very sharp transition into metallic Mg occurs. In reality, the fraction of MgH_2 cannot increase, the observed rise in the peak area is likely to be due to an increase in the crystalline fraction and due to coarsening/recrystallization of the MgH_2 crystallites. The metallic Mg reacts then to MgB_2, the decrease of the Mg peak takes place simultaneously to the formation of MgB_2. The results do not indicate a formation of a crystalline intermediate phase. For the orthorhombic $LiBH_4$ a small decrease in the phase fraction is observed before the first order phase transition into the hexagonal lattice structure takes place and at higher temperatures the melting occurs. The evolution of the crystallite sizes of MgH_2 and MgB_2 is plotted in figure 3.14(b). Significant coarsening and possibly recrystallization of MgH_2 starts at approximately 170 °C. The small jump in the phase fraction and crystallite size after approximately 15 min is likely to be due to the phase transition of $LiBH_4$, because the analyzed MgH_2 reflection is overlapping with a reflection of the orthorhombic $LiBH_4$. The crystallite size of MgB_2 is quite constant at a level of 18 nm. MgB_2 is stable for temperatures up to 1300 °C before decomposing into more boron rich compounds [65], therefore coarsening is less likely to take place than in the less stable MgH_2.

It should be noted, that the diffraction conditions need to be fulfilled, therefore small phase fractions and fine crystallites as well as amorphous phases, e.g., at the beginning of the phase-formation, cannot be observed.

The volumetric measurements suggest a simultaneous decomposition of $LiBH_4$ and formation of MgB_2 under a hydrogen back-pressure of 5 bar, because the equilibrium temperature for pure $LiBH_4$ is greater than 400 °C under 5 bar hydrogen. In-situ XRD measurements with a simultaneous record of the pressure are set up at the ESRF to verify this assumption. As the amount of sample is very small, the change in pressure is also very small, but nonetheless distinctly noticeable. In figure 3.15 selected patterns of pure $LiBH_4$−MgH_2 composites slowly heated to approximately 415 °C are shown. High resolution powder diffraction patterns are taken with 10 minutes measurement time for each pattern.

The initial composite is clearly visible with the orthorhombic room-temperature phase of $LiBH_4$ and a mixture of MgH_2 and γ-MgH_2. Upon heating the phase

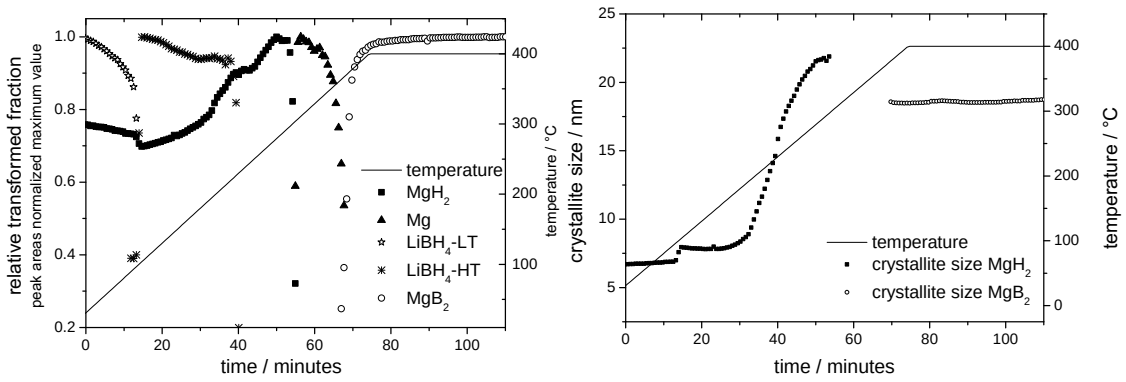

(a) phase fractions (b) crystallite sizes of the Mg-phases

Figure 3.14: Quantitative analysis of the phase fractions (a) and the crystallite sizes (b) of the Mg phases during the first desorption of $LiBH_4-MgH_2$ composites with 5 mol % Vanadium-isopropoxide under 5 bar hydrogen. The crystallite sizes were estimated using the Scherrer formula.

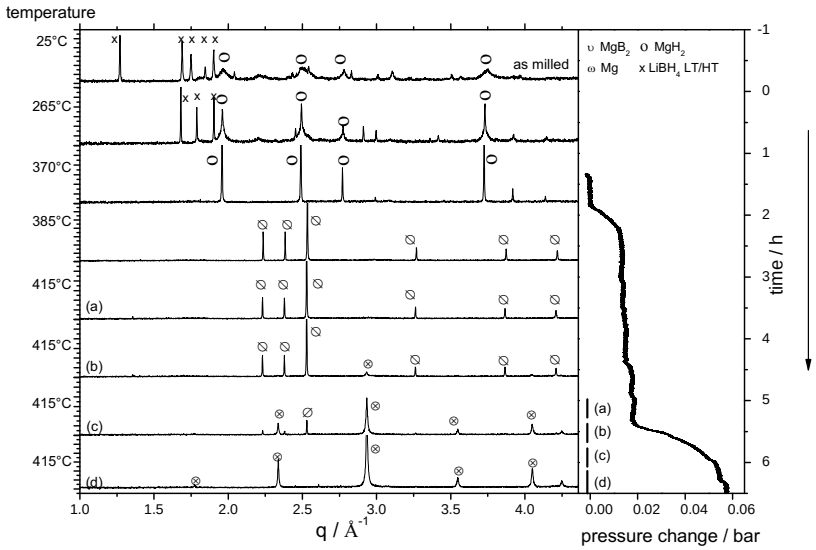

Figure 3.15: In-situ XRD and pressure record of the first desorption of pure $LiBH_4-MgH_2$ composites performed at the ESRF under approximately 5 bar hydrogen, heating to 415 °C and then keeping isothermal.

transformation and melting of the $LiBH_4$ can be observed. The peaks of the MgH_2 get narrower, relaxation and coarsening is taking place. At approximately 380 °C the desorption of MgH_2 occurs, accompanied by a slight change in pressure. Upon further slow heating and under isothermal conditions at approximately 410 °C only metallic Mg can be observed in the diffraction patterns for several hours. An "incubation" period like in the isothermal measurements in the titration apparatus is visible. Then, the simultaneous formation of MgB_2 and a significant change in pressure takes place, the desorption of $LiBH_4$ occurs simultaneous to the formation of MgB_2. This is illustrated by scans (a) through (d) and the corresponding pressure signal in the diagram on the right. During the incubation period, some small reflections at lower q values can be observed. They are discussed in section 4.1 with the other unidentified peaks of other in-situ measurements.

To investigate the effect of heating an experiment was performed with the conditions similar to those in the high-pressure DSC. A heating rate of 5 K/min was applied to a maximum temperature of the sample of approximately 490 °C under a hydrogen pressure of 3 bars. The results from this measurement is shown in figure 3.16.

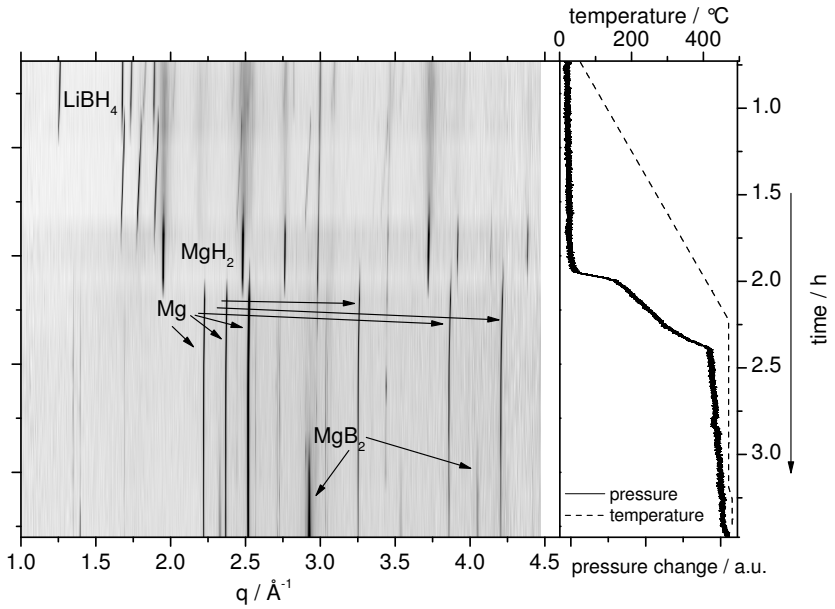

Figure 3.16: In-situ XRD and pressure record of the first desorption of pure $LiBH_4-MgH_2$ composites performed at the ESRF under approximately 3 bar hydrogen, heating to 480 °C with 5 K/min and then keeping isothermal.

Initial compounds of $LiBH_4$ and MgH_2 are clearly visible at the top of the diagram. Upon heating the phase transformation and melting of $LiBH_4$ occur. The increasing intensity of the MgH_2 reflections hint to significant coarsening of this phase. Upon further heating, the formation of Mg is observed. Under these conditions of 3 bar hydrogen the pressure trace shows a two step reaction without incubation period. Again, metallic Mg is present for several hours, before formation of MgB_2 is noted. It seems that the formation of MgB_2 is delayed, although metallic Mg is present. Free B is assumed to be present but it cannot be observed in the diffraction patterns. A detailed quantitative analysis or Rietveld refinement of the XRD patterns is not possible, because the scattered intensity was measured by point detectors and the sample could not be spun because of the pressure setup; homogeneity and random orientation can therefore not be assumed. A possible rate limiting step for the first desorption reaction of $LiBH_4$−MgH_2 composites under isothermal conditions is the delayed formation of MgB_2.

This observation is also supported by HP-DSC measurement of the pure $LiBH_4$-MgH_2 composite in comparison to the measurement of pure ball milled $LiBH_4$ measured under identical conditions of 3 bar hydrogen and a heating rate of 5 K/min shown in figure 3.17. The onset temperature of reaction D, the desorption of $LiBH_4$, is very similar in both experiments. For the composite, the onset temperature for reaction D is at approximately 390 °C while for the pure $LiBH_4$ it is at 380 °C. It is noted, that the reaction D in the composite is much more complete than for the pure $LiBH_4$ where reactions B and A are distinctly noticeable during the cooling. The Mg therefore influences the kinetics of the desorption of $LiBH_4$.

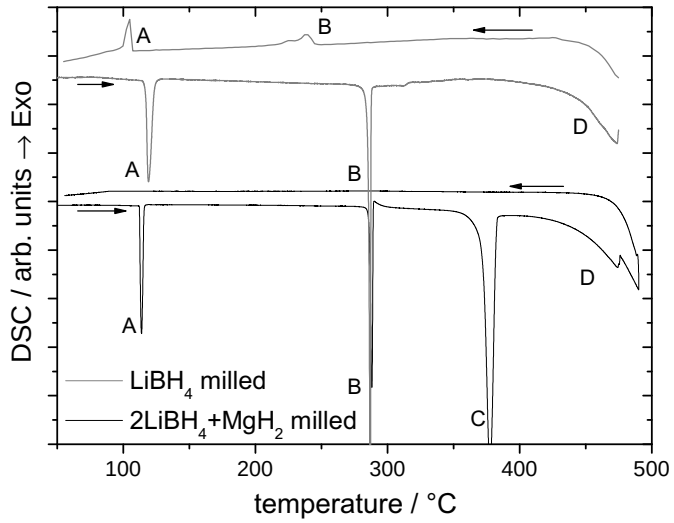

Figure 3.17: HP-DSC measurement of pure, milled $LiBH_4$ and of $LiBH_4$−MgH_2 composite, measured with 5 K/min and 3 bar hydrogen.

3.3 The first absorption reaction – kinetics and mechanism

3.3.1 Volumetric measurements

Reversible hydrogenation is one of the great advantages of the solid state metal hydrides. Therefore, in the following section the focus is put on the absorption reaction. In figure 3.18 the first absorption reactions of initial LiH−MgB_2 composites and previously desorbed $LiBH_4$−MgH_2 composites are shown. The measurements were performed at 350 °C and 50 bar hydrogen pressure and the sorption time is with 10-25 hours in the hour-to-day range for undoped material. But it is worth mentioning, that under these moderate conditions, the direct formation of $LiBH_4$ from the elements is not possible [66,67]. As already described in section 3.2.1, full rehydrogenation under these conditions is only possible from the correct reaction products LiH−MgB_2, otherwise, only the metallic Mg absorbs hydrogen.

It is noted, that the first absorption reaction after previous dehydrogenation is faster in comparison to the initial sorption reaction starting from as milled LiH−MgB_2 composites, thus hinting to a positive influence of the cycling on the microstructure. The smooth and monotonic increasing curves indicate a single step reaction mechanism in contrast to the two step desorption mechanism.

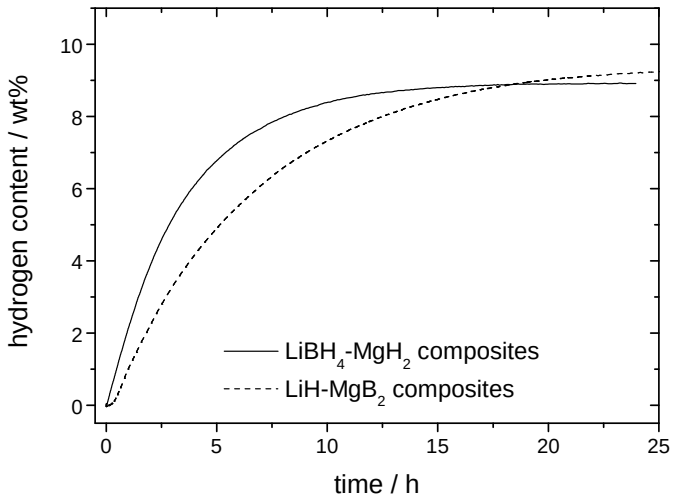

Figure 3.18: Volumetric measurement of the first absorption reaction of the pure LiH−MgB_2 composite and previously desorbed $LiBH_4$−MgH_2 composite at 350 °C and 50 bar hydrogen pressure.

3.3.2 Thermal analysis

More details on the ongoing reactions in the composite during the absorption of hydrogen can be revealed by the thermal analysis by high-pressure DSC. The black trace of the measurement in figure 3.19 represents the first absorption reaction of $LiH-MgB_2$ composites and shows here two exothermic events upon heating. The reactions occur in a wide temperature range, with an onset of the reaction X at approximately 250 °C. The second exothermic event Y is not concluded in the investigated temperature range but continues during the cooling segment. Upon cooling, the two distinct features of $LiBH_4$ appear, the exothermic solidification and polymorphic phase transition. Therefore, a successful hydrogenation reaction took place under 50 bar hydrogen and heating to 450 °C. This is also proven by the following desorption reaction represented by the gray trace in figure 3.19, again showing the characteristic phase transformation and melting of $LiBH_4$ and then the desorption reactions C and D. During the cooling, no exothermic peaks from $LiBH_4$ can be observed, the desorption reaction was complete in the investigated temperature range. In comparison to the first desorption of the as prepared $LiBH_4-MgH_2$ composites, see figure 3.12, the onset temperature for reaction C is lowered by approximately 20 K and for reaction D by 35 K. The determination of the onset for reaction D in figure 3.19 is difficult, because reactions C and D merge into each other. These results also hint towards improving sorption kinetics upon cycling.

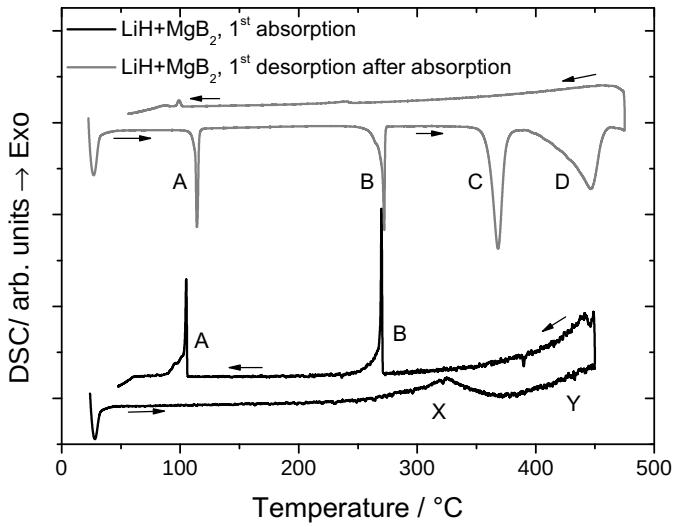

Figure 3.19: First full sorption cycle of $LiH-MgB_2$ composites, first absorption measured under 50 bar hydrogen, first desorption measured under 3 bar hydrogen, heating rate in both cases 5 K/min.

The origin of the two peaks during the absorption reaction in the HP-DSC remains unclear. The intensity of the two exothermic peaks X and Y varies with the sample and cycle. In the selected sample for detailed investigation only a weak X peak was observed with an onset temperature of approximately 250 °C, see figure 3.20(a). The reaction Y is not completed during the heating segment and continues during the cooling. The cooling segment as well as the following desorption reaction reveals the known features of the composites A, B, C and D as described above. Sample material from the same batch was heated under 50 bar of hydrogen to a maximum temperature of 320 °C, figure 3.20(b). The cooling segment indicates a small exothermic event at approximately 100 °C, which may correspond to the phase transformation of freshly formed $LiBH_4$. The following desorption measurement under 3 bar hydrogen reveals two small endothermic events at 100 °C and 240 °C which may correspond to the phase transformation and melting of $LiBH_4$. The third endothermic event at approximately 420°C may then correspond to the combined desorption of $LiBH_4$ and MgH_2. It occurs at higher temperatures than the individual desorption of MgH_2, observed in figure 3.20(a). The presence of MgH_2 is likely because the Mg is expected to react immediately to MgH_2 under the applied conditions when the MgB_2 reacts. The observed thermal events are much smaller than in the composites heated to higher final temperatures and allow therefore only limited conclusions. The variation in the intensity of two exothermic peaks suggests a separation of the reaction due to kinetic restrictions. Furthermore, the formation of BH_4^- tetrahedra, corresponding to amorpous $LiBH_4$ in $LiH-MgB_2$ composites was observed by Raman spectroscopy after keeping the sample at 265 °C under 90 bar hydrogen for 5 h by Wan et al. [68]. All my other investigations by in-situ XRD and volumetric measurements in a Sievert's apparatus support a one-step reaction character.

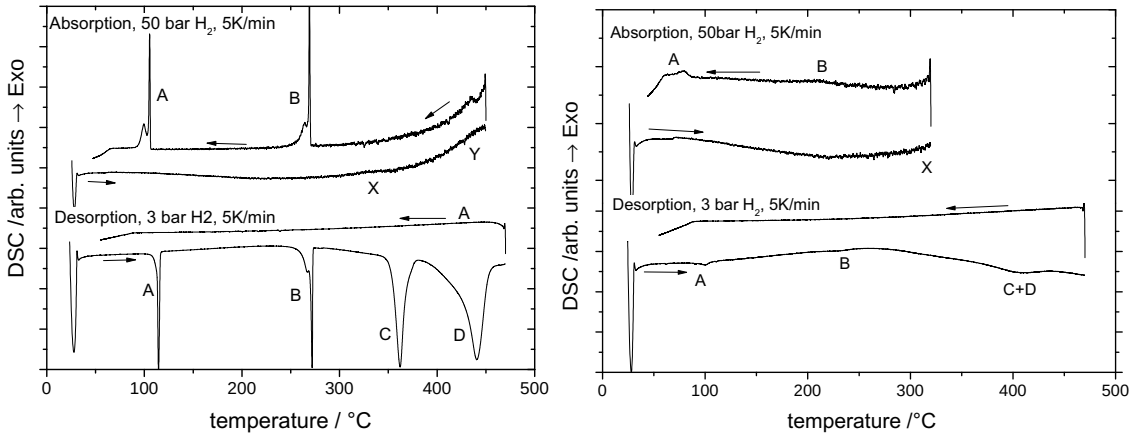

(a) heating to 450°C (b) heating to 320°C

Figure 3.20: HP-DSC investigation of the absorption behavior of LiH−MgB_2 composites, measured under 50 bar hydrogen heating to 450 °C and 320 °C in figure (a) and (b) respectively. The second trace displays the following desorption measurement under 3 bar hydrogen.

3.3.3 In-situ XRD

To investigate further on the reaction mechanism of the absorption reaction, in-situ XRD measurements were performed. Figure 3.21 shows the first absorption reaction of pure LiH−MgB_2 composites under 150 bar hydrogen, heated to 265 °C, then kept isothermal for 5 hours and finally cooled to room temperature. The temperature was chosen to observe also the formation of crystalline $LiBH_4$, since it is just below the melting point. This was however not possible, the formation of $LiBH_4$ was only observed after cooling to temperatures below 215°C. However, the limited accuracy of the temperature control, does not allow conclusions, whether the newly formed material has a lower melting point or whether the temperature measurement was inaccurate.

The reflections of the initial compounds of LiH and MgB_2 can be followed throughout the experiment. After a short time, reflections for the MgH_2 can be observed, the increasing intensity shows the reaction progress, this is quantitatively plotted in figure 3.22.

The evolution of the Mg-containing phase fractions directly correlate to each other. Therefore, a one step absorption reaction with a direct reaction of MgB_2 to MgH_2 is assumed. The then released boron is expected to form $LiBH_4$ with the free LiH directly. Since the reflections of $LiBH_4$ cannot be observed until cooling, there is no proof for this assumption. In figure 3.22 (b) the evolution of the crystallite

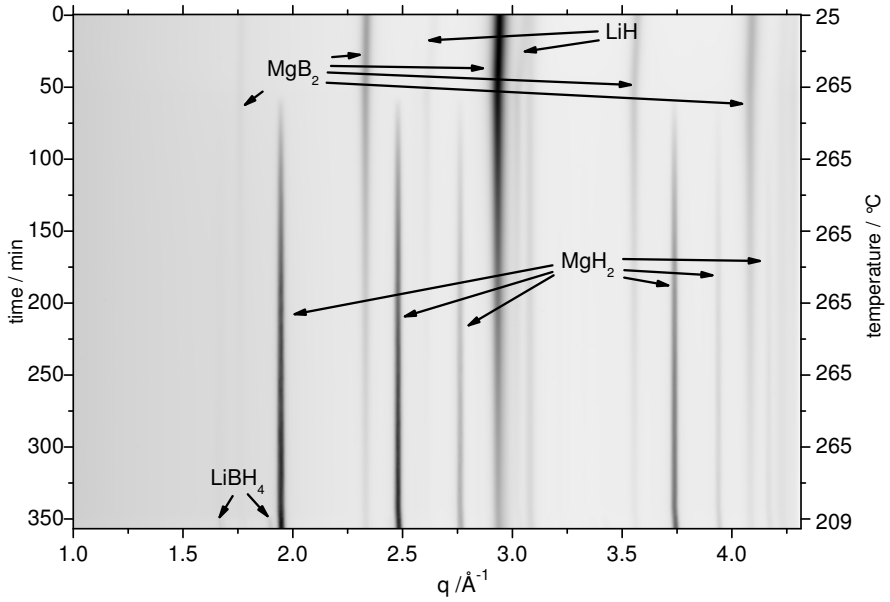

Figure 3.21: In-situ XRD of the first absorption reaction of pure LiH−MgB_2 composites under 150 bar hydrogen, heating to 265° C , then keeping isothermal for five hours and cooling to room temperature.

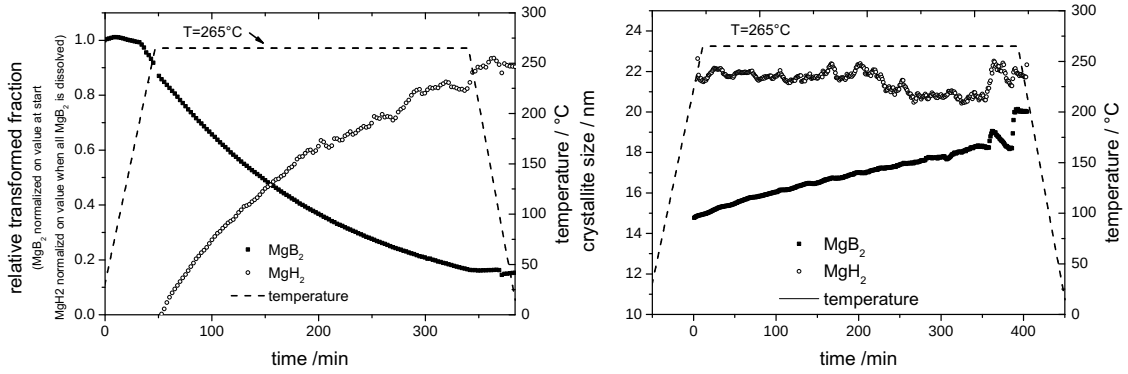

(a) phase fractions

(b) crystallite sizes

Figure 3.22: Quantitative analysis of the Mg-phase fractions (a) and the crystallite sizes (b) during the first absorption of LiH−MgB_2 composites under 150 bar hydrogen at 265 °C

size is shown. For the MgB_2 a slight growth of the crystallites can be observed during the reaction whereas the crystallite size of MgH_2 remains constant. This observation for the MgH_2 is slightly surprising, because the temperature is higher than the temperature where the starting of the coarsening of MgH_2 in the first desorption reaction was observed. The study suggests, that MgB_2 has a stabilizing effect on the crystallite size of MgH_2.

3.4 Influence of additives in $LiBH_4$–MgH_2 and LiH–MgB_2 composites

The following section focuses on the beneficial effect of additives on the sorption kinetics. The investigations include the phenomenological description of the effect for transition-metal as well as light-metal based additives and an exemplary study on the chemical state, size and location of Zr-based additives.

Transition-metal based additives are known to play a crucial role for the reaction kinetics and reversibility of light-metal hydrides such as MgH_2 and $NaAlH_4$ [7, 18]. The volumetric experiments focus on the first desorption reaction because of the most similar starting conditions. With additives, the lengthy incubation period can be overcome. Detailed investigations on the chemical state after milling and after cycling are performed exemplarily for Zr-based additives by XANES. For these, typical sizes are estimated by ASAXS measurements. The location of the Zr is addressed by TEM investigations. The combination of these methods gives a comprehensive overview on the chemical state, size and location of the additive.

The investigations on the effect of light-metal based additives such as oxides and hydroxides is motivated by the observed limited reproducibility and aging of samples.

One possible origin for the observed incubation period during the first desorption reaction is restricted nucleation of MgB_2. This is investigated with additives supporting heterogeneous nucleation, such as surplus material of the final reaction products (LiH and MgB_2). This is discussed in detail in section 4.2.

3.4.1 Transition-metal based additives

In figure 3.23 the significant influence of transition-metal based additives on the sorption kinetics is demonstrated. The sorption time can be reduced by an order of magnitude from about 30h to 1.5 hours and the incubation period is significantly reduced or even eliminated. However, under the applied measuring conditions of 400 °C and 5 bar hydrogen the reaction proceeds in two steps with the intermediate formation of metallic Mg. The changes in the hydrogen storage capacity correspond to the additional weight of the additives.

Different compounds on the basis of the transition-metal titanium are studied. Here, the effect of $TiCl_3$, TiB_2 and Ti-isopropoxide are investigated to clarify the influence of the anion. Furthermore, compounds on the basis of different transition-metals such as titanium, vanadium and zirconium are studied to investigate the

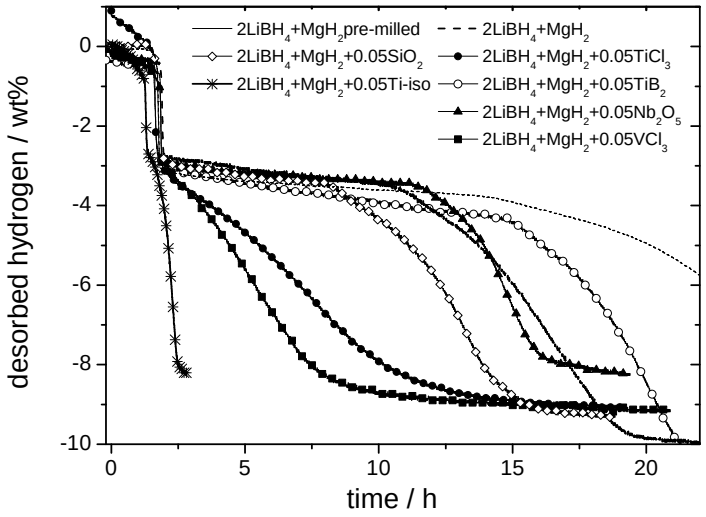

Figure 3.23: Volumetric measurement of the first desorption reaction of $LiBH_4$−MgH_2 composites with 5 mol% of various transition-metal based additives. The as milled samples are measured under 5 bar hydrogen and are heated to 400 °C and then kept isothermal.

influence of the cation. Additionally, several transition-metal based additives with a known positive influence on the reaction kinetics like Nb_2O_5 (known for MgH_2 [8]) and SiO_2 (known for $LiBH_4$ [58, 59, 69]) were tested. To allow better comparison, the measurements are grouped in figure 3.24 according to the transition-metal or the anionic-group (oxide, chloride, isopropoxide).

Titanium-based compounds (figure 3.24(a)) all show a significant effect on the sorption kinetics. While the isopropoxide and the chloride completely overcome the incubation period, it is still existent but significantly reduced with additional TiB_2. The isopropoxide as well as the chloride are highly reactive and are therefore likely to react with the hydride matrix during milling or during the sorption reaction to form more stable compounds. TiB_2 is thermodynamically very stable and also mechanically one of the hardest known compounds. Both of these parameters may influence the distribution and crystallite sizes within the composite. A reaction of the additive with the hydride is likely to advance their distribution. The chemical state of the additive is treated in more detail for Zr-based additives in the following section 3.4.1.1. It is noted, that none of the additives, except for the TiB_2 and Sc_2O_3, can be observed in the XRD patterns after milling. This indicates small crystallite sizes and a very fine distribution. The influence on the hydrogen storage capacity in dependence of the molecular weight of the additive is clearly visible.

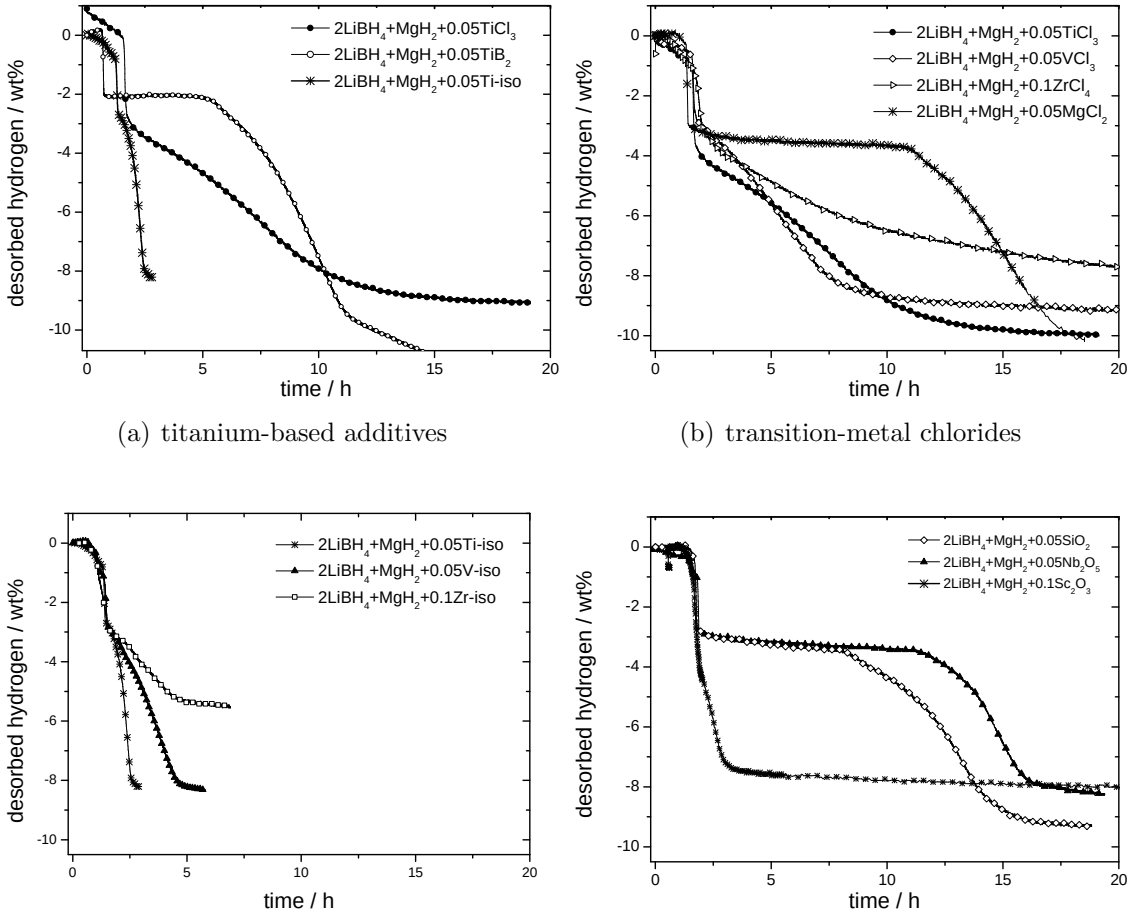

(a) titanium-based additives

(b) transition-metal chlorides

(c) transition-metal isopropoxides

(d) oxides as additives

Figure 3.24: Effect of various transition metal based additives on the first desorption reaction of $LiBH_4-MgH_2$ composites measured in a Sievert's type apparatus under 5 bar hydrogen and heating to 400 °C and then holding isothermal. The amount of additive was 5 mol% unless noted otherwise.

For example, the gravimetric capacity with 10 mol% additional $ZrCl_4$ is reduced to approximately 8 wt%.

Composites with additional Ti-isopropoxide display the highest reaction rates of all additives, 3.24(c). The isopropoxides are highly reactive compounds, a reaction with the hydride matrix during milling or the first sorption reaction is therefore likely. It should be noted, that in case of Zr-isopropoxide, only a Zr-isopropoxide-isopropanol complex was available.

In comparison of the different transition-metal chlorides (figure 3.24(b)), all overcome the incubation period contrary to the addition of $MgCl_2$ which only reduces

the incubation period by few hours. However, it shows the highest reaction rates of the chlorides.

For additional Nb_2O_5 and SiO_2 only a small effect on the incubation period is visible, figure 3.24(d). Additional Nb_2O_5 catalyzes the desorption reaction of the MgH_2 and thus lowers the onset temperature. Also, for the desorption of the $LiBH_4$ a faster reaction is measured. The addition of SiO_2 has a small effect on the reaction kinetics, despite its known effect on pure $LiBH_4$ [58, 59]. In higher concentrations, SiO_2 is known to react with $LiBH_4$ to form a stable ternary oxide [70]. Of the additional oxides, Sc_2O_3 displays very high reaction rates and the incubation period is completely overcome.

Despite the high thermodynamic stability of Sc_2O_3 with -1908 kJ/mol [71], this compounds reacts with the hydride matrix. The reaction was observed by in-situ XRD under 5 bar hydrogen, see figure 3.25. The initial crystalline phases are $LiBH_4$, MgH_2 and Sc_2O_3. Upon heating the phase transformation and melting of the $LiBH_4$ can be observed. At higher temperatures the desorption of MgH_2 into metallic Mg takes place and then MgB_2 forms. The reflections from the Sc_2O_3 with a scattering vector around 1.5 $Å^{-1}$and 3.5 $Å^{-1}$show a distinctly decreased intensity compared to the initial reflections. The weakening starts approximately after the melting of the $LiBH_4$ at 110 °C.

Analysis of the final pattern for a new Sc containing phase gives no satisfactory result. Possible are the formation of ternary oxides such as $ScMg_2O_4$ [72] or $LiScO_2$ [73] as well as Scandium boride ScB_2. For the ternary oxides no thermodynamic data is available. The formation of ScB_2 is thermodynamically favorable, under the condition that the compounds react partially to ScB_2 and MgO. Confirmation of present ScB_2 by XRD is not possible for these composites, because the crystal lattice of ScB_2 is almost a complete match of the MgB_2 lattice.

3.4.1.1 Chemical state of Zr-based additives

The previous section illustrated strong effect of the additives on the sorption kinetics as well as the high reactivity and reduction power of the of the hydride matrix. The approach was mainly phenomenological and the results allow only limited conclusions on the mechanism behind the influence of the additives on the sorption kinetics. For this, reliable knowledge about the chemical state, size and distribution are mandatory. The first question of the chemical state is addressed exemplarily for Zr-based additives in the following section by a qualitative evaluation of the XANES measurements. The isopropoxide and chloride additives as well as the hydride

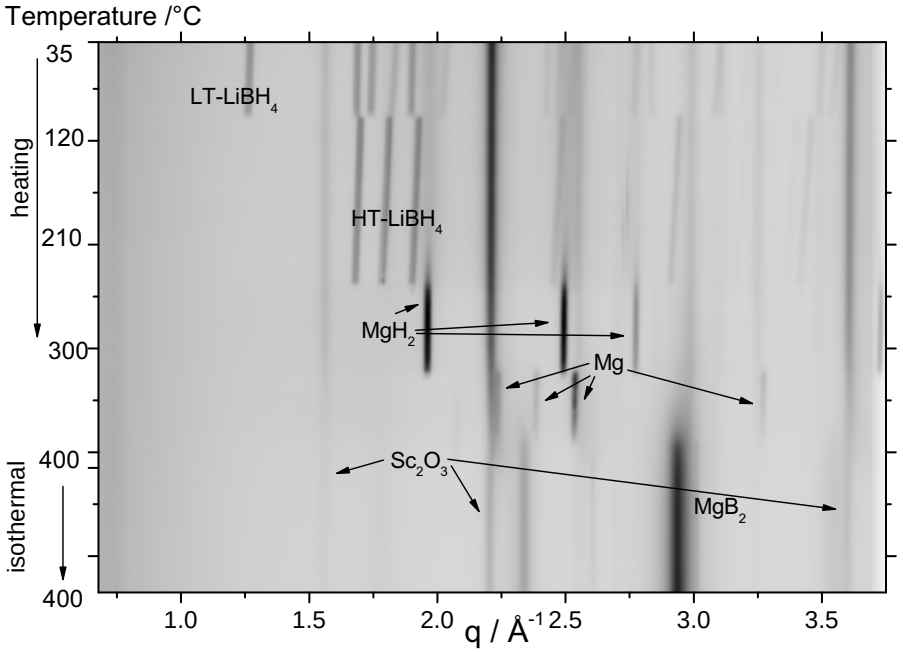

Figure 3.25: In-situ XRD during desorption of $LiBH_4$−MgH_2 composites with 10 mol% Sc_2O_3 under 5 bar hydrogen, heating to 400 °C and then keeping isothermal.

matrix are highly reactive. An inert state during high energy ball milling and during the sorption reactions of the additives is therefore unlikely. To investigate the reaction products and the time of formation XAS was performed on the as milled samples as well as on samples after one and two sorption reactions. Conclusions on the stability of the reaction products can then also be drawn. A qualitative analysis of the XANES spectrum is performed by comparison to reference materials. It should be noted, that neither after milling nor after the first sorption reaction, a Zr-containing phase could be observed from the X-ray diffraction patterns. This already indicates a very fine distribution and small crystallite sizes or amorphous state.

In figure 3.26 the X-ray absorption spectra of the Zr-K-edge for the samples and references, the XANES curves, are shown. The curves obtained for the materials prepared with additional $ZrCl_4$ (3.26(a) and (b)) show little similarity to the initial absorption edge of $ZrCl_4$.

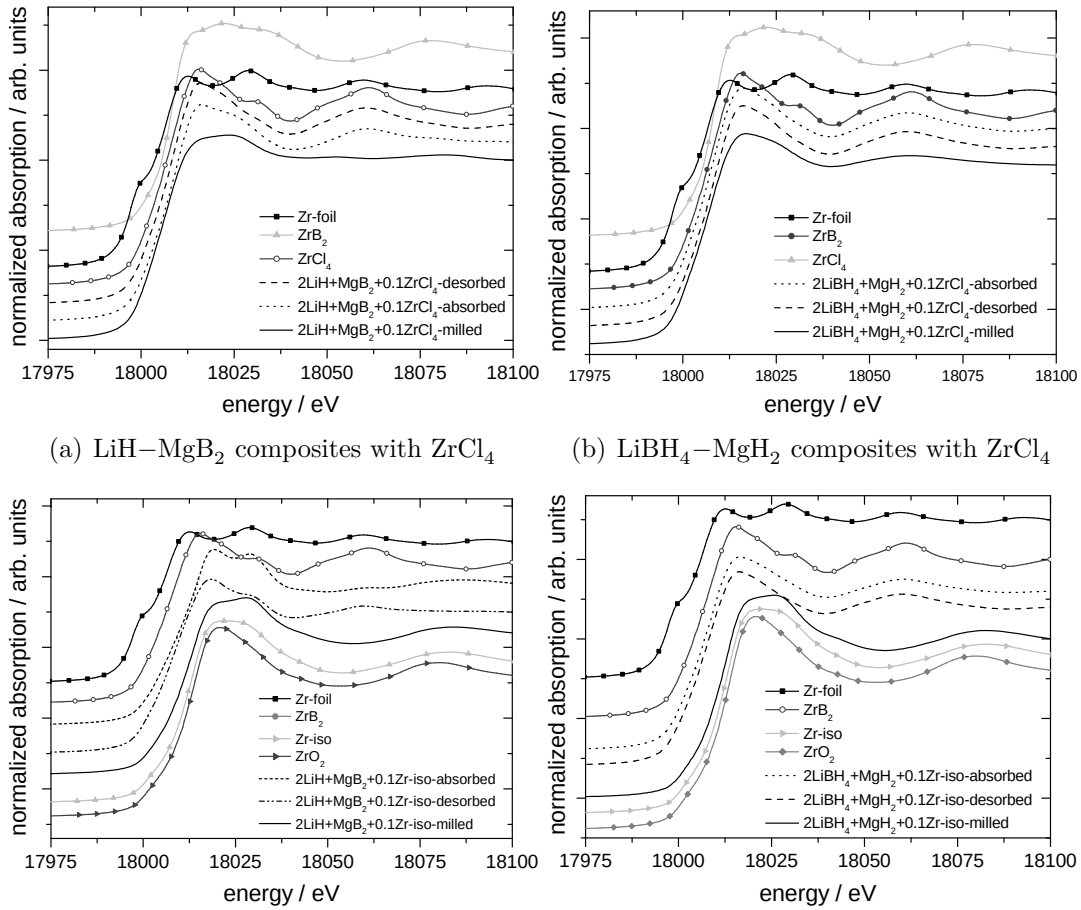

(a) LiH−MgB_2 composites with $ZrCl_4$

(b) $LiBH_4$−MgH_2 composites with $ZrCl_4$

(c) LiH−MgB_2 composites with Zr-iso

(d) $LiBH_4$−MgH_2 composites with Zr-iso

Figure 3.26: XANES curves of the samples with the respective additives. The curves are shifted vertically for better visualisation

For all samples with additional $ZrCl_4$ the position of the edge is similar, also in the cycled states. The edge positions are quantified in table 3.1. There are some variations in the amplitude of the oscillations in the post-edge region, which are probably due to the nanocrystalline state of the compound. The materials are apparently reduced during the milling, however not to metallic Zr, because the absorption edge is only slightly shifted to lower energies than that of the edge position of $ZrCl_4$ but not to the value of metallic Zr. The state is stable upon further cycling. For these samples, the formation of ZrB_2 is proposed. This is illustrated in figure 3.27 by the difference curves of milled and cycled $LiBH_4$−MgH_2 composites with 10 mol% $ZrCl_4$ to pure $ZrCl_4$ and ZrB_2. Both samples show a very high similarity to ZrB_2 and significant differences to the initial $ZrCl_4$. The chlorine reacts with lithium to form LiCl.

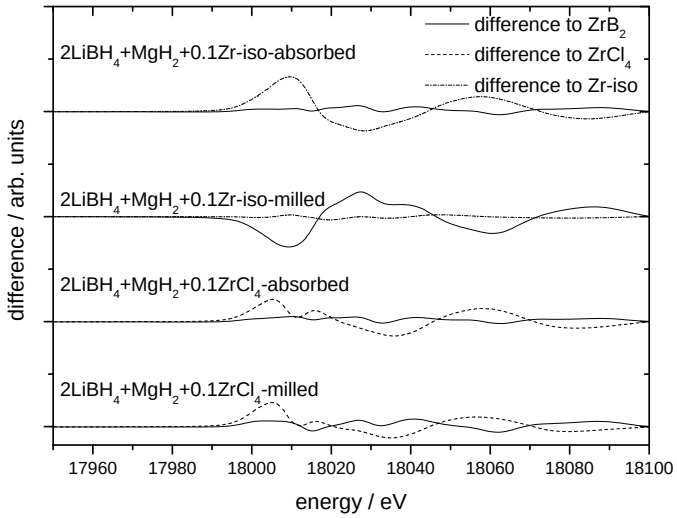

Figure 3.27: Difference curves of the XANES measurements for four selected samples of the sample to ZrB_2, Zr-iso or $ZrCl_4$

For the samples containing Zr-iso as an additive, see figure 3.26(c) and (d), there seem to be no significant changes of the chemical state during the preparation by high energy ball milling. The XANES curve of the milled samples shows very high similarity to the one of pure Zr-iso, which is also illustrated in figure 3.27. In the X-ray diffraction patterns very similar reflections to those of the as received Zr-iso are observed. The Zr-iso is not stable during the first sorption reaction, a reduction of the chemical oxidation state is revealed for the initial $LiH-MgB_2$ composites as well as for the initial $LiBH_4-MgH_2$ composites in the XANES measurements. The shift of the absorption edge with the first sorption reaction to lower energies is quantified in table 3.1. Besides the oxidation state, the bonding within the compound has changed as well. This is indicated by the post-edge peak positions. For example in the region of 18060 eV the curves of the milled samples show minima whereas after the first sorption reaction, maxima are displayed. The formation of stable ZrB_2 is proposed for the $LiBH_4-MgH_2$ composites with Zr-iso during the first sorption reaction. The difference curve of the sample to the ZrB_2-reference is almost zero. $LiH-MgB_2$ composites with additional Zr-iso show similarity to the ZrB_2 but there are additional features to be noted, e.g. around 18030 eV. Partial oxidation and formation of ZrO_2 or stable Zr-iso leading to an overlay of the Zr absorption features is likely to be the origin of this observation. These results agree very well with the observations of Ignatov et al. [74], who observed the formation of stable amorphous TiB_2 in $LiBH_4-MgH_2$ composites with additional $TiCl_3$ by EXAFS.

Sample	f'	f''	edge position / eV
$2LiBH_4+MgH_2+0.1\ ZrCl_4$ -absorbed	-3.05	0.56	18008
	-7.84	2.47	
$2LiBH_4+MgH_2+0.1ZrCl_4$ -desorbed	-3.05	0.56	18008
	-7.78	2.5	
$2LiBH_4+MgH_2+0.1ZrCl_4$ -milled	-3.06	0.56	18007
	-7.63	1.91	
$2LiBH_4+MgH_2+0.1$Zr-iso-absorbed	-3.04	0.56	18009
	-7.51	1.46	
$2LiBH_4+MgH_2+0.1$Zr-iso-desorbed	-3.04	0.56	18009
	-7.51	1.48	
$2LiBH_4+MgH_2+0.1$Zr-iso-milled	-3.02	0.56	18012
	-7.05	1.02	
$LiH+MgB_2+0.1ZrCl_4$- absorbed	-3.02	0.54	18009
	-7.63	2.22	
$LiH+MgB_2+0.1ZrCl_4$- desorbed	-3.02	0.54	18009
	-7.65	2.32	
$LiH+MgB_2+0.1ZrCl_4$- milled	-3.03	0.54	18006
	-7.25	1.8	
$LiH+MgB_2+0.1$Zr-iso- absorbed	-3.05	0.56	18007 & 18014
	-7.76	2.48	
$LiH+MgB_2+0.1$Zr-iso- desorbed	-3.04	0.56	18009
	-7.36	1.29	
$LiH+MgB_2+0.1$Zr-iso- milled	-2.99	0.51	18013
	-6.92	0.96	
Zr-powder			17998
ZrB_2			18008
$ZrCl_4$			18009
Zr-iso			18012

Table 3.1: Anomalous dispersion corrections obtained from the XANES measurements and the experimentally determined absorption edge position for each sample

3.4.1.2 Typical sizes for Zr- and V-based compounds

Besides the chemical state, size, distribution and location of the additives are key issues to find the origin for their effect on the sorption kinetics. To obtain information on the sizes of the Zr-compounds, ASAXS measurements were performed at the Zr-K edge. Ti and, as it was revealed during the measurements, V-additives in combination with this reactive hydride composite are below the limit of the reliable range of the instrument at beamline B1, Hasylab, DESY. The location of the Zr phases is addressed in the following section 3.4.1.3, where the images obtained by electron microscopy are presented.

In figure 3.28 the obtained separated scattering curves from the ASAXS measurements are shown for all Zr-containing samples. The shown data points correspond only to the scattering contribution of the Zr-containing structures. The symbols present the experimental data and the lines the fits according to equation 2.7. The determined anomalous dispersion corrections for each sample corresponding to the measuring energies are noted in table 3.1. They describe the strong dependency of the scattering on the energy close to the absorption edge to an element. The correlation lengths for the phases obtained by fitting to the scattering curves are listed in table 3.2. For the analysis, the formation of stable ZrB_2 is assumed, see section 3.4.1.1. By using the estimated volume fraction of ZrB_2 the characteristic lengths of the two phases, ξ_α and ξ_β are calculated. However, the value of the volume fraction is not known exactly, it was estimated under the assumption of homogeneous chemical state throughout the sample and complete reaction. The porosity of the powder was neglected and bulk density assumed. Due to these assumptions, the characteristic matrix-length ξ_α can only serve as a guideline. However, it matches well the estimated crystallite sizes from the XRD patterns.

The composites with additional Zr-iso reveal a distinct peak in the measured q range. This is a Bragg peak of Zr-iso, the reflection in the milled material is very similar to the one observed in the received material. Besides this peak, no scattering contribution is measured in the large q region but a scattering contributions from larger structures is observed in the lower q region. Upon cycling, the Bragg-peak disappears and a scattering contribution in the q range corresponding to a few nm sizes is measured. A very broad shoulder around 2 nm^{-1} can be noticed after the first sorption reaction and it is apparently stable during further sorption reactions. The scattering is due to structures in the size range of several nm. This observation was made for all cycled Zr-iso containing samples.

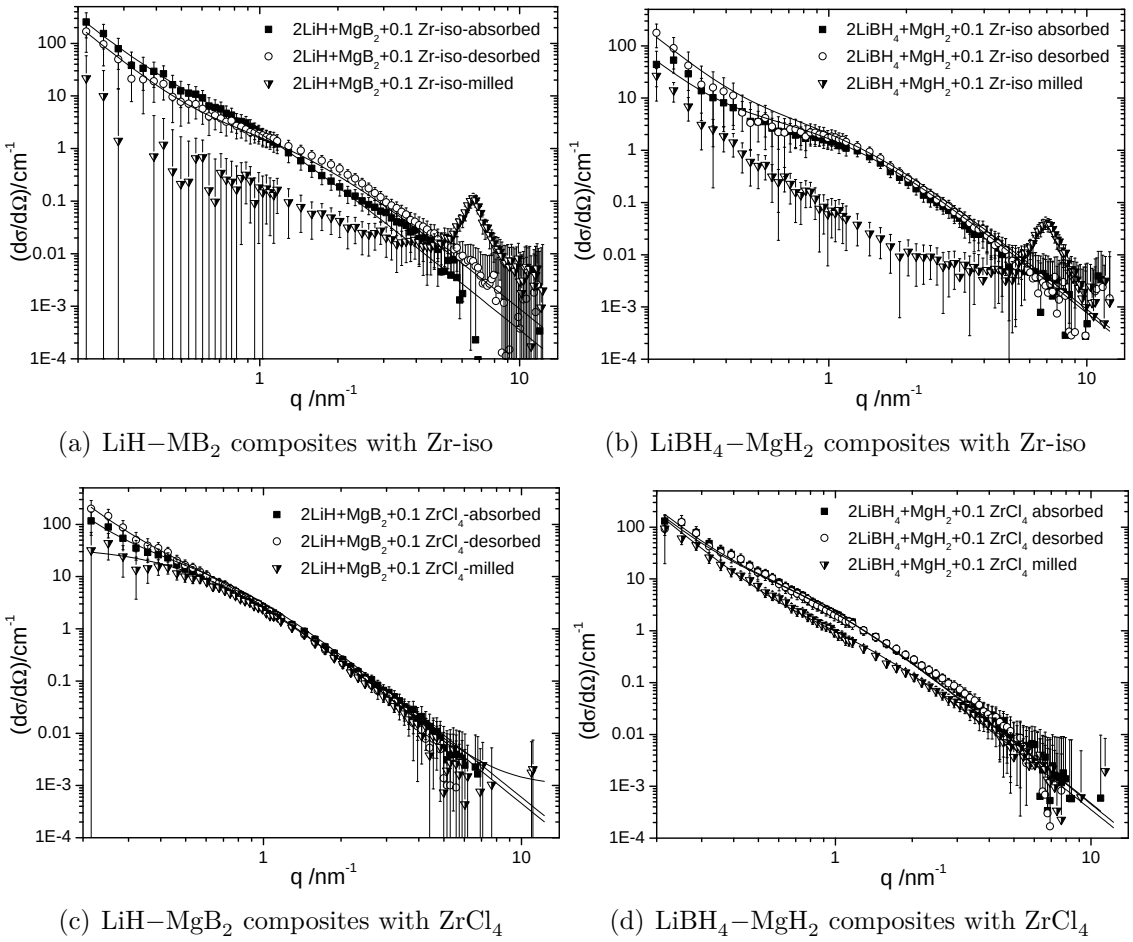

(a) LiH−MB_2 composites with Zr-iso

(b) $LiBH_4$−MgH_2 composites with Zr-iso

(c) LiH−MgB_2 composites with $ZrCl_4$

(d) $LiBH_4$−MgH_2 composites with $ZrCl_4$

Figure 3.28: ASAXS separated curves for the as as prepared and cycled composites. The symbols represent the measured data whereas the lines correspond to the obtained fit applying the Debye-Bueche model described by equation.

In the separated curves with additional $ZrCl_4$ already after milling a scattering contribution in the interesting q range can be observed. The scattering structures seem to remain stable upon further cycling. For the composites of initial LiH−MgB_2 an increase of the scattering signal in the low q region is observed with further sorption reactions, this is likely to be caused by larger structures like agglomerates and such. Again, characteristic lengths on the scale of 1-3 nm are obtained.

From this analysis, it is assumed, that the formation of stable ZrB_2 nanostructures takes place during milling (with additional $ZrCl_4$) or upon cycling (with additional Zr-iso).

Similar investigations were performed with V-based additives. Due to the poorer detector sensitivity at the energy of the vanadium K-edge, only the scattering

Sample	correlation length a (nm)	Volume fraction Φ_β	ξ_β (nm)	ξ_α (nm)
$2\,LiBH_4 + MgH_2$+0.1$ZrCl_4$-absorbed	1.4	0.023	1.4	61
$2\,LiBH_4 + MgH_2$+0.1$ZrCl_4$-desorbed	1.4	0.04	1.4	35
$2\,LiBH_4 + MgH_2$+0.1$ZrCl_4$-milled	0.9	0.23	0.9	39
$2\,LiBH_4 + MgH_2$+0.1Zr-iso-absorbed	0.9	0.03	0.9	30
$2\,LiBH_4 + MgH_2$+0.1Zr-iso-desorbed	0.9	0.03	0.9	30
$2\,LiH + MgB_2$+0.1$ZrCl_4$-absorbed	1.6	0.023	1.6	70
$2\,LiH + MgB_2$+0.1$ZrCl_4$-desorbed	1.7	0.04	1.8	43
$2\,LiH + MgB_2$+0.1$ZrCl_4$-milled	1.8	0.04	1.9	45
$2\,LiH + MgB_2$+0.1Zr-iso-absorbed	1.5	0.03	1.5	50
$2\,LiH + MgB_2$+0.1Zr-iso-desorbed	0.8	0.03	0.8	27
$2\,LiH + MgB_2$+0.1VCl_3-absorbed	2.0	0.03	2.1	40
$2\,LiH + MgB_2$+0.1VCl_3-desorbed	2.4	0.03	2.5	60
$2\,LiH + MgB_2$+0.1VCl_3-milled	2.0	0.03	2.1	40

Table 3.2: Characteristic length obtained by fitting with the Debye-Bueche model

results from the sample set of LiH−MgB_2 composites with 10 mol% VCl_3 could be reliably analyzed. The results show a high similarity to those obtained for the Zr-based additives. In figure 3.29 the scattering contribution of the V-containing structures is shown. The symbols present the experimental data points whereas the lines represent the modeled curve obtained by fitting equation 2.7. The resulting correlation lengths are noted in table 3.2.

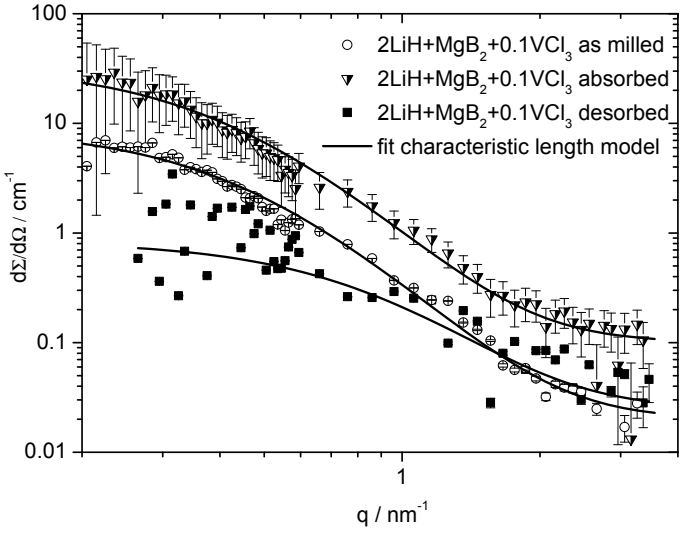

Figure 3.29: ASAXS separated curves for LiH−MgB_2 composites with 10 mol% VCl_3 in the milled, absorbed and desorbed state.

For the broad shoulder in the samples containing Zr-iso as an additive, Fourier transformation was performed to obtained the distance distribution function using the GNOM program [75]. The fit and the corresponding distance distribution function is shown in figure 3.30. This method has the advantage of displaying a probability for maximum lengths present in the sample. It can be interpreted as a type of a size distribution. The maximum is found around 2 nm and the maximum length is at approximately 4 nm. This is in good agreement with the previously reported characteristic lengths. The scattering data from the low q values was neglected for this analysis.

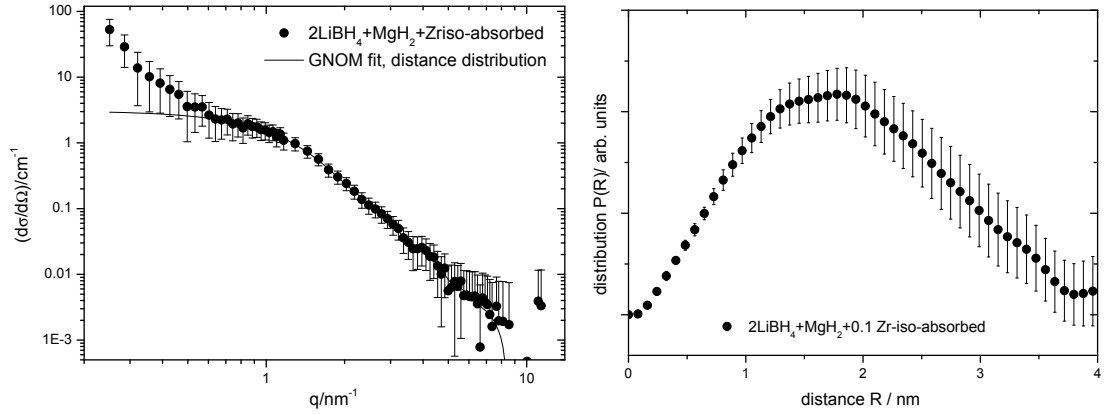

(a) seperated scattering curve (b) distance distribution

Figure 3.30: Separated ASAXS curve for LiH−MgB_2 composites with 10 mol% Zr-iso in the absorbed state and the corresponding distance distribution using the GNOM program

3.4.1.3 Location of the transition metal additives in LiH−MgB_2 composites

The location of the additives is an important step towards the identification of their effect on the sorption reactions. ASAXS and XANES measurements (see section 3.4.1.2 and 3.4.1.1) indicated a formation of ZrB_2 nanoparticles, but this as well as their location in the composites need confirmation. Access to information on the phase distribution is difficult due to the nanoscale character of the composites in combination with light elements and high sensitivity to air and water. First investigations in the micrometer size range were performed by scanning electron microscopy (SEM). To obtain higher resolution and thus information on the nanometer size range of the materials, transmission electron microscopy was performed on as milled and cycled samples.

In figure 3.31 micrographs of desorbed $LiBH_4-MgH_2$ composite with 5 mol% $TiCl_3$ and Ti-iso are presented. Figure 3.31(a) the SEM image displays a plate-like structure with connections forming a three dimensional network of the sample. Similar to the milled $LiH-MgB_2$ composite, figure 3.1, a fractal structure can be observed. Identification of the phases by EDX is not possible. From XRD patters typical crystallite sizes of the MgB_2 in the range of 50 nm are known. Similar, the sample investigated by TEM, figure 3.1 (b) shows a plate like structure, but the network structure can not be observed in this resolution. Phase separation occurs on a scale smaller than 100 nm.

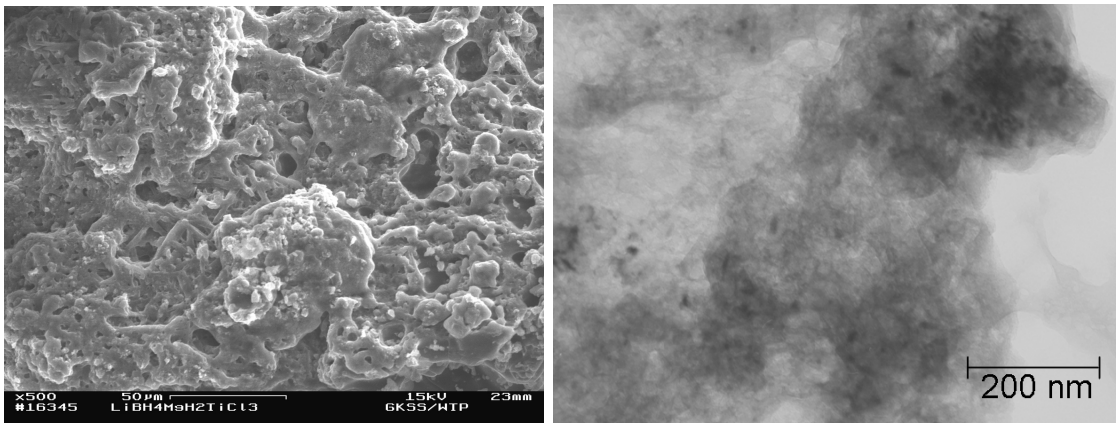

(a) SEM image (b) TEM image

Figure 3.31: SEM micrograph of desorbed $LiBH_4-MgH_2$ composite with additional 5 mol% $TiCl_3$ and TEM image of desorbed $LiBH_4-MgH_2$ composite with additional 5 mol% Ti-iso.

Further measurements on the cross-section of as milled $LiH-MgB_2$ composites with 10 mol% $ZrCl_4$ by SEM show very good homogeneity of a two phase mixture, see figure 3.32. The dense coating at the top is the protective Pt layer. A significant difference to the sample without additive can not be observed, for comparison see figure 3.3.

The as milled $LiH-MgB_2$ composites with 10 mol% $ZrCl_4$ are shown in more detail in figure 3.33, where 3.33 (b) is the center of image (a) in higher resolution. The faceted homogeneous part in the center of 3.33 (b) is a MgB_2 crystallite of approximately 150 nm width. This was confirmed by EDX and diffraction analysis. The black spot at the upper right hand corner of this crystallite was identified to consist of Iron, probably wear from the milling tools during synthesis.

By EDX analysis, a small region surrounding the MgB_2 crystallite shows high Zr and Cl concentration. This is presented in more detail by a high resolution

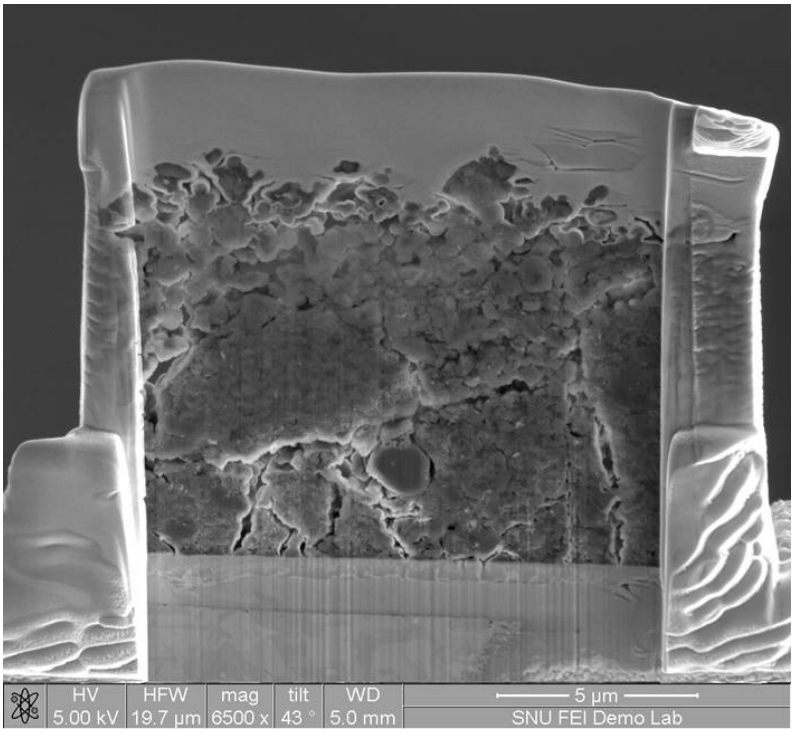

(a) as milled LiH−MgB_2+0.1$ZrCl_4$ composites

Figure 3.32: SEM image of the cross section of as milled LiH−MgB_2 composite with 10 mol% $ZrCl_4$.

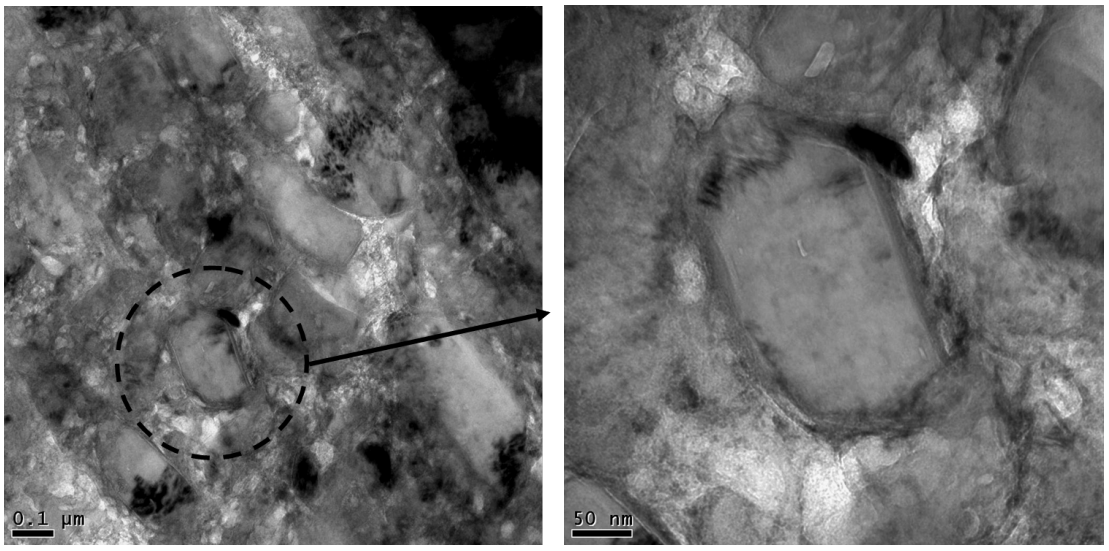

(a) overview (b) detail

Figure 3.33: TEM images of LiH−MgB_2 composite with 10 mol% $ZrCl_4$ with (a) overview and (b) detail.

micrograph in figure 3.34. On the right hand side the lattice planes of the MgB_2 crystallites are visible. The amorphous region on the left hand side consist mainly of Li. But the interface region shows high concentration of Zr. This region of about 2 nm thickness has an amorphous structure as well. This is on the same length scale as the characteristic lengths determined from the ASAXS experiments. From the previous measurements a composition of Zr and B phase and the formation of LiCl is expected. Li as well as Cl is also detected in this region with the high Zr concentration, but only little B. From this observation a formation of an amorphous Zr-Cl-Li containing phase can be concluded.

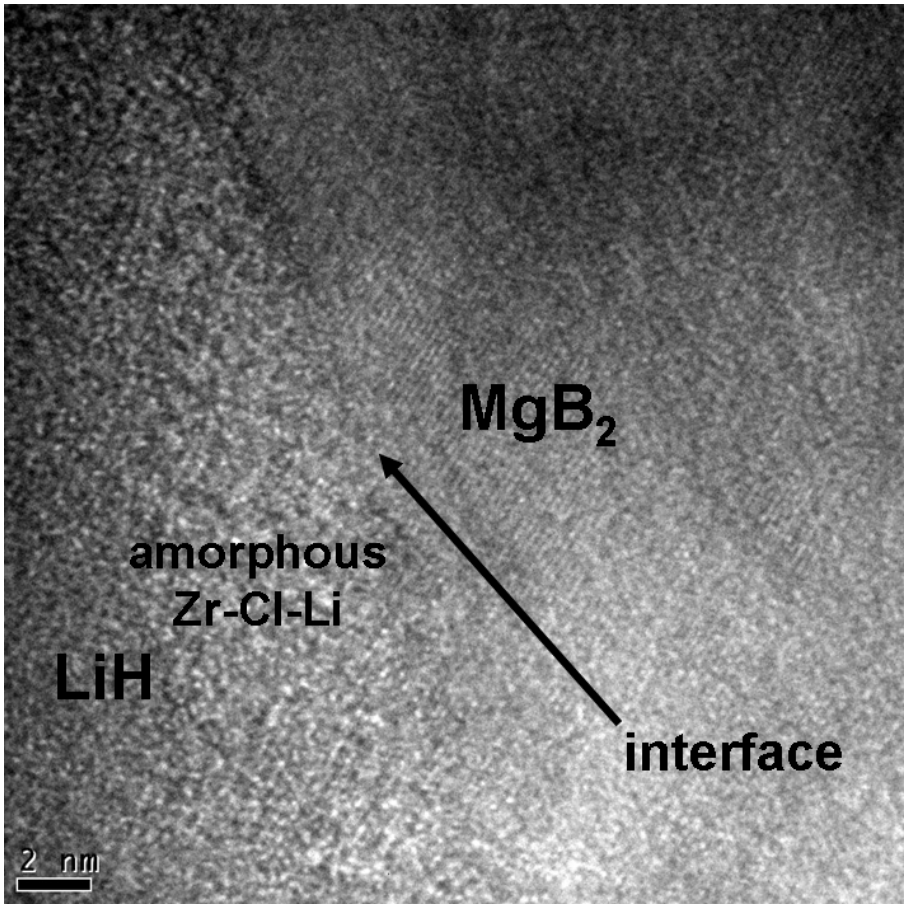

Figure 3.34: High resolution TEM image of LiH−MgB_2 composite with 10 mol% $ZrCl_4$.

However, in another location of this sample, a diffraction pattern of crystalline ZrB_2 was identified, see figure 3.35. But since MgB_2 and ZrB_2 have the same lattice structure and very similar lattice parameters, differentiation between the two phases is difficult from the diffraction patterns.

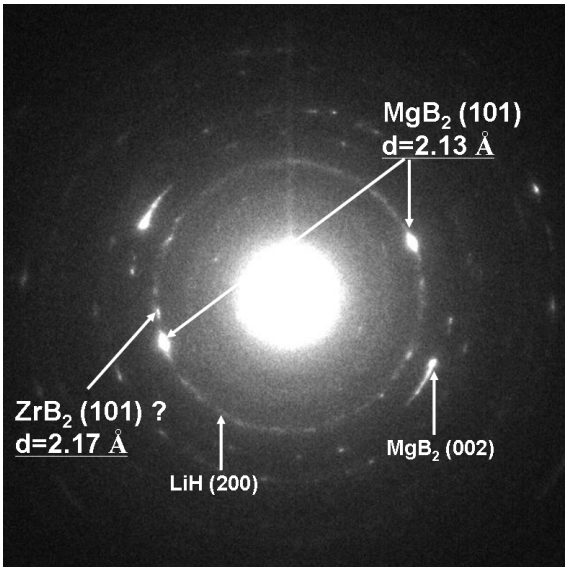

Figure 3.35: TEM diffraction image of crystalline MgB_2, LiH and possibly ZrB_2.

3.4.2 Light metal oxides and hydroxides as additives

The reaction kinetics of the materials were observed to vary in different laboratories. Prepared in conditions with up to about 200 ppm oxygen, the reaction times of the first desorption reaction of $LiBH_4{-}MgH_2$ composites was reduced to 3 hours under otherwise identical conditions [76]. This is in contrast to the approximately 25 hours for the composites prepared in high-purity atmosphere with an oxygen content below 25 ppm. To investigate the origin for this behavior, small amounts of microcrystalline Mg- and Li-oxide and -hydroxide were added to the compounds in a first approach [77]. Their effect is presented in the following section. A future approach will be exposure of the pure composites prepared in high-purity conditions to controlled amount of oxygen and water vapor.

The first desorption of the $LiBH_4{-}MgH_2$ composites with additional 5 mol% MgO (trace with black squares in figure 3.36) shows very similar properties as the pure composite. For additional 5 mol% $Mg(OH)_2$ (trace with open circles in figure 3.36) an approximately 30% longer incubation period is observed. During the second desorption reaction the incubation period is even doubled in time compared to the first desorption reaction (results not shown). Detailed investigation by XRD revealed the formation of stable, microcrystalline MgO during the milling for additional $Mg(OH)_2$. During the second desorption reaction the incubation period is even doubled in time compared to the first desorption reaction (results not shown). Composites with additional Li_2O and LiOH overcome of the incubation

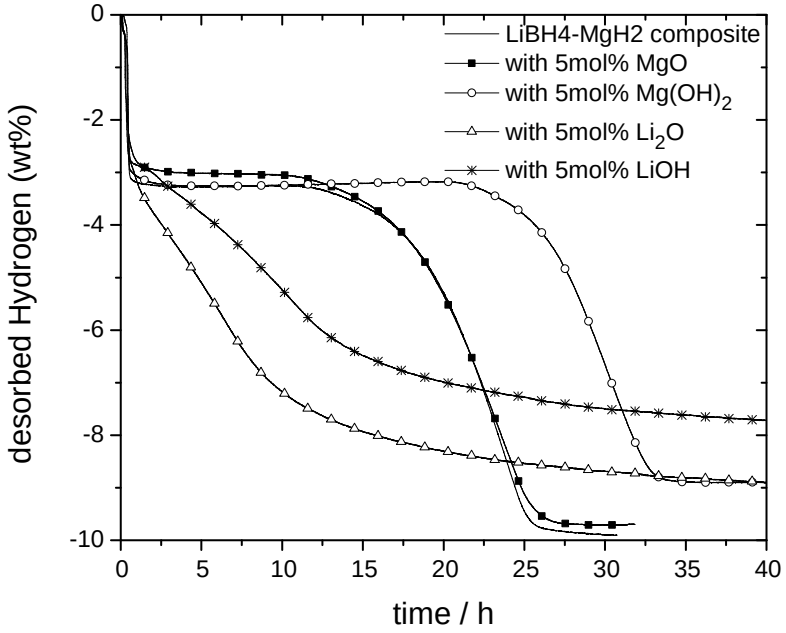

Figure 3.36: Volumetric measurements of the first desorption reactions of initial $LiBH_4-MgH_2$composites with additional light-metal oxides and hydroxides. Measured under 4 bar hydrogen at 390 °C.

period (trace with the open triangles and stars, respectively) but exhibit extremely slow reaction kinetics. Li_2O and LiOH is observed in the XRD-patterns of the milled composites but not anymore in the cycled composites. A reaction of the Li_2O with the hydride matrix is therefore assumed. The extremely slow reaction kinetics indicate the formation of a reaction barrier, possibly due to this newly formed phase.

3.4.3 Possible rate limiting nucleation of MgB_2

One possible origin of the observed incubation period during the first desorption reaction is restricted nucleation of MgB_2. The incubation period could then be overcome by additives supporting heterogeneous nucleation of this compound. In the simplest case, this can be finely distributed MgB_2. Therefore, MgB_2 was added to the initial compounds and investigated by volumetric measurements shown in figure 3.37. Preparation method and quantity of the additive were varied as these are parameters influence the distribution of the additive.

A significant influence can be observed especially when a fairly large quantity (10 mol%) of MgB_2 (line with open circles) is added to the pre-milling of the MgH_2. The line with stars represents the sample where only 3 mol% MgB_2 was added to

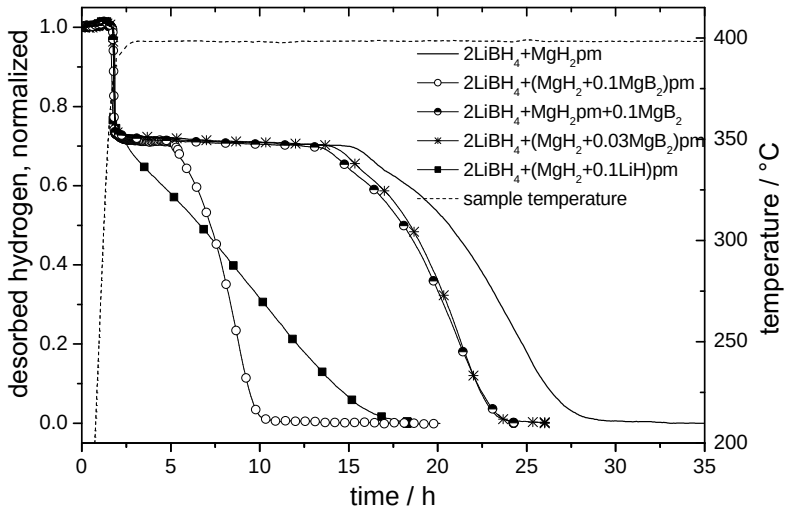

Figure 3.37: Kinetic measurements at 400 °C and 5 bar hydrogen of the first desorption reaction of $LiBH_4-MgH_2$ composites for the investigation of heterogeneous nucleation with addition of final compounds.

the pre-milling of MgH_2 and the line with the open circles represents the sample where the 10 mol% MgB_2 was not pre-milled. The reference sample of the pure composite is represented by the line trace. The lengthy incubation period observed for the latter two samples suggest, that the distribution as well as the amount of the additive is of importance. For these two samples, almost no deviation from the pure sample was observed. For the sample with additional LiH, no incubation period was observed (line with filled squares). The closest packed planes of MgB_2 and LiH show a small lattice misfit, a mandatory condition for heterogeneous nucleation. Thus, Nucleation of MgB_2 on LiH might explain the lack of the incubation period with additional LiH. In general, no correlation between the sorption kinetics and the initial crystallite size, estimated from the XRD scans by application of the Scherrer formula, was found.

The strong effect of surplus final materials, such as LiH and MgB_2, indicate, that the nucleation of MgB_2 could be a rate limiting step during the desorption reaction. For a control test, the aim was to find an additive that shows a very high lattice misfit to MgB_2 and therefore does not support heterogeneous nucleation of MgB_2 or LiH during the desorption reaction. For the measurement CaB_6 was chosen because of its chemical inertness and the large lattice misfit to MgB_2. Furthermore, its three dimensional network structure of boron-octahedra with Ca centers is unlikely to support the layered MgB_2 structure. During preparation it was pre-milled together with the MgH_2 to ensure good distribution. The results for

the kinetic measurements for $LiBH_4-MgH_2$ composites with 10 mol% additional CaB_6 is shown in figure 3.38 in comparison to the pure composite as a reference.

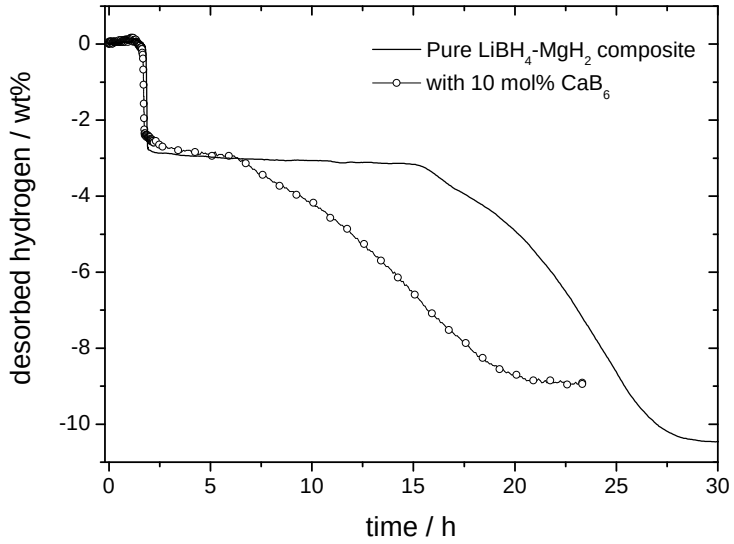

Figure 3.38: First desorption of $LiBH_4-MgH_2$ composites with and without additional CaB_6. Measured under 5 bar hydrogen at 400°C.

The reduced capacity origins from the relatively large amount of additional CaB_6. The incubation period is significantly reduced , though not vanished. The CaB_6 does not react with the hydride matrix; in the XRD patterns the corresponding reflections can be observed before and after the sorption reactions. The reduction of the incubation period is suggested to be caused by a change of the microstructure during the milling process or a prevention of coarsening during the sorption reactions, but this was not yet confirmed. The subject of nucleation and function and mechanism of the additives is further discussed in section 4.2.

It is interesting to note, that the addition of MgB_2 to the initial composite has a positive influence on the first absorption reaction as well, see figure 3.39. This might be due due to a stabilizing effect of the grain boundaries and prevention of coarsening. Finer grain sizes imply shorter diffusion distances during the following sorption reaction and thus lead to shorter reaction times.

3.5 Cycling of the composites

For practical applications, not only the sorption kinetics of the first desorption or absorption reaction are important but also the materials behavior during further sorption reactions is very important. Up to 5 sorption cycles were studies by volu-

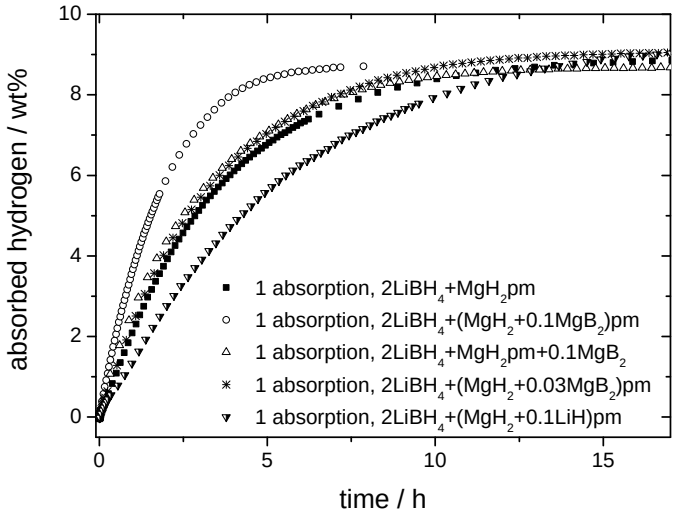

Figure 3.39: Kinetic measurements of the first absorption reaction of $LiBH_4-MgH_2$ composites for the investigation of heterogeneous nucleation during the desorption reaction.

metric measurements and thermal analysis in the HP-DSC was performed for the first two cycles for chosen composites.

As already noted in figure 3.18, the first absorption reaction after a previous desorption shows faster kinetics in comparison to the milled powder. In figure 3.40 the first and second desorption reaction for the pure $LiBH_4-MgH_2$ composites are shown.

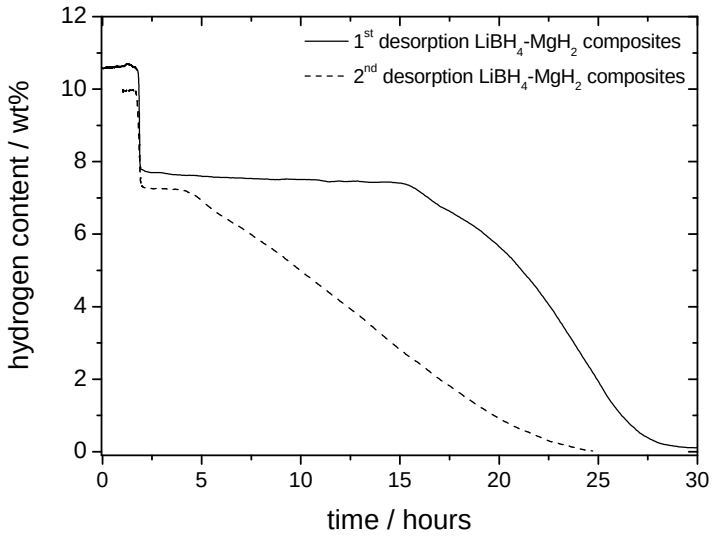

Figure 3.40: First and second desorption reaction of $LiBH_4-MgH_2$ composites, measured at 400 °C and 5 bar hydrogen

The incubation period is almost overcome for the second desorption. But during the second desorption of $LiBH_4$ the reaction rate is lower than for the first desorption reaction. For the second desorption the capacity is slightly reduced to approximately 10 wt%. XRD measurements reveal residual MgB_2. This could play an important role on the suppression of the incubation period. This idea is discussed in more detail in section 3.4.3.

In figure 3.41 the first three cycles of LiH−MgB_2 composites prepared in the desorbed state are shown for the desorption (3.41(a)) as well as the absorption reaction 3.41(b). The absorption reaction of the pure initial LiH−MgB_2 composites remains very similar with the ongoing cycling reactions. For these composites, already the first desorption reaction does not show an incubation period. The gravimetric capacity with approximately 9 wt% is below the theoretical value, possibly due to unreacted MgB_2. This could then overcome the incubation period during the desorption reaction. With further cycling a slight increase of the reaction rate of the second step is noted.

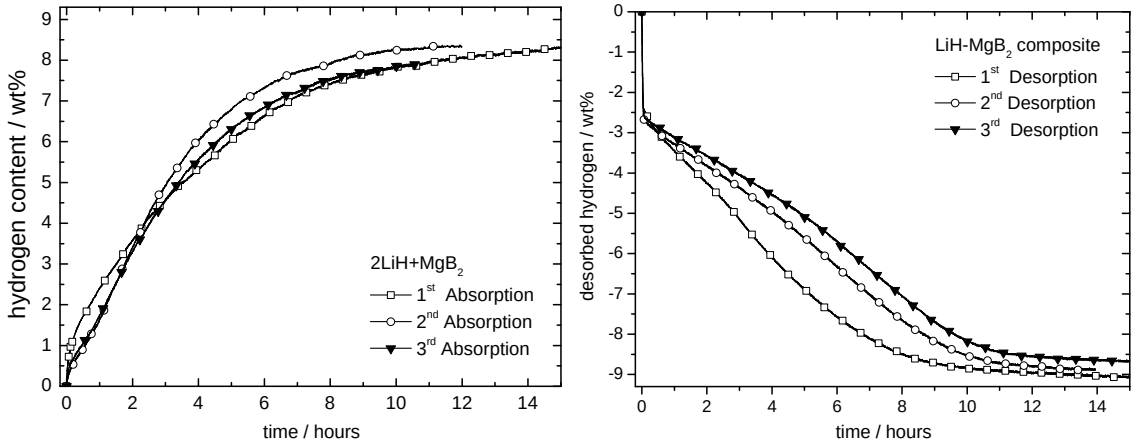

(a) absorption (b) desorption

Figure 3.41: Cycling of pure LiH−MgB_2 composites. Desorption at 400 °C, 5 bar hydrogen and absorption at 350 °C and 50 bar hydrogen [78].

In figure 3.42 the first five sorption cycles for LiH−MgB_2 composites with additional 5 mol% $ScCl_3$ are shown. In comparison to the first absorption reaction of the pure composites, the reaction with additive is much slower. Upon further cycling, the sorption rates of the absorption reactions become much enhanced.

The desorption reaction shows already very fast reaction kinetics for the first desorption in comparison to the pure composite. For the second and further des-

orption reactions the reaction time is further reduced and shows higher reaction rates for the second reaction besides increased capacity.

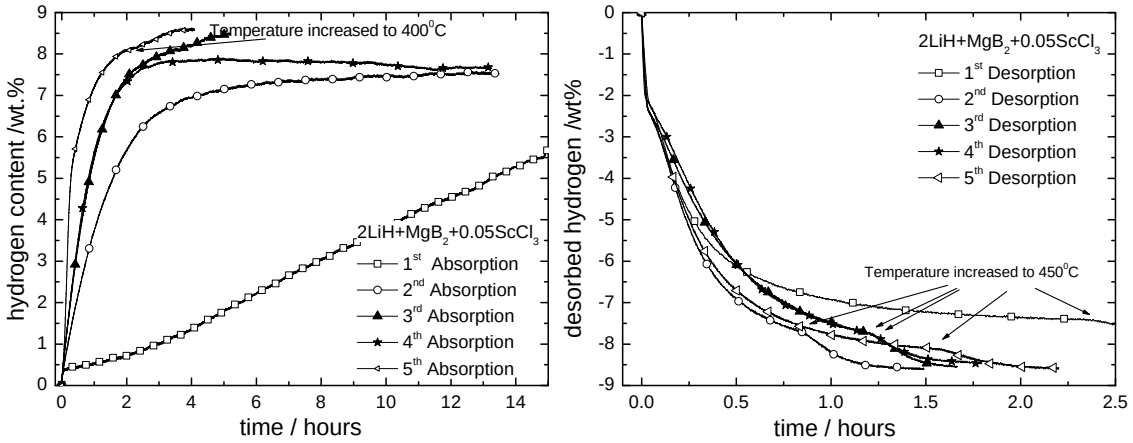

(a) absorption (b) desorption

Figure 3.42: Cycling of LiH−MgB_2 composites with 5 mol% $ScCl_3$. Desorption at 400 °C, 5 bar hydrogen and absorption at 350 °C and 50 bar hydrogen [78].

The cycling of the materials was also investigated by HP-DSC. In figure 3.43 the heating traces of the first and second desorption reaction as well as the first absorption reaction of $LiBH_4$−MgH_2 composites with 5 mol% VCl_3 are shown. In the investigated temperature range up to 475 °C the first desorption reaction (black trace) shows all four endothermic events and the desorption of $LiBH_4$, reaction D, is apparently complete. The following absorption reaction (gray trace) under 50 bar hydrogen displays two exothermic events. Upon cooling as well as during the next heating (dotted trace), the distinct peaks of $LiBH_4$ A and B were observed, proving the reabsorption of hydrogen. The second desorption reaction (dotted trace) shows very similar reactions A, B and C in comparison to the first desorption reaction, but the onset temperature of reaction D is significantly lowered by approximately 15 °C and the reaction spreads over a larger temperature range. This indicates a faster and earlier start of the reaction, maybe due to a lowered activation barrier for the reaction, but also a lower reaction rate. Reaction D is also completed in this experiment.

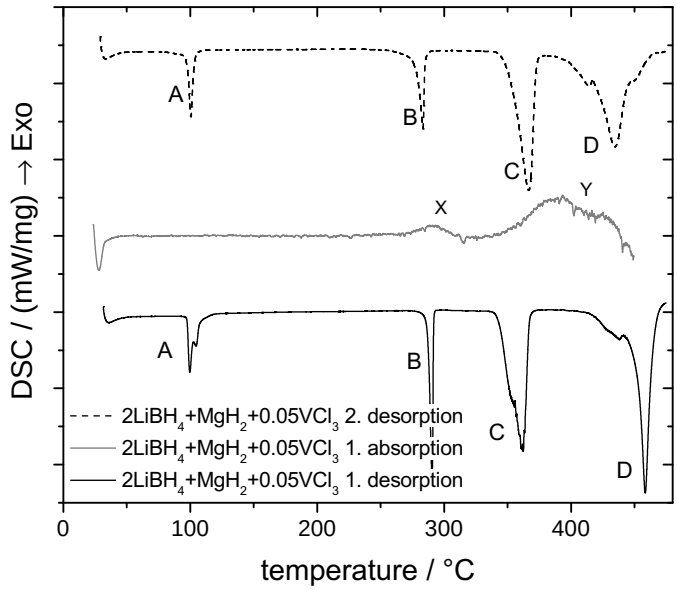

Figure 3.43: HP-DSC measurements of $LiBH_4-MgH_2$ composites with 5 mol% VCl_3 of the first desorption, absorption and second desorption with 5 K/min, desorption under 3 bar hydrogen and absorption under 50 bar hydrogen.

As already noted in section 3.2.2, the exothermic formation of MgB_2 cannot be observed by this method. However, MgB_2 must form at one point, because the reaction is completely reversible and formation of $LiBH_4$ from the elements is not possible under these conditions according to my and other measurements [57, 66, 67].

4 Discussion

In the following section, the experimentally obtained sorption reactions of $LiBH_4$-MgH_2 composites are evaluated with respect to the reaction mechanisms and to the origin of the kinetic limitations. The observed reaction steps are presented in relation to the experimental parameters and their consequences are discussed. Proposed reaction mechanisms and suggested rate limiting steps are compared to other work on the RHC systems and the pure compounds $LiBH_4$ and MgB_2. The emphasis is laid on the sorption reactions of $LiBH_4$ and the formation of MgB_2 rather than the sorption reactions of MgH_2.

As a second point, the origin of the incubation period and function and mechanism of additives is discussed in detail. Transition-metal and light-metal based additives have a strong influence on the reaction kinetics of the composites. More detailed investigations on the chemical state, size and distribution were exemplarily performed for Zr-based additives. How these various compounds with very different chemical properties have a similar impact on the composites is discussed.

The last part focuses on the limitations in the reaction kinetics of the ongoing sorption reactions. The results are evaluated by comparison of the obtained kinetic curves to calculated functions of the reacted fraction with known rate limiting processes. Conclusions on the rate limiting processes during the sorption reactions in the composites are drawn.

4.1 Reaction mechanism in $LiBH_4-MgH_2$ composites

As described in section 3.2.3 two different reaction pathways were observed for the desorption reaction of $LiBH_4-MgH_2$ composites. For experimental temperatures of 400 °C and 5 bar hydrogen, i.e. below the equilibrium temperature of $LiBH_4$ at this pressure, the formation of MgB_2 is suggested to take place simultaneously to the desorption of $LiBH_4$. In in-situ XRD measurements the formation of MgB_2 and a significant rise in pressure was measured simultaneously (see figure 3.15). The

experimental conditions are similar to those in the isothermal volumetric measurements and they are illustrated as point A in the van't Hoff plot of the composites and the individual compounds in figure 4.1.

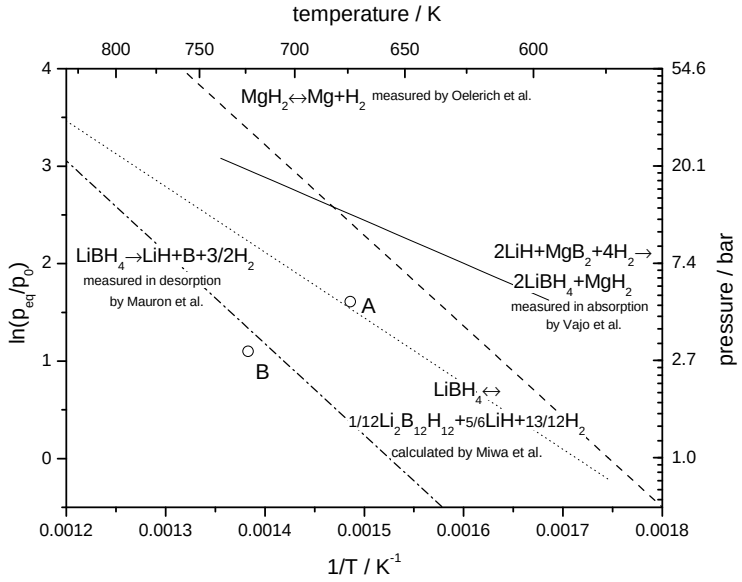

Figure 4.1: Van't Hoff plot of the LiH−MgB_2 composite [14] as well as the pure compounds $LiBH_4$ decomposing directly into LiH, B and H_2 [57] or into $Li_2B_{12}H_{12}$, LiH and H_2 [60, 79] and MgH_2 [64] (mean value of ab- and desorption).

The desorption reaction is then suggested to proceed in two steps along the following pathway:

$$2\,LiBH_4 + MgH_2 \longrightarrow 2\,LiBH_4 + Mg + H_2 \longrightarrow 2\,LiH + MgB_2 + 4\,H_2 \qquad (4.1)$$

Here, the reaction enthalpy is effectively lowered, because release of hydrogen from $LiBH_4$ takes place below its thermodynamic equilibrium temperature for the applied pressure. The applied hydrogen back-pressure suppresses the decomposition of $LiBH_4$ into LiH, B and H_2 as well as into $Li_2B_{12}H_{12}$, LiH and H_2 and thus facilitates the formation of MgB_2. The intermediate formation of metallic Mg was also observed for other MgB_2 forming RHCs [15, 80]. The onset temperature of the desorption of MgH_2 in the volumetric measurements (see figure 3.9) matches approximately the equilibrium temperature of MgH_2 for the applied pressure.

With large heating rates and high final temperatures, the conditions applied for example in DSC measurements, conditions below the equilibrium pressure of pure

$LiBH_4$ are realized, illustrated as point B in figure 4.1. Then individual desorption of the two hydrides MgH_2 and $LiBH_4$ is observed in in-situ XRD experiments with pressure recording (see figure 3.16). The formation of MgB_2 is shifted to higher temperatures.

Under such high temperature and low pressure conditions, the partial decomposition of $LiBH_4$ into amorphous $Li_2B_{12}H_{12}$ is suggested, because it was proposed and experimentally verified for the decomposition of the pure compound [60–62]. The formation of $Li_2B_{12}H_{12}$ was calculated to lower the reaction enthalpy for the desorption of pure $LiBH_4$ by approximately 20 kJ/mol H_2 [60,79], illustrated by the dotted line in figure 4.1. Brampton et al. have measured the formation of amorphous $Li_2B_{12}H_{12}$ in cycled $LiBH_4$–MgH_2 composites by Raman spectroscopy [81]. Their desorption measurements were performed under a low argon pressure and neither the formation of MgB_2 nor the reabsorption to $LiBH_4$ was observed.

Presence of $Li_2B_{12}H_{12}$ in cycled $LiBH_4$–MgH_2 composites was also found by solid state NMR spectroscopy by Bowman et al. [82]. They investigated the samples prepared at HRL laboratories [14] by heating to 350 to 400 °C in closed volumes and therefore final pressure of several bar hydrogen. Purewal et al. [83] have confirmed the formation of $Li_2B_{12}H_{12}$ for the $LiBH_4$–ScH_2 system, but since no ScB_2 was formed in the desorbed state, the thermodynamics and reaction mechanism of the $LiBH_4$ is expected to remain unchanged. It is likely that the intermediate formation of the $[B_{12}H_{12}]^{2-}$ anion hampers the formation of MgB_2 despite a high thermodynamic driving force. The inactivity of the $[B_{12}H_{12}]^{2-}$ anion is due to the symmetric icosahedral structure with small contact surfaces. The structure is illustrated in figure 4.2.

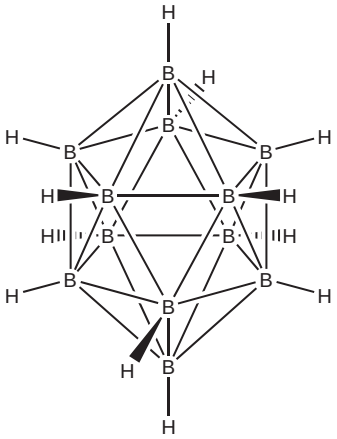

Figure 4.2: Structure of the $[B_{12}H_{12}]^{2-}$ anion

Regarding the reaction kinetics, a subsequent formation of pure boron is likely, because the icosahedral structure of pure α-Boron is very similar to the structure of the $[B_{12}H_{12}]^{2-}$ anion [84]. The formation of MgB_2 would then proceed from the elements and would thus have to cope with the same kinetic limitations as they are observed for the synthesis of the superconductor materials. Synthesis of MgB_2 for superconductor applications usually takes place through the liquid or gas phase of Mg [85,86], at temperatures above 600 °C with a lowest observed onset temperature of the reaction of 440 °C for nanocrystalline starting materials [87].

The desorption reaction in the composites under low hydrogen pressures and elevated temperatures is therefore likely to proceed partially along the following pathway:

$$\begin{aligned} 2\,LiBH_4 + MgH_2 &\longrightarrow 2\,LiBH_4 + Mg + H_2 \longrightarrow \tfrac{5}{3}\,LiH + \tfrac{1}{6}\,Li_2B_{12}H_{12} + Mg + \tfrac{19}{6}\,H_2 \\ &\longrightarrow 2\,LiH + 2\,B + Mg + 4\,H_2 \longrightarrow 2\,LiH + MgB_2 + 4\,H_2 \end{aligned} \tag{4.2}$$

In contrast to this reaction mechanism, Yu et al. [88] observed the formation of a Li-Mg alloy beside the formation of MgB_2 during the desorption reaction after heating their samples up to 600 °C, but this was not reproduced by other groups. LiH is know to decompose only above its melting point of 689 °C, the observation of a Li-Mg alloy below this temperature is therefore surprising. Early publications by Schlesinger et al. [89] and early investigations of Züttel et al. [58,59,69] propose the decomposition via the intermediate formation of $LiBH_2$, but the formation of this phase was not confirmed experimentally.

The unidentified diffraction maxima, that are observed during the in-situ XRD measurements, see sections 3.2.3 and 3.3.3, could be due to an intermediate phase. But they appear at various positions for the different measurements and can not be matched to any of the proposed intermediate compounds from [55, 58–60, 90, 91].

The performed experiments reveal a strong dependency of the desorption reaction on the experimental parameters. Below the equilibrium temperature of $LiBH_4$, the formation of MgB_2 is suggested to take place directly without any formation of $Li_2B_{12}H_{12}$. This assumption was not yet verified, but first Raman measurements of isothermally desorbed samples at 400 °C and 5 bar hydrogen give no indication for the presence of a $Li_2B_{12}H_{12}$ phase.

Formation of MgB_2 upon desorption was observed to be the key issue for reversibility. Rehydrogenation to $LiBH_4$ under moderate temperatures and hydrogen

pressure is only possible if the desorption products were LiH and MgB_2. From the desorption products LiH and Mg obtained in vacuum, only rehydrogenation of Mg to MgH_2 is possible [54] under moderate conditions such as 100 bar hydrogen at 350 °C. The formation of hexaborides like CaB_6 or CeB_6 upon desorption in other RHC systems shows improved reaction kinetics but the kinetics of the rehydrogenation reaction are minor in comparison to the reabsorption of from the diboride [92]. This is probably related to the layered hexagonal crystal structures of the diborides in comparison to three-dimensional network forming boron-structures of the hexaborides. The network structure is favorable during the desorption but is detrimental during the absorption reaction because of its lower reactivity. This observation supports the key-role of the chemical and structural state and of the boron for the absorption reaction. Pure amorphous B as well as boron integrated in network structures like in polyhedral B and in borane phases is kinetically inactive and its formation needs to be avoided. Relatively weakly bound B as in MgB_2 or LiB_3 is observed to enhance the absorption reactions [12, 67].

The onset temperature of the absorption reaction of $LiH-MgB_2$ composites under 50 bar hydrogen is observed in the HP-DSC for temperatures as low as at 250°C, see figure 3.19.

4.2 Function and influence of the additives

In section 3.4 the substantial influence of additives was reported. The effect is not only observed for transition metal based additives or "typical" additives for complex hydrides such as $TiCl_3$ but also for transition-metal- and light-metal-oxides and surplus material of final products like MgB_2 and LiH. The additives do not only influence the first sorption reactions but enhance and stabilize the improved reaction kinetics upon further cycling. To identify the mechanism by which the additives improve the reaction kinetics, the chemical states and sizes were investigated exemplarily for Zr-based additives by means of XANES and ASAXS (section 3.4.1.1). The results show a formation of stable ZrB_2 during milling or the heating of the first sorption reaction. The average size of these Zr-containing phase was determined to be in the range of several nm, only. The formation of borides is considered to be representative for the transition metal chlorides and isopropoxides as additives, because the transition metal borides are thermodynamically very stable. The origin of the incubation period and the delayed onset of the desorption reaction of $LiBH_4$ is therefore proposed to be related to the nucleation of MgB_2.

In the following, the ability of transition-metal borides to support heterogeneous nucleation of MgB_2 and their role as a grain refiner during the sorption reactions are discussed.

In a first approach, the critical radii of nucleation are estimated to be very small due to the high driving force of the overall reaction. However, there are two new crystalline phases that have to be formed during the desorption reaction, namely LiH and MgB_2. Therefore the overall reaction enthalpy as a driving force is split up for the formation of the two phases. A formation of two new phases leads also to the formation of two new interfaces which has to be considered in the interfacial contribution. Furthermore, the compounds in the composites exist only in stoichiometric concentrations, high ordering energies are thus implied. Considering the presently available data, a good estimation of the driving force and critical radius for nucleation for the individual compounds is not possible.

A necessary condition for heterogeneous nucleation is a low interfacial energy. The interfacial energy is dominated by the strain caused by the lattice misfits at the interface. Therefore a low interfacial energy is primarily achieved by a small lattice misfit of the closest packed planes of the two phases. Chemical contributions play a secondary role. For the present material couples, there is no data available for the interface energies. However, the lattice misfit can be estimated from the crystal structures of the phases. The lattice misfit of the metal atoms in the closest packed plane of various additives and participating compounds are noted in table 4.1 [93]. A good distribution and a sufficient amount of the nucleation agents are mandatory for efficient heterogeneous nucleation.

Several observations support the crucial role of nucleation of MgB_2. The observed incubation period for the pure composites is striking and must be related to a time-independent process. This excludes, e.g., diffusion or hydrogen recombination and hints towards complicated nucleation of the newly forming phases.

The XANES measurements reveal the formation of ZrB_2 upon milling or cycling of the composites (see section 3.4.1.1). MgB_2 and ZrB_2 have the same hexagonal lattice structure and very similar lattice parameters, therefore a support of MgB_2 nuclei on ZrB_2 is given, see table 4.1. The reaction of the Zr-based additives with the composite material to form the boride leads to a very fine distribution. The phase itself can not be detected by XRD. Additionally, ASAXS measurements and TEM images of samples with Zr-based additives show a nanometer scaled formation of a Zr-phase surrounding MgB_2 (see section 3.4.1.2 and 3.4.1.3).

TiB_2 precipitations in Ti doped MgB_2 were observed by TEM in the grain boundaries as well as in the matrix [94, 95]. In analogy, a location in the grain bound-

Compound	Plane	Misfit in %
Mg	{0001}	3.7
LiH	{111}	6.5
MgO	{111}	3.5
$Mg(OH)_2$	{001}	2.2
Li_2O	{100}	15.5
LiOH	{100}	16.8
TiB_2	{0001}	1.8
VB_2	{0001}	2.9
ZrB_2	{0001}	2.7
CaB_6	{100}	62.5

Table 4.1: Calculated lattice misfits between the {0001}basal-plane of MgB_2 and the closest packed planes of the named compound.

aries of the newly formed ZrB_2 nanoparticles in the composites is likely because the sorption reactions involve complex phase transformations with significant mass transport, which could sweep the precipitates into the grain boundaries. This is supported by XPS and TEM results obtained for as milled $LiH-MgB_2$ composites. XPS measurements on cycled composites with additional Ti-iso revealed no Ti at the surface of the particles [96]. In the grain boundaries, they could function as grain refiners and support the heterogeneous nucleation. A similar crystallite size was deduced from the XRD patters after each sorption reaction, but the role of the additives as a grain refiner needs to be further confirmed.

The addition of surplus MgB_2 to $LiBH_4-MgH_2$ composites leads to a similar sorption behavior as with additional transition-metal based additives. This indicates a similar mechanism. Since MgB_2 is one of the reaction products, the effect is expected to be physical rather than chemical. The experiments have also shown, that a certain amount of surplus MgB_2 is necessary and that a good distribution is crucial for the enhancement of the reaction (see figure 3.37).

A catalytic effect on the hydrogen interaction of a transition-metal boride is unlikely. The charge free surfaces of the mainly covalently bonded material leads only to small interaction with hydrogen gas [97, 98].

The proposition is further supported by a detailed in-situ neutron diffraction study on pure and $TiCl_3$ catalyzed $NaAlH_4$ by Singh et al. [99]. They found the

grain size to be stable during the sorption reactions for the samples with additive, while the pure samples showed significant coarsening. They propose a positive effect of NaCl on heterogeneous nucleation of NaH because of large agreement of the crystal lattices. Thus, an important role of the additive as a grain refiner in $NaAlH_4$ is concluded.

As a rule of thumb, lattice misfits below 5% are expected to support heterogeneous nucleation of the newly forming phase, but in specific cases more stringent requirements have to be met. Regarding the calculated lattice misfits in table 4.1, metallic Mg would be expected to support heterogeneous nucleation of MgB_2 and therefore no incubation period should be observed at all. However, a lattice misfit greater than 2% cannot be overcome by elastic deformation in ceramic-like materials like MgB_2. Thus, dislocations would have to be included during the growth. This would lead to a significant increase of the interfacial energy, because the square of the dislocation density contributes to the interfacial energy.

Typically the nucleation occurs at ledge positions. Therefore, not only the misfit to the basic plane is important, but also the third dimension of the growing phase needs to match the ledge. The misfit of the c-axis of Mg and MgB_2 is large, therefore high energy releasing this misfit in dislocations would be necessary. Furthermore, metals with a relatively low energy of fusion are known to be poor substrates for nucleation [100].

Similar, a large misfit in the third dimension was observed for MgO and MgB_2. For the transition metal borides, the third-dimension misfit can be neglected, because the borides were observed to be present as nanoscaled structures.

A further indication, why borides facilitate the formation of MgB_2 in contrast to metallic Mg might be the valence state. The bonding of Mg to the boron layers in MgB_2 is ionic, therefore the interaction between metallic Mg and boron is likely to be weak. For the formation of MgB_2 the metallic Mg needs to be ionized.

It should also be pointed out, that by proposing the nucleation of MgB_2 being a rate limiting step, the high kinetic stability of $LiBH_4$ may be neglected. $LiBH_4$ has a determined equilibrium temperature of 370 °C at one bar hydrogen which means a decomposition approximately 100 °C above the melting point [57]. The origin for the high stability was related to charge transfer from the cations of the BH_4^- tetrahedron [101]. Theoretical calculations relate the stability of the $LiBH_4$ compound to the perfect symmetry [102] of the BH_4^- tetrahedron [103–106]. This ideal configuration was experimentally confirmed by the diffraction studies of Hartman et al. [107] and Renaudin et al. [108]. Du et al. [104] investigated the role of the charge distribution, e.g., lithium vacancies in the (010) surface during the

dehydrogenation of $LiBH_4$ by ab initio density functional calculations. For such vacancies they found a significant weakening of the B−H bonds in the surrounding BH_4^- complex and reduction the activation energy for hydrogen recombination by more than one half. Their studies show an increase of distortion of the tetrahedron with a decrease of charge. $LiBH_4$ is liquid at the desorption temperature, thus many Li vacancies are expected to be present. Still, the study indicates, that destabilization can be achieved by a change in the local charge distribution. And indeed, by substituting/mixing $LiBH_4$ with Mg the onset temperatures for the dehydriding reactions is lowered [66].

Considering these studies, the positive effect of the transition-metal based additives could also be caused by an influence on the local charge distribution in $LiBH_4$. The observed transition-metal borides are unlikely to change the charge distribution but the reaction of the additives with the hydride matrix changes the stoichiometry of the system and thus may lead to changes in the charge distribution. However, this hypothesis does neither explain the origin of the incubation period nor the change in the reaction kinetics with additional MgB_2 or LiH.

Barkhordarian [109] suggested the formation of a thin barrier of $Li_2B_{12}H_{12}$ at the interfaces between Mg and $LiBH_4$ from defect sites. The chemical inertness of the $[B_{12}H_{12}]^{2-}$ anions could prevent the interaction of B with Mg and thus further delay the nucleation of MgB_2. However, this proposition needs to be experimentally verified.

Regarding the obtained results in general, a fundamental role of the additives as grain refiners and support for heterogeneous nucleation is likely.

4.3 Rate limiting processes during the sorption reactions

For the progress of the sorption reactions not only the limiting process at the onset of the reaction is important but also the rate limiting processes during the reactions. This is addressed the following section by comparison of the reacted fractions to calculated curves with known rate limiting processes. Qualitative conclusions on the dominating reaction mechanism are drawn. Pure composites and Zr doped composites are in the focus of the present analysis.

In figure 4.3 the volumetric measurements of the first sorption reactions of pure composites are shown again. From these measurements the transformed fraction $\alpha(t)$ is obtained by normalization.

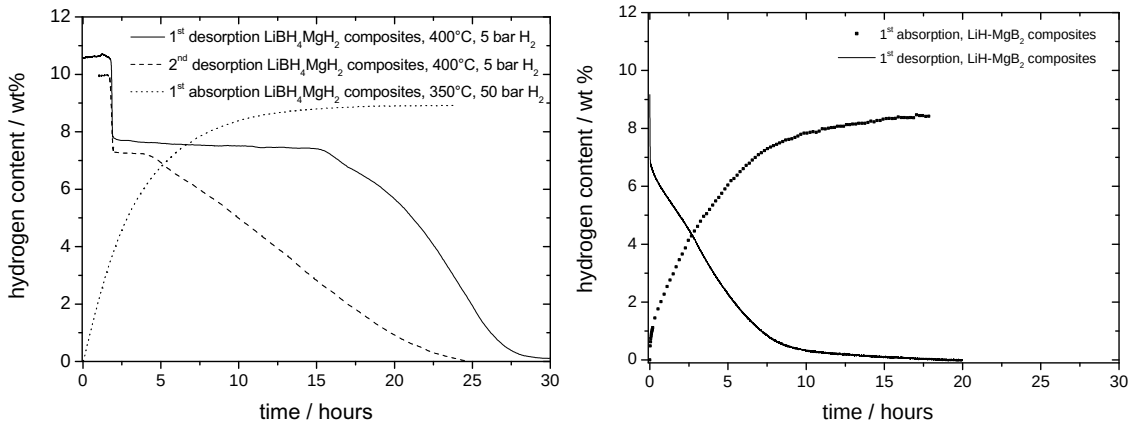

(a) $LiBH_4-MgH_2$ composites (b) LiH-MgB_2 composites

Figure 4.3: Sorption kinetics of pure $LiH-MgB_2$- [78] and $LiBH_4-MgH_2$ composites .

The applied models can be divided in three main groups [110]. An overview over the applied equations and a short description is given in table 4.2. In a first model, the transformed fraction $\alpha(t)$ is directly proportional to time. This is the case for a constant reaction rate, which can be found, e.g., for the chemisorption of hydrogen or a non-adherent product film.

The second group describes the growth of existing nuclei by the Johnson-Mehl-Avrami (JMA) correlation. Nucleation occurs randomly in the bulk of the material. The growth can be controlled by an interface reaction, leading to a constant interface velocity or by a diffusion controlled growth mechanism with a decelerating interface velocity. This group is relatively independent of size and distribution of the reacting particles.

The third group describes the growth of a new phase from the surface to the center of a volume, they are called contracting volume models. Here, an existing thin layer of reacted material on the surface grows inwards. The reaction itself can be again interface or diffusion controlled.

The transformed fraction $\alpha(t)$ in correlation to time is calculated by normalization from the measurements. This calculated transformed fraction is then substituted in the equations. The equations are formed in such a way, that if the assumed process limits the reaction, a linear behavior with time should be observed. The quality of the match is judged by the agreement to a linear fit, the correlation coefficient R must be close to 1 and the passing of the linear fit through zero.

These equations were originally derived to describe the reaction kinetics of solid state reactions of single particles but have been successfully adapted to powder par-

Model equation	Rate limiting process	Label
$\alpha(t) = k \cdot t$	linear correlation to time, surface controlled	alpha
$[-\ln(1-\alpha(t))]^{1/2} = k \cdot t$	two dimensional growth of random nuclei with constant interface velocity	JMA-2D
$[-\ln(1-\alpha(t))]^{1/3} = k \cdot t$	three dimensional growth of random nuclei with constant interface velocity	JMA-3D
$[-\ln(1-\alpha(t))]^{2/3} = k \cdot t$	three dimensional growth of random nuclei with decreasing interface velocity, diffusion controlled	JMA-3D-DiffControl
$1-(1-\alpha(t))^{1/2} = k \cdot t$	two dimensional growth of a contracting volume with constant interface velocity	CV-2D
$1-(1-\alpha(t))^{1/3} = k \cdot t$	three dimensional growth of a contracting volume with constant interface velocity	CV-3D
$1-(1-\alpha(t))^{2/3} = k \cdot t$	three dimensional growth of a contracting volume with decreasing interface velocity, diffusion controlled, no significant change in volume	CV-3D-diffControl
$(\epsilon - [1+(\epsilon-1)\alpha(t)]^{2/3} - (\epsilon-1)[1-\alpha(t)]^{2/3}) / (1-\epsilon) = k \cdot t$	three dimensional growth of a contracting volume with decreasing interface velocity, diffusion controlled, with the product-to-reactant-volume ϵ	CV-3D-diffControl [volume corrected]

Table 4.2: Kinetic model equations and descriptions [111, 112].

ticles and metal hydrides [110–115]. Mintz et al. [111,113] investigated the influence of particle size distribution, particle shape distributions and time distributions for hydriding kinetics of powders for the contracting volume models. They varied these parameters in calculations and determined the boundaries, within which these models can be applied on real powder materials. Only for transformed fractions up to about $\alpha \approx 0.5 - 0.6$ they found the deviations to be small. Thus, the obtained curves are only evaluated to this value in the following analysis.

Condition for all growth models is the presence of nuclei or constant nucleation rate. For the contracting volume models, this means a reacted layer on the contracting volume. This layer must be thin compared to the overall reacting volume. The volume change between the desorbed and the hydrided state cannot be neglected, since the hydrides take up approximately twice the volume of the desorbed state. Therefore the more complex contracting volume model with decelerating interface velocity has to be used. Meaningful analysis of the data is only possible, if the time spread for the initiation of the reaction on each of the particles composing the powder is small.

It is emphasized, that the reactive hydride composites are not simple binary solid-gas systems but complex reactions with four phases in equilibrium and significant mass transport other than hydrogen takes place. Therefore the validity of these models cannot be assumed a priori. However, a well matching model indicates, that a similar processes might limit the reaction.

During the volumetric measurements, a pressure change is measured. Therefore the kinetic curves describe the ab- or desorption of the composite. In case of the absorption reaction the formation of MgH_2 and $LiBH_4$ is related to the decomposition of MgB_2 and LiH. This means, that the reaction kinetics can also be dominated by the decomposition reactions or the formation of a new compound. During the desorption reaction the decomposition of $LiBH_4$ is not necessarily directly connected to the formation of MgB_2. Because of the two step character of the desorption reaction, only the second step associated to the desorption of $LiBH_4$ is considered. Furthermore, the first sorption reactions of the composites are neglected and only cycled samples evaluated.

In figure 4.4 (a) the $F(\alpha)$ are calculated for the first absorption reaction of $LiBH_4$-MgH_2 composites using the models and equations described above. In figure 4.4 (b) the $F(\alpha)$ are calculated for the first absorption reaction of LiH$-MgB_2$ composites. For both composites a contracting volume model shows the most linear behavior with time. In case of the initial $LiBH_4-MgH_2$ composites the reaction appears to be dominated by an interface reaction whereas the reaction in initial LiH$-MgB_2$ composites seems to be dominated by the transport process.

In figure 4.5 the calculated $F(\alpha)$ of a desorption reaction after a previous absorption reaction are shown. For initial $LiBH_4$-MgH_2 composites in figure 4.5(a) and for initial LiH$-MgB_2$ composites in figure4.5 (b).

Independent of the initial preparation steps desorption reactions of the pure composites proceed linear with time. This indicates a constant reaction rate.

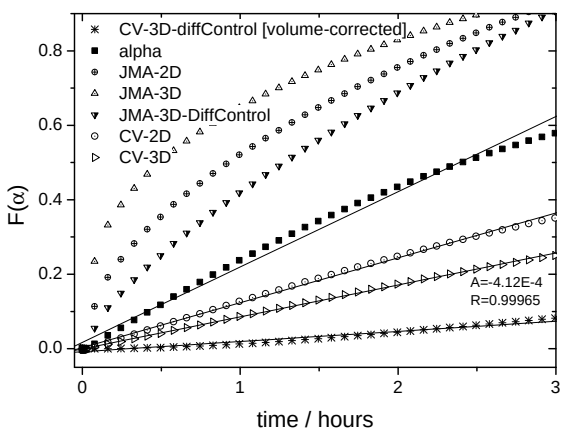

(a) 1 Absorption $LiBH_4-MgH_2$ composites

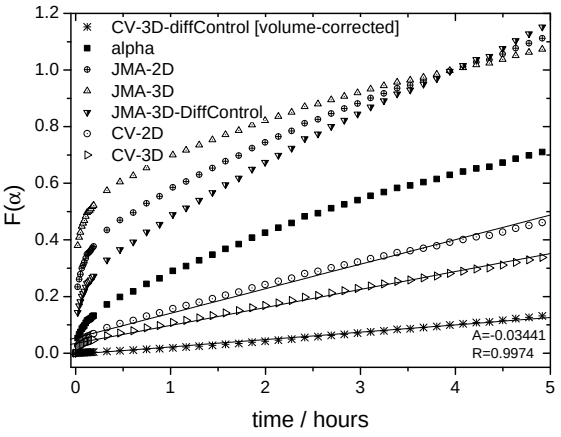

(b) 1. Absorption $LiH-MgB_2$ composites

Figure 4.4: Calculated $F(\alpha)$ using equations of table 4.2 of the first absorption reaction of $LiBH_4-MgH_2$ composites (a) and $LiH-MgB_2$ composites (b).

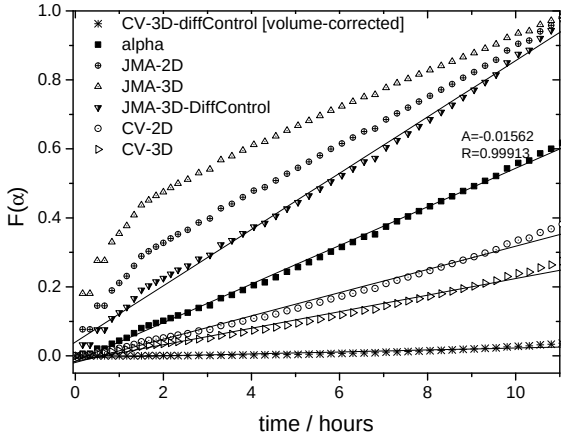

(a) 2 Desorption $LiBH_4-MgH_2$ composites

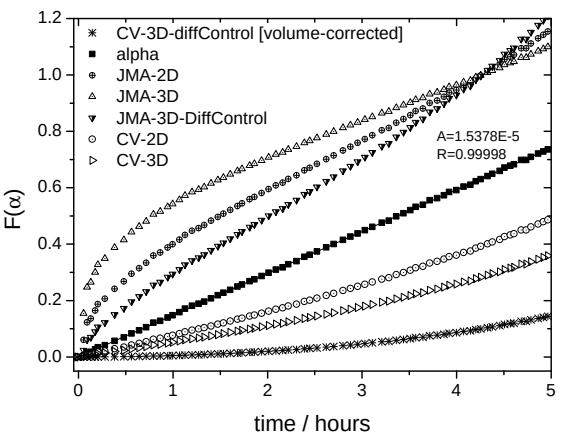

(b) 1 Desorption $LiH-MgB_2$ composites

Figure 4.5: Calculated reacted fraction using equations of table 4.2 of the second step of the second desorption reaction of $LiBH_4-MgH_2$ composites (a) and the first desorption reaction of $LiH-MgB_2$ composites (b).

The obtained correlations seem to be representative for all investigated sorption reactions. In table 4.3 the most correlating model is named for all investigated composites and reactions.

The results indicate, that a similar reaction process dominate the sorption reactions for all composites, independent of the additive and the initial preparation state, although the reaction times are much different. Most of the analyzed desorption reactions correlate well with a linear progress of the reaction. For all absorption reactions, a good agreement with a contracting volume model was observed.

initial composite	Desorption	Absorption
$LiBH_4$−MgH_2	alpha	CV 3D, CV 3D diffusion control
LiH−MgB_2	alpha	CV 3D diffusion control
$LiBH_4$−MgH_2-Zr-iso	alpha	CV 3D diffusion control
LiH−MgB_2-Zr-iso	alpha	CV 3D diffusion control
$LiBH_4$−MgH_2−$ZrCl_4$	CV 3D diffusion control	CV 3D
LiH−MgB_2−$ZrCl_4$	alpha, CV 3D diffusion control	CV 3D diffusion control
$LiBH_4$−MgH_2−MgB_2	alpha, CV 2D, CV 3D	CV 3D
$LiBH_4$−MgH_2−LiH	alpha	CV 2D

Table 4.3: Models best describing the reaction kinetics in reactive hydride composites with Zr additives

For simple binary hydrides, a linear correlation of the transformed fraction during the desorption could mean that recombination of hydrogen molecules at the constant surface is the rate limiting process. However, in the reactive hydride composites the presence of constant surface areas is unlikely, because the reactions are accompanied by significant volume change and the formation of additional phases. Furthermore, the particle size of undoped material was observed to increase by a factor of four during the first desorption reaction.

Another possible explanation for the observed constant rate relationship could be chipping off of the newly formed MgB_2. The ratio of the molar volumes of MgB_2 to Mg is 1.26. This discrepancy leads to strains, which can be released by breaking off of the newly formed phase. In this case the growth of the phase no longer limits the process but the nucleation of the new phase. A linear nucleation rate then leads to a linear relation between the transformed fraction and time. As it was discussed in section 4.2 the additives are assumed to positively influence the nucleation process, which leads to significantly lowered reaction times. This process could be regarded as an analogy to the breakaway oxidation of metals, i.e. iron, where a linear correlation to time is observed.

For absorption reactions a contracting volume model showed the most linear behavior with time in all analyzed cases. For some reaction the process appears to be interface controlled, in others a decreasing interface velocity due to transport processes can be deduced, see figure 4.4. However, it is well possible that these processes are overlapping, in the early stage the interface reaction limits the progress and in later stages diffusion becomes the limiting process because of the increasing diffusion paths. This is in good agreement with the work by Wan et al., who describe the absorption reaction by a diffusion controlled contracting volume model [68].

During the absorption reactions MgB_2 and LiH need to decompose and form $LiBH_4$ and MgH_2, transport processes including B or Mg and Li have to take place besides hydrogen diffusion. The mobile species was not yet identified for the reactive hydride composites, but in pure MgB_2 in the superconductor science, Mg was identified as the mobile species [116–118]. It is therefore likely, that the MgB_2 crystallites are the contracting volume and Li, Mg and hydrogen the mobile species. Hydrogen and Ion diffusion in LiH and $LiBH_4$ is fast in comparison and should not limit the reaction progress [119–121]. From the knowledge of previous work with pure nanocrystalline Mg [112], it is not likely, that the formation of MgH_2 is the rate limiting process of the reaction kinetics.

The reactivity and mobility of the present boron and boron compounds is thus regarded as a key issue for the sorption kinetics.

5 Summary and outlook

In the present work, synthesis and characterization of novel Reactive Hydride Composites was performed. Thermodynamic, kinetic and structural investigations of the ongoing sorption reactions and the materials themselves were performed on $LiBH_4$−MgH_2 composites. Because of the exothermic formation of MgB_2 in the desorbed state, these composites show a reduced overall reaction enthalpy in comparison to the pure hydrides while the storage capacity remains high at 11.4 wt%. Therefore these materials offer promising properties as hydrogen storage materials for mobile applications. However, strong kinetic limitations were observed in the reactions so far.

The experiments revealed a strong dependency of the reaction mechanism on the experimental parameters. By volumetric measurements and in-situ XRD measurements a two step reaction with intermediate formation of metallic Mg was identified for the desorption reaction. Two possible routes were observed for the further desorption of $LiBH_4$ by in-situ XRD with an integrated pressure transducer. Simultaneous desorption of $LiBH_4$ and formation of MgB_2 was observed for samples kept at temperatures below the thermodynamic equilibrium temperature of $LiBH_4$. Such conditions can be, e.g., 400 °C and 5 bar hydrogen pressure, as they were applied for the isothermal volumetric measurements. Under low hydrogen pressures and heating ramps to temperatures above 400 °C or isothermal measurements at enhanced temperatures above the equilibrium temperatures of $LiBH_4$, the desorption of $LiBH_4$ and the formation of MgB_2 was observed to take place separately.

Under these conditions, an individual decomposition of $LiBH_4$ into LiH, B, H_2 and partial formation of $Li_2B_{12}H_{12}$ is suggested, because it was observed for the pure $LiBH_4$ [61, 62] as well as for the composite [81, 82]. The formation of this highly symmetric molecule and pure B can explain the delay for the formation of the MgB_2. For samples prepared under isothermal conditions with a higher hydrogen back-pressure, first Raman measurements do not give any indication for the presence of $Li_2B_{12}H_{12}$. The formation of MgB_2 is proposed to proceed directly from the desorption of the $LiBH_4$. However, this proposition needs to be confirmed in further measurements by methods sensitive to amorphous phases.

For the pure composites, a lengthy incubation period is observed between the two steps of the desorption reaction. The delayed onset of the desorption of $LiBH_4$ is suggested to relate to limited nucleation of MgB_2. Significantly reduced incubation periods are observed with addition of surplus amounts of the final reaction products, transition-metal based additives and continued cycling of the material.

Doping of the composites with additives can have a large beneficial effect on the sorption kinetics. For example, the addition of transition-metal isopropoxides lowers the onset temperature of the reaction and the reaction times for the first desorption are reduced by an order of magnitude to about 2 hours. The intermediate formation of metallic Mg remains, though, under the applied conditions.

Detailed investigations performed exemplarily on Zr-based additives by X-ray absorption spectroscopy and anomalous small angle X-ray scattering revealed the formation of finely distributed ZrB_2 nanostructures upon milling or cycling. A role of a chemical catalyst of these structures is rather unlikely. Its key issue seems to be support for heterogeneous nucleation of MgB_2 and grain refinement during the ongoing reactions. However, this needs to be further confirmed by in-situ XRD by comparison of the crystallite size evolution during the sorption reactions of pure and composites with additives. A cross-check for the role of heterogeneous nucleation was addressed with additional CaB_6. This compound has a high lattice misfit to the basal plane of MgB_2 and does not react with the composites. In the experiment, the incubation period was still present, though reduced. The shortened incubation period might be due to microstructural effects and indicates multiple effects of the additives. The location of the additive in general has to be confirmed by microscopic means such as TEM, not only in the initial as-milled state but also after cycling.

The absorption reaction appears to be single step with a simultaneous formation of MgH_2 and $LiBH_4$. It occurs under moderate temperatures and pressures of 50 bar hydrogen with an onset of the reaction around 250 °C. The experimental conditions for this reaction were not optimized, yet. No severe kinetic limitations were observed for this reaction. The absorption reaction can also be influenced by the additives to proceed completely within few hours.

Qualitative characterization of the rate limiting process during the ongoing sorption reaction was addressed by comparison to models with known rate limiting processes. The reaction mechanism remains similar with addition of the additives. For the desorption reaction a linear correlation of the transformed fraction was observed while for the absorption reaction a contracting volume appears to describe best the ongoing processes. The linear correlation to time for the desorption pro-

cess is possibly related to the formation and breaking away of newly formed MgB_2, similar to the breakaway corrosion on iron. The contracting volume in the absorption reaction is suggested to relate to the consumption of MgB_2. However, this is a qualitative description, for quantitative modeling of the ongoing processes, the exact reaction mechanism and the mobile species have to be identified. The use of the isotope effect is a powerful tool for the identification of mobile species and should be used in further measurements. Knowledge of the dominating transport processes during the reactions contributes to a better understanding of the ongoing processes and will further allow directed improvement of the reaction kinetics.

Significant improvement of the sorption kinetics in $LiBH_4-MgH_2$ reactive hydride composites was achieved by addition of transition-metal based additives. Detailed investigations have shown the formation of nanoscaled transition-metal borides for these additives. Their large beneficial effect is proposed to relate mainly to nucleation and grain refinement during the sorption reactions. However, for mobile applications in combination with a PEM fuel cell the reaction rates still need to be increased and the reaction temperatures lowered.

Bibliography

[1] M.G. Schultz, T. Diehl, G.P. Brasseur, and W. Zittel. Air Pollution and Climate-Forcing Impacts of a Global Hydrogen Economy. *Science*, 302:624–627, 2003.

[2] W.G. Colella, M.Z. Jacobson, and D.M. Golden. Switching to a U.S. hydrogen fuel cell vehicle fleet: The resultant change in emissions, energy use, and greenhouse gases. *Journal of Power Sources*, 150:150–181, 2005.

[3] US Department of Energy. $http://www1.eere.energy.gov/hydrogenandfuelcells/-storage/pdfs/targets\_onboard\_hydro\_storage.pdf$, 2002.

[4] G.G. Libowitz, H.F. Hayes, and T.R.G. Gibb Jr. The system zirkonium-nickel and hydrogen. *Journal Physical Chemistry*, 62:76, 1958.

[5] J.J. Reilly and R.H. Wiswall. The Reaction of Hydrogen with Alloys of Magnesium and Copper. *Inorganic Chemistry*, 6(12):2220–2223, 1967.

[6] J.J. Reilly and R.H. Wiswall. Reaction of hydrogen with alloys of magnesium and nickel and the formation of Mg_2NiH_4. *Inorganic Chemistry*, 7(11):2254–2256, 1968.

[7] W. Oelerich, T. Klassen, and R. Bormann. Metal oxides as catalysts for improved hydrogen sorption in nanocrystalline Mg-based materials. *Journal of Alloys and Compounds*, 315:237–242, 2001.

[8] G. Barkhordarian, T. Klassen, and R. Bormann. Fast hydrogen sorption kinetics of nanocrystalline Mg using Nb_2O_5 as catalyst. *Scripta Materialia*, 49(3):213–217, 2003.

[9] M. Dornheim, N. Eigen, G. Barkhordarian, T. Klassen, and R. Bormann. Tailoring Hydrogen Storage Materials Towards Application. *Advanced Engineering Materials*, 5:377–385, 2006.

[10] M. Dornheim, S. Doppiu, G. Barkhordarian, U. Bösenberg, T. Klassen, O. Gutfleisch, and R. Bormann. Hydrogen storage in magnesium-based hydrides and hydride composites. *Scripta Materialia*, 56:841–846, 2007.

[11] G. Barkhordarian, T. Klassen, and R. Bormann. Patent pending, German Pub. No: DE102004/061286, priority 2004.

[12] G. Barkhordarian, T. Klassen, M. Dornheim, and R. Bormann. Unexpected kinetic effect of MgB_2 in reactive hydride composites containing complex borohydrides. *Journal of Alloys and Compounds*, 440:L18–L21, 2007.

[13] J.J. Vajo, F.O. Mertens, S.L. Skeith, and M.P. Balogh. Patent pending, Int. Pub. No: WO 2005/097671 A2, priority 2004.

[14] J.J. Vajo, S.L. Skeith, and F. Mertens. Reversible Storage of Hydrogen in Destabilized $LiBH_4$. *Journal of Physical Chemistry B*, 109:3719–3722, 2005.

[15] G. Barkhordarian, T.R. Jensen, S. Doppiu, U. Bösenberg, A. Borgschulte, R. Gremaud, Y. Cerenius, M. Dornheim, T. Klassen, and R. Bormann. Formation of $Ca(BH_4)_2$ from Hydrogenation of CaH_2+MgB_2 Composite. *Journal Physical Chemistry C*, 112:2743–2749, 2008.

[16] Y.W. Cho, J-H Shim, and B.J. Lee. Thermal destabilzation of binary and complex metal hydrides by chemical reaction: A thermodynamic analysis. *Computer Coupling of Phase Diagrams and Thermochemistry*, 30:65–69, 2006.

[17] S.V. Alapati, J.K. Johnson, and D.S. Sholl. Identification of Destabilized Metal Hydrides for Hydrogen Storage Using First Principles Calculations. *Journal of Physical Chemistry B*, 110:8769–8776, 2006.

[18] B. Bogdanovic and M. Schwickardi. Ti-doped alkali metal aluminium hydrides as potential novel reversible hydrogen storage materials. *Journal of Alloys and Compounds*, 253-254:1–9, 1997.

[19] E. Deprez. Master's thesis, University of Sevilla, 2008.

[20] J.W. Kim, J.-P. Ahn, S.-A. Jin, S.H. Lee, H.-S. Chung, J.-H. Shim, Y.W. Cho, and K.H. Oh. Microstructural evolution of NbF_5-doped MgH_2 exhibiting fast hydrogen sorption kinetics. *Journal of Power Sources*, 178(1):373 – 378, 2008.

[21] B.D. Cullity. *Elements of X-ray Diffraction.* Addison-Wesley Publishing Company, Inc., 1978.

[22] Y. Cerenius, K. Staal, L.A. Svensson, T. Usby, A. Oskasson, J. Albertson, and A. Liljas. The crystallography beamline I711 at MAX II. *Journal of Synchrotron Radiation*, 7:203–208, 2000.

[23] A. Guinier and A. Fournet. *Small-Angle scattering of X-rays.* John Wiley & Sons, 1955.

[24] R.-J. Roe. *Methods of X-ray and Neutron Scattering in Polymer Science*, pages 155–209. Oxford University Press, 2000.

[25] S. M. King. *Modern Techniques for Polymer Characterisation*, pages 171–232. John Wiley & Sons, 1999.

[26] D. I. Svergun and M. H. I. Koch. Small-angle scattering studies of biological macromolecules in solution. *Reports on Progress in Physics*, 66:1735–1782, 2003.

[27] T.P. Russel, J.S. Lin, S. Spooner, and G.D. Wignall. Intercalibration of Small-Angle X-ray and Neutron Scattering Data. *Journal of Applied Crystallography*, 21:629–638, 1988.

[28] H.B. Stuhrmann, G. Goerigk, and B. Munk. *Handbook on Synchrotron Radiation*, chapter 17, Anomalous X-ray Scattering, pages 555–580. Elsevier Science Publishers, 1991.

[29] H.-G. Haubold, R. Gebhardt, G. Buth, and G. Goerigk. *Resonant Anomalous X-Ray Scattering*, pages 295–304. Elsevier Science, 1994.

[30] J.P. Simon and O. Lyon. *Resonant Anomalous X-Ray Scattering*, pages 305–322. Elsevier Science, 1994.

[31] Y. Waseda. *Anomalous X-Ray Scattering for Materials Characterization.* Springer, 2002.

[32] K. F. Ludwig, Jr. *Anomalous X-ray Scattering Studies of Liquids.* PhD thesis, Stanford University, 1986.

[33] O. Lyon and J. P. Simon. Anisotropy of partial structure factors in an unmixed Cu-Ni-Fe single crystal studied by anomalous small-angle X-ray scattering. *Journal of Physics: Condensed Matter*, 4(28):6073–6086, 1992.

[34] A. B. Bhatia and D. E. Thornton. Structural Aspects of the Electrical Resistivity of Binary Alloys. *Physical Review B*, 2(8):3004–3012, Oct 1970.

[35] O. Lyon, J.J. Hoyt, R Pro, B.E.C. Davis, B. Clark, de D. Fontaine, and J.P. Simon. Anomalous Small-Angle X-ray Scattering on Al-Zn and Al-Zn-Ag Alloys. *Journal of Applied Crystallography*, 18:480–486, 1985.

[36] J.P. Simon, O. Lyon, and de D. Fontaine. A Comparison of the Merits of Isotopic Substitution in Neutron Small-Angle Scattering and Anomalous X-ray Scattering for the Evaluation of Partial Structure Functions in a Ternary Alloy. *Journal of Applied Crystallography*, 18:230–236, 1985.

[37] P. H. Fuoss, P. Eisenberger, W. K. Warburton, and A. Bienenstock. Application of Differential Anomalous X-Ray Scattering to Structural Studies of Amorphous Materials. *Physical Review Letters*, 46(23):1537–1540, Jun 1981.

[38] R.G. Munro. Reliabilitiy of partial structure factors determined by anomalous dispersion of X-rays. *Physical Review B*, 25(8):5037–5045, 1982.

[39] G. Goerigk, R. Schweins, K. Huber, and M. Ballauff. The distribution of Sr^{2+} counterions around polyacrylate chains analyzed by anomalous small-angle X-ray scattering. *Europhysics Letters*, 66(3):331–337, 2004.

[40] U. Vainio. *Characterisation of Cellulose- and Lignin-based Materials using X-Ray Scattering Methods*. PhD thesis, University of Helsinki, 2007.

[41] U. Vainio, K. Pirkkalainen, K. Kisko, G. Goerigk, N.E. Kotelnikova, and R. Serimaa. Copper and copper oxide nanoparticles in a cellulose support studied using anomalous small-angle X-ray scattering. *European Physical Journal D*, 42:92–101, 2007.

[42] H-G. Haubold, K. Gruenhagen, M. Wagener, H. Jungbluth, H. Heer, A. Pfeil, H. Rongen, G. Brandenberg, R. Moeller, J. Matzerath, P. Hiller, and H. Halling. JUSIFA-A new user-dedicated ASAXS beamline for materials science. *Review of Scientific Instruments*, 60:1943–1946, 1989.

[43] G. Goerigk. Electronics and Computer Upgrades at ASAXS Beamline JUSIFA. HASYLAB annual report, 2006.

[44] Bruce Ravel. Hephaestus programm. http://feff.phys.washington.edu/ ravel/software/exafs/.

[45] P. Debye, H.R. Anderson, and H. Brumberger. Scattering by and Inhomogeneous Solid II The Correlation Function and Its Application. *Journal of Applied Physics*, 28, No. 6:679–683, 1957.

[46] G. Goerigk and D. L. Williamson. Nanostructured Ge distribution in a-SiGe:H alloys from anomalous small-angle X-ray scattering studies. *Solid State Communications*, 108, No. 7:419–424, 1998.

[47] G. Goerigk and D. L. Williamson. Quantitative ASAXS of germanium inhomogeneities in amorphous silicon-germanium alloys. *Journal of Non-Crystalline Solids*, 281:181–188, 2001.

[48] A. Bianconi, J. Garcia, and M. Benfatto. XANES in Condensed systems. *Topics in Current Chemistry*, 145:29–67, 1988.

[49] D.C. Koningsberger and R. Prins. *X-ray Absorption.* John Wiley & Sons, 1988.

[50] K. Attenkofer, L. Tröger, M. Herrmann, and U. Brüggmann. Hasylab annual report 1998. Technical report, HASYLAB, 1998.

[51] K. Attenkofer. *Die magnetische Kopplung in ausgewählten Verbindungen - Neue Möglichkeiten und Entwicklungen der Rumpfanregungspektroskopie mit zirkularpolarisierten Photonen.* PhD thesis, Hamburg, 2000.

[52] G. Evans and R.F. Pettifer. CHOOCH: a program for deriving anomalous-scattering factors from X-ray fluorescence spectra. *Journal of Applied Crystallography*, 34:82–86, 2001.

[53] S. Kraft, J. Stümpel, P. Becker, and U. Kuetgens. High resolution X-ray absorption spectroscopy with absolute energy calibration for the determination of absorption edge energies. *Review of Scientific Instruments*, 67(3):681–687, March 1996.

[54] F.E. Pinkerton, M.S. Meyer, G.P. Meisner, M.P. Balogh, and J.J. Vajo. Phase boundaries and reversibility of $LiBH_4/MgH_2$ hydrogen storage material. *Journal of Physical Chemistry C, Letters*, 111 (35):12881 –12885, 2007.

[55] E.M. Fedneva, V.I. Alpatova, and V.I. Mikheeva. Thermal Stability of Lithium Tetrahydrobarate. *Russian Journal of Inorganic Chemistry*, 9, No. 6:826–827, 1964.

[56] H.I. Schlesinger and H.C. Brown. Metallo Borohydrides III Lithium Borohydride. *Journal of the American Chemical Society*, 62:3429–3435, 1940.

[57] Ph. Mauron, F. Buchter, O. Friedrichs, A. Remhof, M. Bielmann, C.N. Zwicky, and A. Züttel. Stability and Reversibility of $LiBH_4$. *Journal Physical Chemistry B*, 112:906–910, 2008.

[58] A. Züttel, S. Rentsch, P. Fischer, P. Wenger, P. Sudan, Ph. Mauron, and Ch. Emmenegger. Hydrogen storage properties of $LiBH_4$. *Journal of Alloys and Compounds*, 356-357:515–520, 2003.

[59] A. Züttel, P. Wenger, S. Rentsch, P. Sudan, Ph. Mauron, and Ch. Emmenegger. $LiBH_4$ a new hydrogen storage material. *Journal of Power Sources*, 118:1–7, 2003.

[60] N. Ohba, K. Miwa, M. Aoki, T. Noritake, S Towata, Y. Nakamori, S. Orimo, and A. Züttel. First-principles study on the stability of intermediate compounds of $LiBH_4$. *Physical Review B*, 74:075110, 2006.

[61] S. Orimo, N. Nakamori, N. Ohba, K: Miwa, M. Aoki, S. Towata, and A. Züttel. Experimental studies on intermediate compound of $LiBH_4$. *Applied Physics Letters*, 89:021920, 2006.

[62] S.-J. Hwang, R. C. Bowman, Jr., J. W. Reiter, J. Rijssenbeek, G. L. Soloveichik, J.-C. Zhao, H. Kabbour, and C. C. Ahn. NMR Confirmation for Formation of $[B_{12}H_{12}]^{2-}$ Complexes during Hydrogen Desorption from Metal Borohydrides. *Journal of Physical Chemistry C, Letters*, 112:3164–3169, 2008.

[63] J. Kostka, W. Lohstroh, M. Fichtner, and H. Hahn. Diborane Release from $LiBH_4$/Silica-Gel Mixtures and the Effect of Additives. *Journal of Physical Chemistry C*, 111:14026–14029, 2007.

[64] W. Oelerich. *Sorptioneigenschaften von nanokristallinen Metallhydriden für die Wasserstoffspeicherung.* PhD thesis, Technische Universität Hamburg-Harburg, 2000.

[65] G. Balducci, S. Brutti, A. Ciccioli, G. Gigli, P. Manfrinetti, A. Palenzona, M.F. Butman, and L. Kudin. Thermodynamics of the intermediate phases in the Mg-B system. *Journal of Physics and Chemistry of Solids*, 66:292–297, 2005.

[66] S. Orimo, Y. Nakamori, G. Kitahara, K. Miwa, N. Ohba, S Towata, and A. Züttel. Dehydriding and rehydriding reactions of $LiBH_4$. *Journal of Alloys and Compounds*, 404-406(SPEC. ISS):427–430, December 2005.

[67] O. Friedrichs, F. Buchter, A. Borgschulte, A. Remhof, C.N. Zwicky, Ph. Mauron, M. Bielmann, and A. Züttel. Direct synthesis of $Li[BH_4]$ and $Li[BD_4]$ from the elements. *Acta Materialia*, 56(5):949–954, 2007.

[68] Xuefei Wan, Tippawan Markmaitree, William Osborn, and Leon L. Shaw. Nanoengineering-Enabled Solid-State Hydrogen Uptake and Release in the $LiBH_4$ Plus MgH_2 System. *Journal of Physical Chemistry C*, 112(46):18232–18243, 2008.

[69] L. Schlapbach and A. Züttel. Hydrogen-storage materials for mobile applications. *Nature*, 414 23:353–358, 2001.

[70] L. Mosegaard, B Moller, J.-E. Jorgensen, Y. Filinchuk, Y. Cerenius, J. C. Hanson, E. Dimasi, F. Besenbacher, and T.R. Jensen. Reactivity of $LiBH_4$: In Situ Synchrotron Radiation Powder X-ray Diffraction Study. *Journal of Physical Chemistry C*, 112 (4):1299–1303, 2007.

[71] D.R. Lide. *Handbook of Chemistry and Physics*. CRC Press, 1994.

[72] H. Müller-Buschbaum. Neue Verbindungen des $CaFe_2O_4$-Typs. *Zeitschrift für Anorganische und Allgemeine Chemie*, 343:113–224, 1966.

[73] C.J.M. Rooymans. The crystal structure of $LiScO_2$. *Zeitschrift für Anorganische und Allgemeine Chemie*, 313:324–325, 1961.

[74] A. Yu. Ignatov, J. Graetz, S. Chaudhuri, T.T. Salguero, J.J. Vajo, M. S. Meyer, Frederick E. Pinkerton, and T.A. Tyson. Spatial Configurations of Ti- and Ni-Species Catalyzing Complex Metal Hydrides: X-Ray Absorption Studies and First-Principles DFT and MD Calculations. In *X-ray absorption fine structure-XAFS 13: 13th international conference*, volume 882, pages 642–644. International XAFS Society, American Inst. of Physics, 2007.

[75] D. Svergun and A. Semenyuk. PROGRAM PACKAGE GNOM. http://www.embl-hamburg.de/ExternalInfo/Research/Sax/, 2003.

[76] K. Binder and S. Theimer. Light metal hydrides for hydrogen storage: Optimization of production prameters. Master's thesis, Helmut-Schmidt University, 2007.

[77] R.Z. Mhuklis. Light metal oxides and hydroxides in reactive hydride composites. Master's thesis, Technical University Hamburg-Harburg, 2008.

[78] Y. Zhou. Catalysts investigations on the $LiBH_4/MgH_2$ reactive hydride composites. Master's thesis, Technische Universität Hamburg-Harburg, 2007.

[79] S. Orimo. private communication, 2008.

[80] C. Pistidda. private communication, 2008.

[81] D. Brampton, D. Reed, A. Walton, V. Mann, and D. Book. Decomposition of Lithium Borohydride-Magnesium Hydride Mixtures. Poster MH2008, Iceland, June 2008.

[82] R. C. Bowman, Jr. private communication, 2008.

[83] J. Purewal, S.-J. Hwang, R. C. Bowman, Jr., E. Rönnebro, B. Fultz, and C. Ahn. Hydrogen sorption behavior of the ScH_2-$LiBH_4$ system: Experimental assesment of chemical destabilization effects. *Journal of Physical Chemistry C*, 112(22):8481–8485, 2008.

[84] N.N. Greenwood and A. Earnshaw, editors. *Chemistry of the Elements*. Butterworth Heinemann, 2 edition, 1997.

[85] S. Lee. Crystal growth of MgB_2. *Physica C*, 385:31–41, 2003.

[86] S. Lee. Recent advances in crystal growth of pure and chemically substituted MgB_2. *Physica C*, 456:14–21, 2007.

[87] C. Zhuang, X. Liu, T. Guo, B. Wang, X. Li, C. Chen, and Q. Feng. The size effect of raw materials on the phase formation of polycrystalline MgB_2. *Superconductor Science and Technology*, 20:1125–1129, 2007.

[88] X.B. Yu, D.M. Grant, and G.S. Walker. A new dehydrogenation mechanism for reversible multicomponent borohydride systems: The role of LiMg alloys. *Chemical Communications*, 37:3906–3908, 2006.

[89] A. E. Finholt, A. C. Bond, and H. I. Schlesinger. Lithium aluminum hydride, aluminum hydride and lithium gallium hydride, and some of their applications in organic and inorganic chemistry. *Journal of the American Chemical Society*, 69(5):1199–1203, 1947.

[90] J.K. Kang, S.Y. Kim, Y.S. Han, R.P. Muller, and W.A. Goddard. A candidate $LiBH_4$ for hydrogen storage: Crystal structures and reaction mechanisms of intermediate phases. *Applied Physics Letters*, 87:111904, 2005.

[91] L. Mosegaard, B. Møller, J.-E. Jørgensen, U. Bösenberg, M. Dornheim, J. C. Hanson, Y. Cerenius, G. Walker, H. J. Jakobsen, F. Besenbacher, and T.R. Jensen. Intermediate phases observed during decomposition of $LiBH_4$. *Journal of Alloys and Compounds*, 446-447:301–305, 2007.

[92] S.-A. Jin, Y.-S. Lee, J.-H. Shim, and Y. W. Cho. Reversible hydrogen storage in $LiBH_4$-MH_2 (M=Ce, Ca) composites. *Journal of Physical Chemistry C*, 112:9520–9524, 2008.

[93] D. Gosslar. private communication, 2008.

[94] Y. Zhao, Y. Feng, C.H. Cheng, L. Zhou, Y. Wu, T. Machi, Y. Fudamoto, N. Koshizuka, and M. Murakam. High critical current density of MgB_2 bulk superconductor doped with Ti and sintered at ambient pressure. *Applied Physics Letters*, 79:1154, 2001.

[95] M.J. Kramer, S. L. Bud'ko, P.C. Canfield, R.D. Wilke, D.K. Finnemore, and J.S. Raymond. Intra-granular Ti precipitates in MgB_2. *cond-mat. supr-con*, arXiv:condmat/0302443v1.

[96] E. Deprez, C. López-Cartes, M.A. Munoz-Márquez, O. Friedrichs, J.C. Sánchez-López, U. Bösenberg, C. Bonnato, M. Dornheim, R. Bormann, and A. Fernández. A comperative study of the additive role int the MgH_2-Nb_2O_5 system vs. their MgH_2+2$LiBH_4$-Ti-iso system. In *3rd Hydrogen & Energy Symposium, Braunwald, Switzerland*, 2009.

[97] V.A. Lavrenko, A.V. Vasil'ev, and A.V. Rokhlenko. Study of the temperature dependence of the coefficients for hydrogen atom recombination on the surfaces of refractory materials. *Theoretical and Experimental Chemistry*, 7 No. 5:564–567, 1974.

[98] G.V. Samsonov and A.I. Kharlamov. Catalytic properties of refractory compound powders (survey). *Powder Metallurgy and Metal Ceramics*, 14, No. 9:699–707, 1976.

[99] S. Singh, S.W.H. Eijt, J. Huot, W.A. Kockelmann, M. Wagemaker, and F.M. Mulder. The $TiCl_3$ catalyst in $NaAlH_4$ for hydrogen storage induces grain

refinement and impacts on hydrogen vacancy formation. *Acta Materialia*, 55:5549–5557, 2007.

[100] B.E. Sundquist and L.F. Mondolfo. Heterogeneous nucleation in the liquid-to-solid transformation in alloys. *Transactions of the Metallurgical Society of AIME*, 221:157–164, 1961.

[101] N. Nakamori, H. Li, K Miwa, S. Towata, and S. Orimo. Syntheses and Hydrogen Desorption Properties of Metal-Borohydrides $M(BH_4)n$ (M= Mg, Sc, Zr, Ti and Zn; n=2-4) as Advanced Hydrogen Storage Materials. *Materials Transactions*, 47(8):1898–1901, 2006.

[102] William N. Lipscomb. *Boron Hydrides*. W.A. Benjamin, 1963.

[103] A. J. Du, Sean C. Smith, and G. Q. Lu. Role of charge in destabilizing AlH_4 and BH_4 complex anions for hydrogen storage applications: Ab initio density functional calculations. *Physical Review B (Condensed Matter and Materials Physics)*, 74(19):193405, 2006.

[104] A.J. Du, S.C. Smith, Y.D. Yao, and G.Q. Lu. Role of Lithium Vacancies in Accelerating the Dehydrogenation Kinetics on a $LiBH_4$(010) Surface: An Ab Initio Study. *Journal Physical Chemistry C*, 111:12124–12128, 2007.

[105] Q. Ge. Structure and Energetics of $LiBH_4$ and Its Surfaces: A First-Principles Study. *Journal of Physical Chemistry A*, 108:8682–8690, 2004.

[106] K. Miwa, N. Ohba, S. Towata, N. Nakamori, and S. Orimo. First-principles study on lithium borohydride $LiBH_4$. *Physical Review B*, 69:245120, 2004.

[107] M.R. Hartmann, J.J. Rush, T.J. Udovic, R.C. Bowman, Jr., and S.-J. Hwang. Structure and vibrational dynamics of isotopically labeled lithium borohydride using neutron diffraction and spectroscopy. *Journal of Solid State Chemistry*, 180:1298–1305, 2007.

[108] G. Renaudin, S. Gomes, H. Hagemann, L. Keller, and K. Yvon. Structural and spectroscopic studies on the alkali borohydrides MBH_4 (M = Na, K, Rb, Cs). *Journal of Alloys and Compounds*, 375:98–106, 2004.

[109] G. Barkhordarian. private communication, 2009.

[110] M.H. Mintz and J. Bloch. Evaluation of the kinetics and mechanisms of hybriding reactions. *Progress in Solid State Chemistry*, 16:163–194, 1985.

[111] M.H. Mintz and Y. Zeiri. Hydriding kinetics of powders. *Journal of Alloys and Compounds*, 216:159–175, 1994.

[112] G. Barkhordarian, T. Klassen, and R. Bormann. Kinetic investigation of the effect of milling time on the hydrogen sorption reaction of magnesium catalyzed with different Nb_2O_5 contents. *Journal of Alloys and Compounds*, 407:249–255, 2006.

[113] J. Bloch and M.H. Mintz. Kinetics and mechanisms of metal hydrides formation - a review. *Journal of Alloys and Compounds*, 253-254:529–541, 1997.

[114] H. Sasaki. Introduction of Particle-Size Distribution into Kinetics of Solid-State Reaction. *Journal of the American Ceramic Society*, 47 (10):512–516, 1964.

[115] P.C. Kapur. Kinetics of solid-state reactions of pariculate ensembles with size distributions. *Journal of the American Ceramic Society*, 56(2):79–81, 1973.

[116] C. Cui, D. Liu, Y. Shen, J. Sun, F. Meng, R. Wang, S. Liu, A.L. Greer, S.K. Chen, and B.A. Glowacki. Nanoparticles of the superconductor MgB_2:structural characterization and in situ study of synthesis kinetics. *Acta Materialia*, 52:5757–5760, 2004.

[117] A. Yan, A. Lu, G. Liu, G. Yan, and L. Zhou. The kinetic analysis of formation behavior for the MgB_2 phase. *Journal of Alloys and Compounds*, 443:161–165, 2007.

[118] S.C. Yan, G. Yan, C.F. Liu, Y.F. Lu, and L. Zhou. Experimental study on the phase formation for the Mg-B system in Ar atmosphere. *Journal of Alloys and Compounds*, 437:298–3001, 2007.

[119] A. Borgschulte, A. Züttel, P. Hug, A.-M. Racu, and J. Schoenes. Hydrogen-Deuterium Exchange in Bulk $LiBH_4$. *Journal of Physical Chemistry A*, 112(21):4749–4753, 2008.

[120] K. Funke and H. Richtering. Nuclear resonance studies of ionic mobility in solid lithium hydride. *Berichte der Bunsen Gesellschaft für physikalische Chemie*, 72:619, 1968.

[121] R.L. Corey, D.T. Shane, R.C. Bowman, Jr., and M.S. Conradi. Atomic motions in $LiBH_4$ by NMR. *Journal of Physical Chemistry C*, 112(47):18706–18710, 2008.

Acknowledgments

I am very grateful to Prof. R. Bormann for the supervision of this work and for giving me the opportunity to work in the interesting field of metal hydrides for hydrogen storage. I wish to thank him for his guiding interest and discussions and at the same time giving me freedom for independent research.

I thank Prof. T. Klassen very much for his constant interest, discussions and encouragement in the work and for examining the thesis.

I sincerely appreciate the scientific and mental support from Dr. M. Dornheim, his encouragement and inspiring discussions.

Many of the results could not have been obtained without the collaboration with the partners of the FunkHy and Cosy project and other collaborations. For this I wish to express my gratitude to

- Dr. O. Gutfleisch and his group at the IFW in Dresden for the high-pressure DSC measurements and the welcoming atmosphere.
- Dr. T. R. Jensen and his group from Århus university in Denmark for introducing me to in-situ XRD measurements and for all this good time at the beamline in Lund.
- Prof. A. Fernandez and E. Deprez for their TEM investigations in Sevilla, visualizing the samples for the first time.
- Prof. W. Jäger and Dr. D. Häußler from the CAU Kiel for their interest and efforts on TEM measurements.
- Prof. Kyu Hwan Oh and Mr. Ji Woo Kim from the Seoul National University and Prof. Young Whan Cho and Dr. Jae-Pyoung Ahn from KIST for the spectacular TEM micrographs.
- Dr. P.K. Pranzas and Dr. U. Vainio for introducing and teaching me small angle scattering and the joyfull collaboration.

- Prof. T. Klassen and his group at the HSU in Hamburg for the HP-DSC measurements and all the cups of tea.

I wish to thank the beamline staff at I 711 MAX-lab, A1 and B1 at Hasylab, DESY and the SNBL at the ESRF, Grenoble for their patience and help with all my questions and wishes.

Without the support and inspiring atmosphere in the group at GKSS this work would not have been possible. I owe my thanks to Gustavo Lozano, Dr. Klaus Taube, Dr. Michael Störmer, Prof. Michael Dahms, Christian Horstmann, Oliver Metz, Dr. Gagik Barkhordarian, Claudio Pistidda, Dr. José Bellosta von Colbe, Dr. Rapee Gosalawit, Christian Bonatto Minella and Sabine Schrader as well as the former members Claude Keller, Dr. Nico Eigen, Dr. Xiumei Xi and Dr. Andreas Borgschulte for their advise, support, collaboration and jokes. I especially appriciate the work and collaboration with the Master students Christopher Nwakwuo, Yanping Zhou and Reiza Mukhlis.

I thank my family and friends for their support, patience and encouragement during the studies and dissertation.